INL/RPT-23-71392

Engineering-scale Modeling of High-Temperature Creep and Creep Crack Growth in Alloy 316H

January 2023

Antonio M. Recuero[a]
Daniel Schwen[a]
Albert Dahal[a]
Benjamin W. Spencer[a]
Markian Petkov[b]
Pierre-Alexandre Juan[b]

[a]Idaho National Laboratory, P.O. Box 1625, Idaho Falls, ID 83415-3840
[b]Kairos Power LLC, 707 W. Tower Ave., Alameda, CA 94501

INL is a U.S. Department of Energy National Laboratory
operated by Batelle Energy Alliance, LLC

INL/RPT-23-71392

Engineering-scale Modeling of High-Temperature Creep and Creep Crack Growth in Alloy 316H

Antonio M. Recuero[a]

Daniel Schwen[a]

Albert Dahal[a]

Benjamin W. Spencer[a]

Markian Petkov[b]

Pierre-Alexandre Juan[b]

[a]Idaho National Laboratory, P.O. Box 1625, Idaho Falls, ID 83415-3840
[b]Kairos Power LLC, 707 W. Tower Ave., Alameda, CA 94501

January 2023

Idaho National Laboratory
Computational Mechanics and Materials Department
Idaho Falls, Idaho 83415

http://www.inl.gov

Prepared for the
U.S. Department of Energy
Office of Nuclear Energy
Under DOE Idaho Operations Office
Contract DE-AC07-05ID14517

SUMMARY

This document demonstrates completion of the goals described in the technical narrative of the Department of Energy's Industry Funding Opportunity Announcement (iFOA) project entitled "Modeling and Simulation Development Pathways to Accelerating KP-FHR Licensing," which relates to the development and demonstration of capabilities for conducting engineering-scale simulations of Alloy 316H components under high-temperature conditions. This work encompassed two major aspects: integrating and testing constitutive models for the creep response of 316H at high temperatures, and developing tools for modeling creep crack growth (CCG) in 316H. Two classes of constitutive models were used in this effort: phenomenological models based on behavior observed at the engineering scale, and reduced-order models (ROMs) that represent the nonlinear response of mesoscale models that capture the sensitivity to material microstructure and processing. Likewise, the approaches employed for CCG modeling considered both simplified engineering approaches and detailed simulations of creep and damage ahead of the crack tip. These developments, which were performed by utilizing the Grizzly code as well as the open-source libraries it depends on, strengthen Grizzly's ability to support licensing and safety analyses of high-temperature reactor components.

ACKNOWLEDGMENTS

This manuscript was authored by Battelle Energy Alliance, LLC under contract no. DE-AC07-05ID14517 with the U.S. Department of Energy, with funding from the U.S. Industry Opportunities for Advanced Nuclear Technology Development Announcement No: DE-FOA-0001817. The U.S. Government retains a nonexclusive, paid-up, irrevocable, worldwide license to publish or reproduce the published form of this manuscript, or allow others to do so, for U.S. Government purposes.

This research utilized the resources of the High Performance Computing Center at Idaho National Laboratory, which is supported by the Office of Nuclear Energy of the U.S. Department of Energy and the Nuclear Science User Facilities under contract no. DE-AC07-05ID14517.

CONTENTS

1 INTRODUCTION

The fluoride-salt-cooled high-temperature reactor (FHR) [34, 92] is an advanced nuclear reactor that has been proposed in recent years for meeting the growing demand for clean, safe, and affordable energy. This reactor type employs a molten-salt coolant as well as fuel pebbles based on tri-structural isotropic (TRISO) particle fuel to generate high-temperature heat. The Li_2BeF_4 (i.e., FLiBe) salt used as a coolant in this system has a very high vaporization temperature, enabling the primary coolant system to operate at high temperatures and near-atmospheric pressures. The TRISO fuel used in the FHR has proven capabilities for fission product retention at high temperatures. The U.S. company Kairos Power (KP) is focused on developing and commercializing their own version of the FHR (i.e., the KP-FHR). The KP-FHR takes advantage of the significant research performed in development of TRISO fuel, molten salts, and high-temperature alloys—research initially targeting other Generation IV reactor designs.

The U.S. Department of Energy Industry Funding Opportunity Announcement (iFOA) project "Modeling and Simulation Development Pathways to Accelerating KP-FHR Licensing" is a recently concluded collaborative effort between KP and various national laboratories to develop and demonstrate computational simulation tools to help overcome the technical barriers to licensing the KP-FHR. Idaho National Laboratory (INL) performed major roles in developing simulation tools to predict the performance of two important aspects of this reactor system: the TRISO fuel and the high-temperature metallic components. This report summarizes the joint INL/KP effort pertaining to structural component integrity, while a separate report documents the INL/KP effort pertaining to fuel performance.

Both of these efforts leveraged previously developed simulation tools based on the Multiphysics Object-Oriented Simulation Environment (MOOSE) [62], an open-source platform that provides the foundation for specialized simulation tools. The structural effort documented herein is based on the Grizzly code [98], which is a tool for assessing the progression and effects of structural component degradation in nuclear reactors. It was originally developed to target light-water reactors, but recent efforts such as those detailed in this report have extended its capabilities to advanced high-temperature reactors as well. Note that a subset of Grizzly's capabilities is provided by an open-source code called BlackBear; in fact, many of the capabilities discussed in this report are actually provided by BlackBear or MOOSE.

As Alloy 316H is the material used in the primary coolant system of the KP-FHR, it is the focus of the efforts described herein. INL's role in the present project covered two major areas: integration and testing of constitutive models for the creep response of 316H at high temperatures, and the development of tools for modeling creep crack growth (CCG) in 316H. For both creep and creep fracture modeling, a combination of accepted, lower-risk engineering approaches and more advanced approaches was employed.

For modeling creep in 316H, the INL effort focused on integrating constitutive models developed by other organizations into Grizzly, the objective being to use those models in full-scale simulations of a representative reactor vessel under complex and challenging conditions. The first of these models is a phenomenological engineering-scale model developed by Argonne National Laboratory (ANL) [6]. This class of models is calibrated to experimental data for material behavior under conditions that are ideally close to actual reactor operating conditions. The employed model was developed using the open-source Nuclear Engineering Material model Library (NEML), which is accessed through an interface provided in BlackBear. Major advantages of this class of models are that they are relatively simple and robust, and are widely accepted within the engineering community. Importantly, efforts are underway to achieve acceptance of this class of models in the context of design codes. Such acceptance would benefit future licensing efforts for the KP-FHR and other high-temperature reactors.

An important deficiency of all phenomenological models is that they are only applicable in regimes

for which they have calibration data. This limits their applicability to other environmental conditions (i.e., stress and temperature), and makes it challenging for them to account for the effects of changes due to the microstructure, whether caused by material processing or environmental effects such as irradiation or corrosion. Sophisticated approaches for modeling microstructure evolution under such conditions do exist, and significant advances are continually being made to these models. However, it has been challenging to apply the outcomes of mesoscale simulations to models that can be practically applied at the engineering scale. The Los Alamos Reduced Order Models for Advanced Nuclear Constitutive Equations (LAROMance), developed by Los Alamos National Laboratory (LANL), address this need by employing data analytics to represent the viscoplastic behavior of representative volumes of a material predicted by sophisticated mesoscale models in a way that is usable in engineering-scale simulations [102]. This approach enables the effects of unique material processing conditions and environmental exposure to be directly accounted for, rather than relying on re-fitting of phenomenological models under the full range of possible conditions. Efforts to integrate the NEML and LAROMance models for 316H, develop needed supporting code features, and apply those models to simulations of the reactor vessel response under operational conditions are described in Section 2 of this report.

The design specifications primarily focus on the deformation response of high-temperature alloys. Another important safety consideration is the effect of flaws that may be present in components. If present, these flaws can grow during operation in a phenomenon known as creep crack growth (CCG). If flaws are discovered during in-service inspections, the ability to predict their growth rates is essential for the safe and economical operation of reactors. In an approach similar to that taken for constitutive modeling, this project pursued a combination of simplified engineering approaches for predicting CCG, as well as more sophisticated approaches that employ detailed high-dimensional finite element simulations to predict the strain localization and the damage ahead of the crack tip—both of which lead to crack growth, as described in Section 3 and Section 4, respectively. While the engineering approaches are straightforward, they are limited in their range of applicability. Demonstrating the compatibility of these two types of models is an important aspect of developing a capability that addresses a wide variety of flaws and loading conditions.

These developments in the modeling of creep deformation and CCG in 316H have greatly expanded Grizzly's capabilities for assessing the performance of components in the KP-FHR and other high-temperature advanced reactors.

2 VESSEL TRANSIENT MODELING

An important objective of this project was to apply MOOSE-based simulation tools (i.e., Grizzly and BlackBear), together with the advanced constitutive equations being developed for 316H, to a realistic simulation of the KP-FHR to demonstrate that both the constitutive models and engineering-scale simulation code are adequately robust for use in production simulations.

2.1 Constitutive model integration

2.1.1 NEML integration with Grizzly

NEML is public, open-source software and is hosted on a GitHub repository maintained by ANL [6]. NEML has internal functions for performing all calculations involved in evaluating the stress tensor for a material point under given strain increment, temperature and variables describing history the history of that material point's behavior. NEML has built-in Python-based constitutive model drivers for testing the various material models that NEML provides. Accessing those models from a finite element code requires the development of an additional interface that calls the NEML model.

The interface to NEML for MOOSE is implemented in BlackBear's `NEMLStress` object, which behaves similarly to any other material model in MOOSE but provides the material calculations by calling functions in NEML. NEML is accessed from `NEMLStress` using a submodule in the BlackBear Git repository. This submodule can be updated as needed to make new features that were developed in NEML available to both BlackBear and Grizzly.

The interface to NEML through the `NEMLStress` object had already been developed prior to this project, but INL developers worked closely with NEML developers at ANL to make multiple updates to NEML to accommodate the needs of this project. In addition, an independent assessment of the adherence of Grizzly and BlackBear to the American Society of Mechanical Engineers (ASME) Nuclear Quality Assurance (NQA-1) requirements was performed concurrently with this project to meet the needs of other programs using those codes. A number of improvements to the codes, as well as to the testing and documentation thereof, were implemented while preparing for the assessment and addressing the issues it raised. Those issues pertaining to the interface with NEML were addressed as part of this iFOA project.

Testing of the NEML models is an important area in which software quality as it relates to the NEML interface was improved as part of this project. NEML has a set of regression tests used in the course of its development, and those tests consist of direct material model evaluations performed through its Python interface. It is important that those models produce equivalent results when run from the BlackBear finite element code. To ensure full testing of the models available to BlackBear, a system was developed to populate a set of test cases in BlackBear that run the same material models and conditions as used in the NEML internal tests, but from a single-element finite element model. The BlackBear testing refers to the same reference results utilized by the NEML internal tests, thus ensuring that the models give the correct results and that whenever the version of NEML used by BlackBear is updated, BlackBear also runs an updated set of tests corresponding to that NEML version.

2.1.2 LAROMance integration with Grizzly

The LAROMance models compute the inelastic strain increment and updated material state data, based on the current von Mises stress and material state. Because the models for isotropic materials such as 316H

are based on assumptions of pressure-independent behavior and associated flow, they can utilize the same radial return mapping procedures used for other plasticity and creep models in MOOSE. The material model `LAROMANCEStressUpdateBase` in the MOOSE TensorMechanics module provides an implementation of these models that can be used in the same manner as any other creep or plasticity model in MOOSE. Specializations of this model are provided for specific materials such as 316H.

As was the case for the NEML model, this MOOSE interface to LAROMance was developed to meet the needs of other programs outside this iFOA project; however, extensive development and testing of this model were performed in support of this project. We developed a Javascript-Object-Notation-based file format for LAROMance models, enabling more convenient exchange of reduced-order model (ROM) data.

2.2 Other capability development activities

In addition to integrating the constitutive models into Grizzly/BlackBear, the full vessel lifetime simulation required a number of MOOSE capability improvements. These are detailed in the following sections.

2.2.1 LAROMance substepping

A major component of the structural materials effort in this project was to develop and apply a ROM for 316H, based on LANL's LAROMance methodology. The model for 316H remained in development at LANL during much of the project performance period. While waiting for the final model version, INL focused on making foundational improvements to the LAROMance model framework in MOOSE to improve its usability and robustness. Here, the primary focus was to implement a substepping algorithm that was based on a user-defined tolerance and that would apply to all LAROMance models in MOOSE-based codes. Substepping (i.e., the division of the material timesteps at local material points into sets of smaller steps) allows the user to control the creep strain increments taken in the time integration of the material model in a way that is independent of the global time stepping. Below is an excerpt from a MOOSE input file exercising this feature:

```
[Materials]
    ...
    [rom_stress_prediction]
        type = LaRomance316hkp4
        temperature = T
        stress_unit = MPa
        initial_cell_dislocation_density = ${cell_density}
        initial_wall_dislocation_density = ${wall_density}
        max_inelastic_increment = 1e-4
        max_relative_wall_dislocation_increment = 0.05
        max_relative_cell_dislocation_increment = 0.05
        outputs = all
        verbose = false
        stress_input_window_low_failure = EXTRAPOLATE
        stress_input_window_high_failure = EXCEPTION
        temperature_input_window_high_failure = ERROR
        wall_input_window_low_failure = ERROR
        wall_input_window_high_failure = EXCEPTION
```

```
        cell_input_window_low_failure = ERROR
        cell_input_window_high_failure = EXCEPTION
        internal_solve_output_on = on_error
        internal_solve_full_iteration_history = false

        use_substepping = ERROR_BASED
        adaptive_substepping = true
        substep_strain_tolerance = 1.0e-4

        maximum_number_substeps = 1000
        block = 1
    []
[]
```

The substepping algorithm handles increments of stateful properties (e.g., wall and cell dislocation density), dividing the timestep into substeps over which to solve the creep—and possibly the plasticity—problem. There are two major benefits to this approach: (1) the creep numerical integration error is limited to a user-selected value, and (2) the system's timestep is not directly governed by the need of the local material points to take small steps to avoid integration error or to keep the model within acceptable bounds.

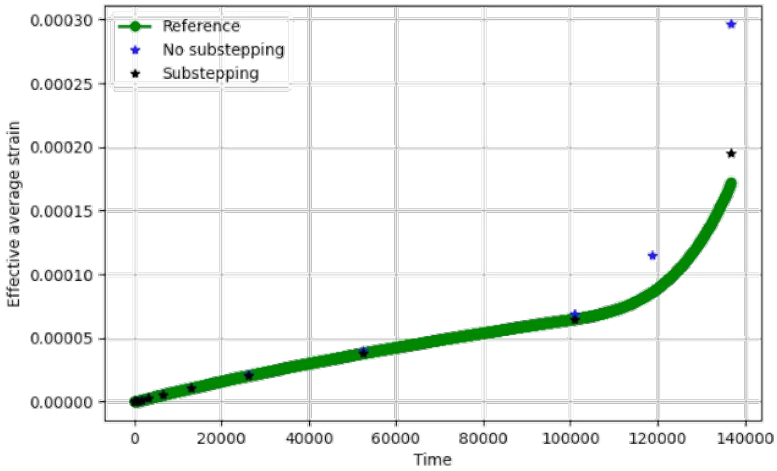

Figure 1: Effective average strain for various LAROMance simulations that used an exceedingly small timestep (green), regular time stepping (blue), and regular time stepping with substepping (black).

A basic example of the use of this algorithm is presented in Fig. 1. A problem with a small number of finite elements was first solved using a very small global time step (shown in green). This result provided a reference solution. The same problem was then simulated with a much larger time step that is more representative of what might be used in practice (blue asterisks). The resulting average strain in that solution greatly differed from the reference solution, due to creep integration error. Furthermore, the solver had to cut the timestep at about 120,000 s, prompting an additional system solve. Finally, using the substepping feature with large global timesteps (black asterisks), the creep numerical integration error was greatly reduced and the overall timestep increment was never cut, as the inelastic solves occurred over smaller timestep increments.

It is important to note that while these developments to the substepping algorithm were targeted at

the LAROMance model, they were implemented in the C++ base classes that are also used by most of the other creep and plasticity models in MOOSE. Thus, this development effort benefits a wide variety of other material models.

2.2.2 Adaptive substepping

In the substepping scheme (described in the previous section) for inelastic material evaluations, the number of substeps was determined by one of two criteria: a maximum inelastic increment or a maximum integration error metric. In running the LAROMance model, we observed that neither criterion resulted in a robust solve for common maximum inelastic increments and maximum integration errors (on the order of 10^{-4}). Often, only a few material points with high stress and/or high temperature would consistently fail to converge in their return mapping solutions. A convergence failure in the return mapping would trigger a C++ exception, leading to a cut in the global timestep and thereby increasing the overall computational cost of the model. Furthermore, the substepping criteria would result in a smaller number of substeps with the reduced global timestep, again leading to a failing return mapping solve. The only way around this would be to severely tighten the maximum inelastic increment or maximum integration error. However, doing so would increase the computational cost of the return mapping at every quadrature point, leading to unsustainably long computation times. In some parts of the transient, we would observe global timesteps on the order of seconds, whereas conventional constitutive models would permit timesteps on the order of days.

As a solution to this problem, we developed an adaptive substepping scheme. In this algorithm, the number of substeps for the local material evaluation is still based on either the maximum inelastic increment or maximum integration error metrics. However, if the return mapping solve fails for that material, an exception is thrown and caught within the material, and the local material solution is reattempted, this time with double the number of substeps (as long as the resulting number of substeps is at or below a user-specified maximum number of substeps). This avoids repeating the global solution with a smaller timestep, thus significantly reducing the computational time. This procedure of cutting back the local subincrement size is repeated until either the return mapping solve converges or the return mapping fails after having attempted the maximum number of substeps. In the latter case, the exception from the radial return mapping is rethrown and the global timestep cut. Adaptive substepping can be enabled by adding `adaptive_substepping = true` to the parameter block of the radial return mapping model.

We observed that, in many cases, this adaptive substepping scheme can lead to a sustained global timestep several orders of magnitude higher than would be possible without adaptive substepping, making previously infeasible simulations feasible.

2.2.3 Fast global timestep cutting

Although the substepping algorithms described in the previous sections are highly effective at preventing failures in the material evaluation, such failures do occasionally occur for various reasons. In those cases, rather than simply stopping execution of the code with an error, it is better that the nonlinear solution be stopped for the current step and then used to reattempt to solve it, this time with a smaller time increment. To accomplish this, the MOOSE framework utilizes C++ exceptions to signal issues during the nonlinear or linear iterations of the solve. Exceptions are caught at a high level and should lead to termination of the current simulation step, which is then repeated using a reduced global timestep. However, an issue arose during the process of handling the exception in this way, thus preventing interruption of the current solve under certain conditions relevant to actual production runs. The result was that even after an exception was thrown, linear and nonlinear iterations would continue until the simulation step either converged or failed to converge. At

that point, the timestep would be cut and the step repeated. However, this cutting of the timestep occurred only after reaching the maximum number of iterations, potentially necessitating considerable computational effort.

We identified the issue and implemented a fix to prevent any further evaluation of the residual or Jacobian once an exception is thrown during a simulation step. This essentially results in instantaneous termination of the current step, which is then repeated using a smaller timestep, substantially speeding up simulations that have convergence issues (e.g., the reactor vessel simulations performed in this effort).

2.2.4 Input file merging

To streamline the creation of multi-stage input files and reduce the duplication of input file content over multiple stages, we developed the ability to run MOOSE-based applications with multiple input files. Multiple input file names can be specified after the `-i` MOOSE command line option. The supplied inputs are then successively merged into a single simulation specification, with later files adding and overwriting parameters. This new capability allows users to factor out common parameters (e.g., solver options, postprocessors, and outputs) from a set of similar input files (e.g., `./mooseapp-opt -i common_parameters.i simulation_1.i`). The output file names will be based on the *last* input file name specified (unless the `Outputs/file_base` parameter is specified). When multiple inputs are specified, MOOSE informs the user about parameter overrides early in the simulation output log.

To assist users with refactoring input files, several new functions were added to the `hit` tool. This tool provides the library that is used by MOOSE for parsing input files, and has a command-line utility (distributed with MOOSE) that builds on this library and provides a number of input file manipulation capabilities. To facilitate management of models defined in multiple files, functions were added for merging, diffing, and subtracting parameters in input files, as well as for extracting the set of parameters in common across a set of input files.

We used this new capability to refactor and reduce the complexity of the input files used for the 14-stage transient vessel simulation. Common outputs, solver options, boundary conditions, material properties, physics kernels, and variable declarations were put in a single file used by the model in all stages of the transient. The individual stage inputs then contained only the different thermomechanical loading conditions. This approach makes it easy to change or add postprocessing and output options affecting the entire transient.

2.2.5 Material timestep enforcement

MOOSE material models can compute a local maximum timestep based on material behavior. For example, a common usage of this capability is to limit the timestep according to a maximum permissible inelastic deformation increment. The global timestep can be chosen such that the minimum local timestep for all material points is not exceeded. However, this global timestep limit can only be known at the end of a timestep, once the inelastic increments have been computed. The timestep limit would be applied to the next simulation step and would lag by one step. In cases of sudden onset of creep, this lag would cause some simulation steps to significantly exceed the calculated timestep cap, and as a result, creep increments could exceed the maximum specified values.

We added a new capability to MOOSE that enables users to automatically discard and repeat timesteps that lead to inelastic deformation increments that exceed the user-specified maximum by a given margin. This functionality is implemented in the `Terminator` user object (UO), which employs a user-specified function expression to make a decision on whether a simulation step will be accepted or discarded.

2.3 Results

2.3.1 Vessel head model

We meshed a computer-aided design (CAD) description of a KP-provided surrogate vessel head model into a hex mesh with side sets suitable for use with the MOOSE finite element framework. For an initial steady-state loading simulation, a set of boundary conditions that included constant temperature, constant flux, and convective heat transfer was applied to the heat transport portion of the model. Constant load and constant pressure boundary conditions were applied to the mechanical portion. Under these fixed boundary conditions, creep relaxation of the vessel head material was modeled over the course of 2 years simulation time. Our solution strategy was to simulate the steady-state heat transport decoupled from the time-dependent mechanical creep solve, and use the steady-state thermal solution as a constant temperature field during the creep solve. This decoupling reduces the number of degrees of freedom and thus the computational and memory requirements.

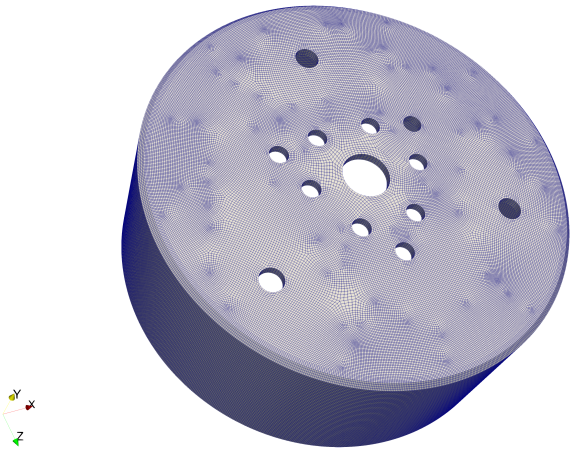

Figure 2: Vessel head mesh consisting of about 430,000 hex elements.

In a second simulated transient, the thermal loading conditions were set up to model the linear ramping up of reactor power over the course of 48 hours (which is quite aggressive; actual ramps would be slower), holding the reactor at constant load for 2 years and then ramping down the reactor power over a period of 24 hours. Initially relying on MOOSE's dynamic time-stepping capabilities, we encountered issues with the NEML model experiencing hard failures as creep set in with rising temperature, which was due in part to the fact that the timestep had previously grown in the initial phases of the power ramp. We approached this by limiting the timestep size during the power ramp phases, using MOOSE's built-in functionality to limit the timestep based on a maximum value change for a user-supplied function—in this case, a ramp function, with values in the interval [0, 1] being used to set up the thermal boundary conditions. Simultaneously, work began on improving the dynamic time-stepping system, based on information from NEML (e.g., scalar inelastic strain rate). Changes have been proposed to avoid hard failures in NEML and to instead signal back soft failures to MOOSE so as to trigger a cut-back of the simulation timestep.

In parallel to the work conducted by INL, LANL used our vessel head model to simulate the behavior of this component following an initial heat-up phase and 30 years of (steady-state) pseudo-"normal operations," and to assess the influence of microstructure (i.e., cell and wall dislocation contents) on the overall mechanical

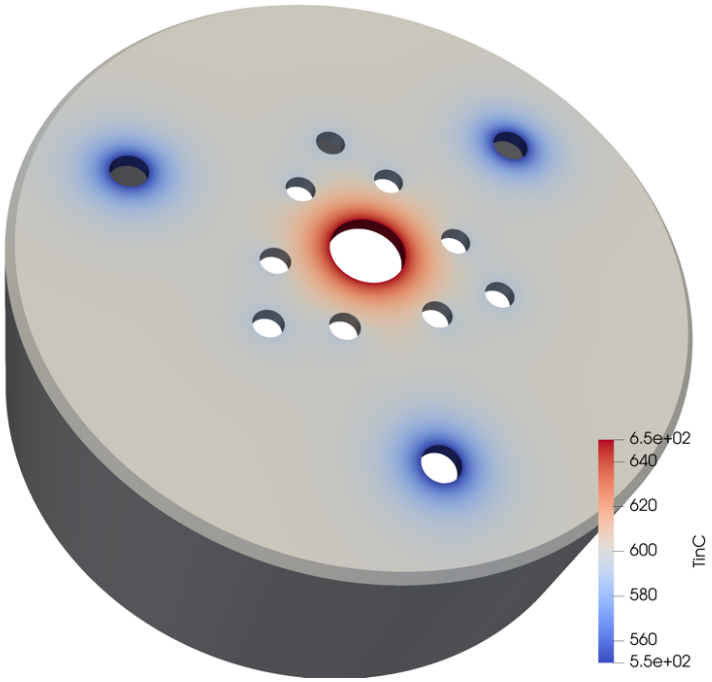

Figure 3: Steady-state temperature distribution.

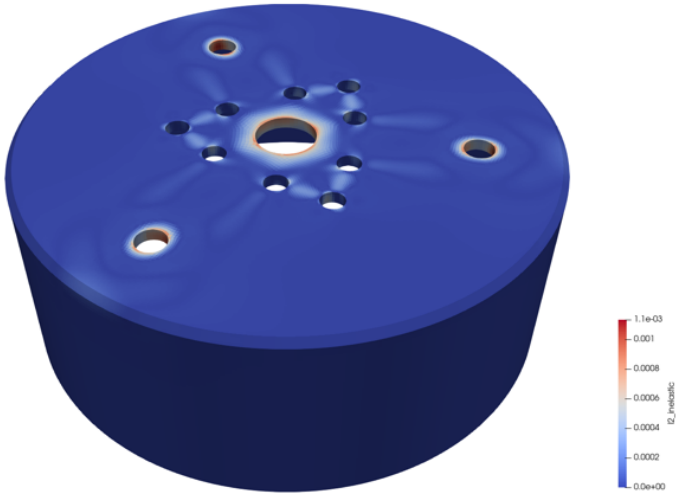

Figure 4: Total inelastic strain (Frobenius norm) at the end of the 2-year steady-state load phase (0.1% strain).

response of the component. The LAROMance model implemented into MOOSE and used by LANL for the vessel head was derived from LANL's visco-plastic self-consistent (VPSC) code, and differs from the more recent one we used for the full vessel simulations. The results (not shown here) were presented during the last project review, conducted on January 27, 2022. For more information on the differences between the various versions of the LAROMance model, see the LAROMance milestone report for this project.

2.3.2 Full vessel model

INL was provided a highly simplified and modified CAD model of the KP-FHR's full reactor vessel. The CAD model was meshed using the Cubit meshing software, and side sets were assigned to facilitate the application of boundary conditions in the finite element solve. In addition to the full model, partial models of half- and third-sections around the major axis of the vessel were prepared for future use in higher fidelity simulations; however, these are not shown here.

Vessel transient phases INL was provided a list of 14 stages, with defined thermal and mechanical boundary conditions spanning 30 years of reactor operation. Note that the thermal and mechanical boundary conditions provided by KP do not correspond to actual normal and accident conditions of the KP-FHR. Instead, they were meant to challenge the convergence of the models and span the whole temperature and strain ranges allowed by ASME Section III, Division 5. The conditions for these stages are summarized below:

1. Preparation of the vessel prior to startup (orange)

0 h	24 h	72 h
MLC0	MLC0	MLC1
TLC0	TLC1	TLC1

2. Filling & startup (yellow)

72 h	96 h	120 h
MLC1	MLC2	MLC2
TLC1	TLC1	TLC2

3. Normal operation for 10 years (green)

120 h	87600 h
MLC2	MLC2
TLC2	TLC2

4. Hot maintenance (red)

87600 h	87606 h	87762 h	87768 h
MLC2	MLC3	MLC3	MLC2
TLC2	TLC3	TLC3	TLC2

5. Normal operation for 3 years (green)

87768 h	113880 h
MLC2	MLC2
TLC2	TLC2

6. Overheating or loss-of-coolant accident (LOCA) (blue)

113880 h	113928 h	114000 h	114048 h
MLC2	MLC3	MLC3	MLC2
TLC2	TLC3	TLC3	TLC2

7. Normal operation for 7 years (green)

114048 h	175200 h
MLC2	MLC2
TLC2	TLC2

8. Hot maintenance (red)

175200 h	175206 h	175362 h	175368 h
MLC2 TLC2	MLC3 TLC3	MLC3 TLC3	MLC2 TLC2

9. Normal operation for 5 years (green)

175368 h	219000 h
MLC2 TLC2	MLC2 TLC2

10. Pump trip (overpressure accident) (blue)

219000 h	219024 h	219048 h	219072 h
MLC2 TLC2	MLC5 TLC2	MLC5 TLC2	MLC2 TLC2

11. Hot maintenance (red)

219072 h	219078 h	219234 h	219240 h
MLC2 TLC2	MLC3 TLC3	MLC3 TLC3	MLC2 TLC2

12. Normal operation for 5 years (green)

219240 h	262800 h
MLC2 TLC2	MLC2 TLC2

13. Drainage (yellow)

262800 h	262848 h	262850 h	262874 h	262876 h
MLC2 TLC2	MLC2 TLC5	MLC6a TLC5	MLC6b TLC5	MLC6c TLC5

14. Final shutdown (orange)

262876 h	262900 h
MLC6c TLC5	MLC0 TLC0

Mechanical loading conditions The mechanical loading conditions (MLCs) consist of both permanently applied and time-dependent loading conditions. The permanent loading conditions are listed below.

- In addition to the vessel's own weight, gravitational loads corresponding to the following masses must be prescribed to the vessel at various nozzle areas:
  - 4,000 kg mass at the hot leg nozzle
  - 1,500 kg mass at each cold leg nozzle
  - 1,000 kg at each nozzle associated with the reactor's reactivity management systems
- No vertical displacement allowed at the base of the vessel
- **MLC0**
  - Graphite mass: 180,000 kg prescribed to the bottom plate

  - No internal pressure

- **MLC1**
  - Graphite mass: 180,000 kg prescribed to the bottom plate
  - After the cover gas temperature reaches 500°C, 12 internal pressure cycles are applied:
    * From 0 to 4 bar gauge in 2 hours (linear increase)
    * From 4 to 0 bar gauge in 2 hours (linear decrease)

- **MLC2**
  - The cover gas pressure increases from 0 to 0.5 bar gauge and is prescribed to the top head and shell inner surfaces, both of which are in contact with the cover gas
  - Hydrostatic pressure is applied to the shell and bottom surfaces
  - 150 kN of upward force is distributed over the three thrust force contact areas
  - Bending moments and reaction forces are prescribed to the hot leg nozzle
    * Force (-10,000, -12,000, -5,000) N
    * Moment (5,000, -10,000, 30,000) Nm

- **MLC3**
  - The prescribed cover gas pressure is 0 bar gauge
  - Hydrostatic pressure
  - 30 kN of upward force is distributed over the three thrust force contact areas
  - No bending moment and reaction force at the hot leg nozzle area

- **MLC4** (same as MLC2)

- **MLC5**
  - A cover gas pressure of 3 bar gauge and is prescribed to the top head and shell inner surfaces, both of which are in contact with the cover gas
  - The rest of the mechanical boundary conditions are identical to those listed for MLC2 (i.e., bending moments and reaction forces prescribed to the hot leg nozzle, hydrostatic pressure and upward force distributed over the three thrust force contact areas)

- **MLC6a**
  - The cover gas pressure is progressively increased to 2 bar gauge
  - The rest of the mechanical boundary conditions are identical to those listed for MLC2 (i.e., bending moments and reaction forces prescribed to the hot leg nozzle, hydrostatic pressure and upward force distributed over the three thrust force contact areas)

- **MLC6b**
  - The cover gas pressure is set at 2 bar gauge
  - The hydrostatic pressure is progressively reduced by decreasing the FLiBe + graphite mass density from 1829 to 1750 kg/m^3

  - The upward force distributed over the three thrust force contact areas is reduced from 150 to 0 kN
  - The bending moments and reaction forces prescribed to the hot leg nozzle remain unchanged
- **MLC6c**
  - The cover gas pressure is set at 2 bar gauge
  - The hydrostatic pressure is progressively reduced by decreasing the FLiBe + graphite density from 1750 to 0 kg/m^3
  - Graphite mass: from 0 to 180,000 kg prescribed to the bottom plate
  - The bending moments and reaction forces prescribed to the hot leg nozzle remain unchanged.

Thermal loading conditions

- **TLC0**
  - All systems are at room temperature (i.e., 25°C)
- **TLC1**
  - Inner temperature reaches 500°C in 24 h (linear ramp)
  - Heat losses at nozzles are neglected
- **TLC2**
  - 650°C prescribed to each hot leg nozzle area
  - 550°C prescribed to the cold leg nozzle area
  - 250 W heat loss prescribed to each reactivity management nozzle area
  - Vessel outer surfaces are assumed perfectly insulated
  - 550°C prescribed to the shell and bottom inner surfaces in contact with the FLiBe
  - Top head and shell inner surfaces in contact with the cover gas are subject to:
    * Convective heat transfer using a heat transfer coefficient equal to 3 W/(m^{2}K) and a cover gas temperature equal to 650°C
    * Radiative heat transfer, assuming a metal emissivity of 0.6 and a FLiBe temperature of 650°C
- **TLC3** (same as TLC1 [final])
  - The FLiBe and cover gas are kept at 500°C
  - All heat losses at nozzles are neglected
- **TLC4**
  - 816°C prescribed to the hot/cold leg nozzle areas and to the shell and bottom inner surfaces
  - 250 W heat loss prescribed to each reactivity management nozzle area
  - Vessel outer surfaces are assumed perfectly insulated
- **TLC5**

- 550°C prescribed to the hot/cold leg nozzle areas and to the shell and bottom inner surfaces
- 100 W heat loss prescribed to each reactivity management nozzle area
- Vessel outer surfaces are assumed perfectly insulated
- Convective and radiative heat transfers can be maintained, but their effect will become marginal because the cover gas and FLiBe temperatures are equal to 550°C

The loading conditions for each phase are implemented as a separate MOOSE simulation, using restart data from the previous phase. Separate inputs permit convenient restarts in the middle of a transient, enabling the testing of different solver options and time-stepping strategies. The common input file section describing the mechanical constitutive model, simulation outputs, and postprocessing sections are split into yet another separate MOOSE input file. This approach allows for easy modification of the parameters common to all 14 phases of the transient vessel simulation, and of the common inputs for the loading conditions for all available constitutive models. We used the material-based time-stepping method (previously developed for this project) based on effective inelastic strain increments. We also utilized additional strategies to ensure that the maximum inelastic strain increment in a given step does not exceed 0.1%.

One of the mechanical boundary conditions is a torque applied to the hot leg surface. We developed a novel torque boundary condition for MOOSE specifically for this application. The torque is applied pointwise to the selected surface, permitting deformation. Since MOOSE currently offers no support for the type of multi-point constraints that would ideally be used for this appliction, to prevent excessive deformation of the hot-leg side set, we meshed in a plug to fill the pipe opening, and assigned it an elastic material with a high stiffness so that it would effectively behave as a rigid body. By analyzing the mechanical strain, we verified the rigidity of this plug and by extension, of the adjacent surface. Thermally the plug has no effect, as the temperature of the side set is kept uniform by a Dirichlet boundary condition.

We assigned a color to each phase, and used them as background colors in each phase of the time history plots. For the mechanical modeling of the Alloy 316H vessel material, we used two different constitutive models: one based on the ANL-provided NEML, and one that uses the LAROMance ROM for creep deformation being developed by LANL.

In addition to the KP-supplied thermal loading conditions, a modified, less aggressive, version of the loading conditions was created, with all applied temperature differences reduced to 25%. In this scenario, the LOCA in Phase 6 was replaced by normal operation to further decrease the demands on the material models. The result can be seen the in the maximum/minimum temperature plot in Figure 5. This reduced thermal loading condition was applied in simulations with the LAROMance model, because we could not run the original KP-supplied loading conditions without experiencing material model failures with that model. The temperature averages on the nozzle boundaries are grid-converged to within less than 1 °C.

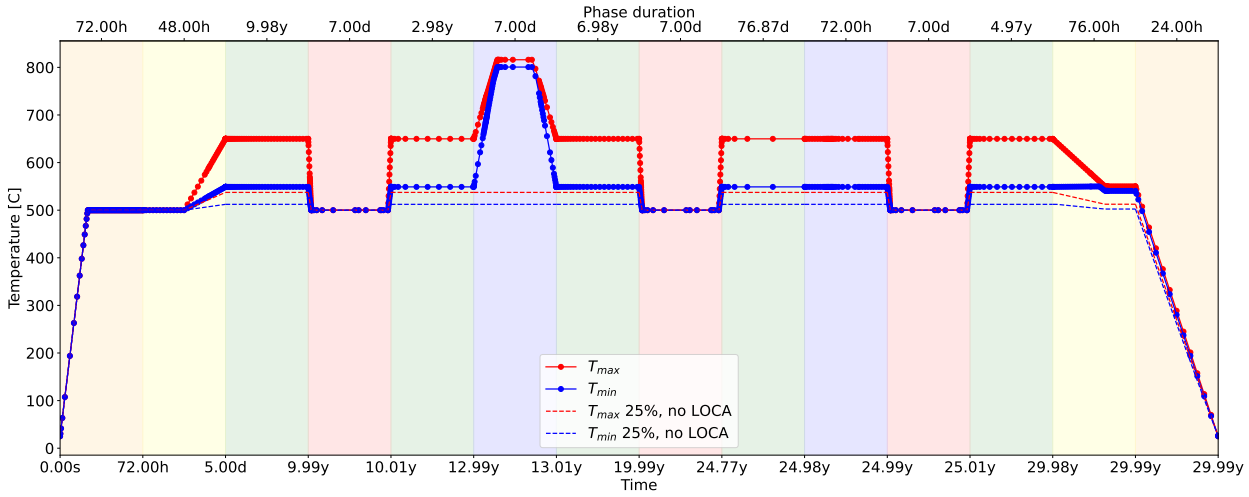

Figure 5: Maximum (red) and minimum (blue) temperature over the full vessel transient simulation—utilizing the November 2022 version of the NEML model at full thermal loading, and from a simulation using the reduced thermal loading conditions and substituting normal operation for the LOCA phase (25%, no LOCA).

Figure 5 uses a variable time axis format, which we also use in other similar time-history plots that follow. Each phase appears on the plot as having equal width by applying constant scaling to the time increments within that phase. The true duration of each phase is labeled along the top axis, and the total time is labeled on the bottom axis. The background colors in the plot correspond to the colors given in parentheses in the enumeration of the different phases near the beginning of Section 2.3.2.

In all simulations utilizing inelastic deformation, models are timestep-size limited by a material-informed metric based on a prescribed maximum inelastic increment of 10^{-4} strain. On top of that are restrictions based on the maximum rate of change of the applied time-varying boundary conditions (e.g., the pressure oscillations in Phase 1). Within these constraints, MOOSE will choose a timestep by either growing or shrinking the previous step size, depending on the number of non-linear iterations required to converge the global solve. Fast global convergence leads to timestep increases, while slow global convergence leads to a cutting of the timestep.

Linear elastic model To verify the simulation loading conditions and input file syntax, we set up a simple linear elastic constitutive model input that can be applied to all 14 phases of the vessel transient. This linear elastic model runs extremely fast and allows for debugging the loading conditions for the entire transient, without the cost of solving for a high-fidelity creep model.

NEML constitutive model Multiple iterations of the NEML 316H model were tested throughout its development over the course of this project. Initial iterations of the NEML constitutive model had issues with the included damage model, which was therefore disabled at that time. Furthermore, in early model iterations, the LOCA in Phase 6 had to be replaced with a normal operation phase. The damage model caused a breakdown of the convergence, due to a failing element adjacent to a cold leg hole. Even with disabled damage model, excessive creep in the vessel wall right below the lid—with strains of up to 30%—were observed during the LOCA phase. These results are shown in early quarterly reports from April 2021.

The performance of the November 2022 version of the NEML model delivered by ANL was considerably

improved. Both the damage modeling and modeling of the LOCA phase converged well. The results from this model are presented here. Figure 6 shows the time history of the maximum von Mises stress in the reactor vessel model, as predicted by this version of the model through all loading phases. Figure 7 shows a similar plot of the history of the maximum effective inelastic strain and maximum first principal component of the inelastic strain. Figure 8 shows the contours of the effective inelastic strain and von Mises stress at the end of the last loading phase. As would be expected due to the loading conditions, the regions near the inlets experience the highest stresses and strains. The peak inelastic strains are somewhat lower than those reported in the time history plot because the quantities plotted are elemental averages, whereas the time history plots take the maximum of all quadrature points. It is also important to note that the inelastic strains predicted by this model are high, but that this simply reflects the fact that the loading conditions are intentionally designed to be more severe than would be expected to exercise the model.

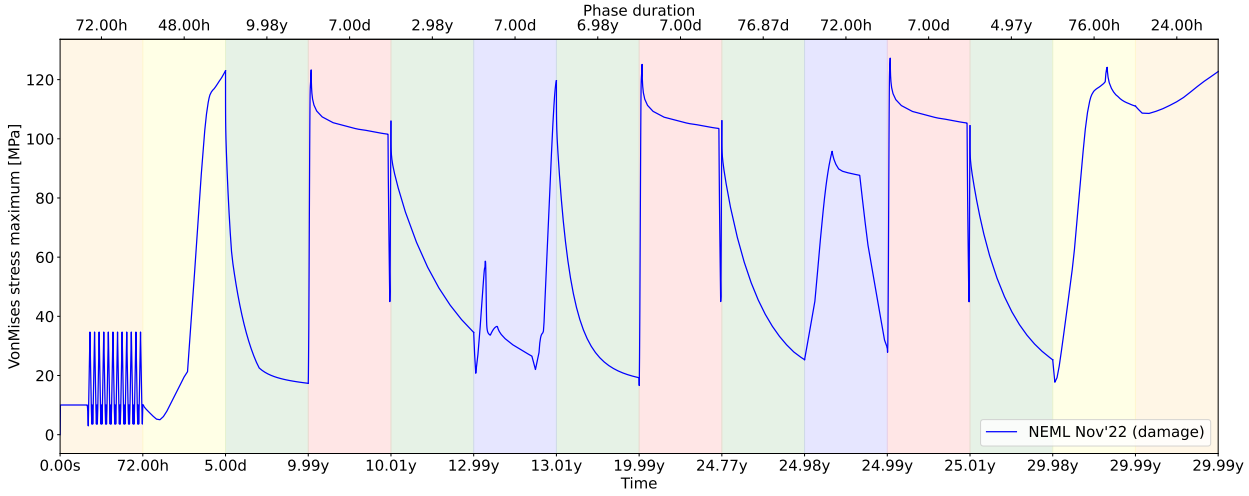

Figure 6: Maximum von Mises stress for the November 2022 version of the NEML model. The effects of the applied pressure oscillations are visible in Phase 1.

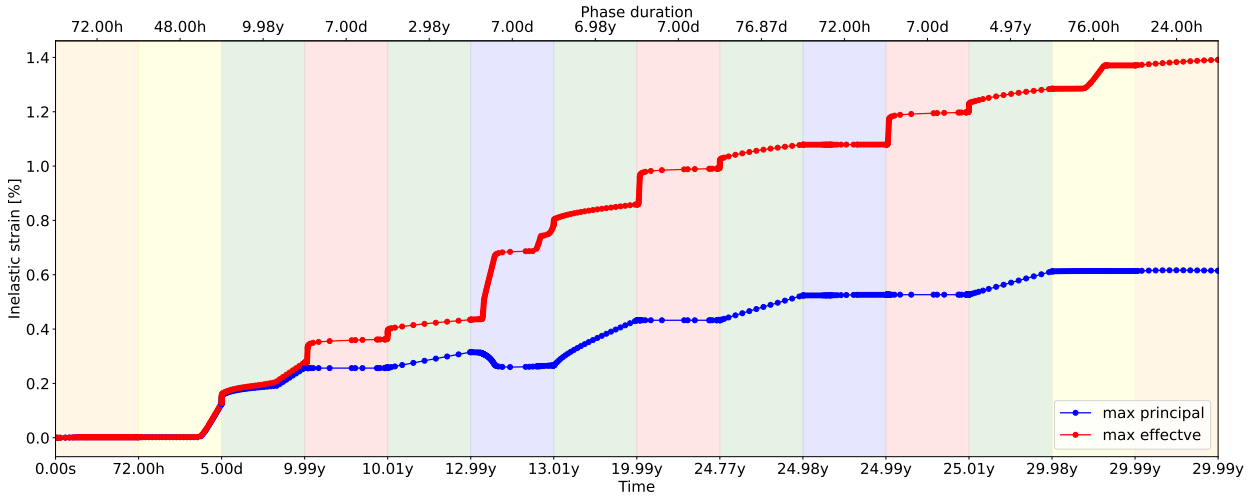

Figure 7: Maximum values of the effective inelastic strain (red) and the maximum principal component of the inelastic strain obtained using the November 2022 version of the NEML model.

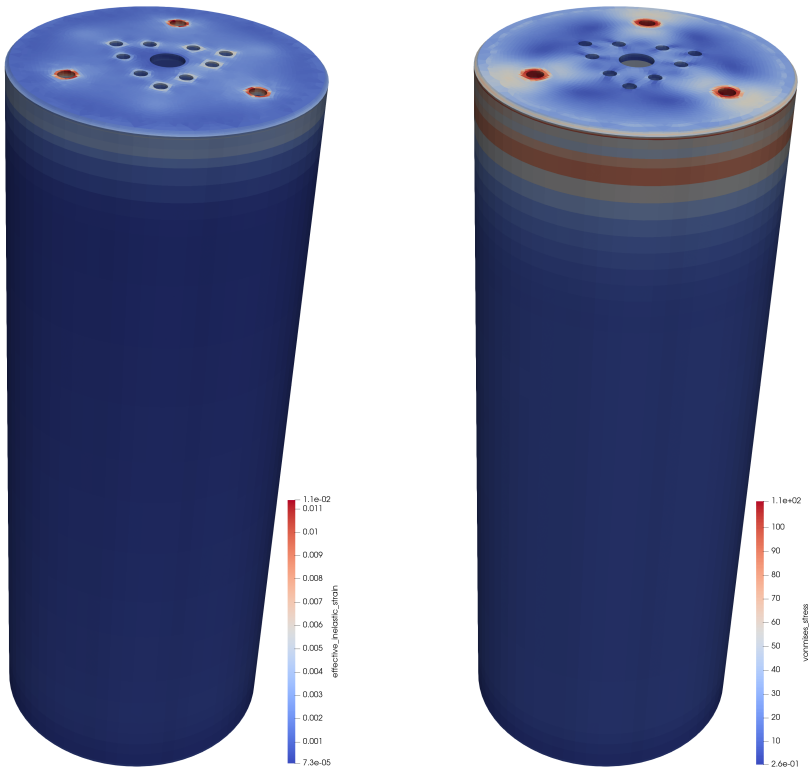

Figure 8: Contour plots of (left) the effective inelastic strain and (right) the von Mises stress for the November 2022 version of the NEML model at the end of the full loading sequence.

In January 2023, an updated (deformation + damage) model calibrated against the full dataset provided to ANL by KP, including the final batch of creep-fatigue data and the full National Institute for Material Science (NIMS) creep dataset, was provided. The previous model did not incorporate the results of the KP tests or the NIMS data acquired by KP, but instead incorporated low-stress calibration with helical spring creep data. In addition, the model was refitted using stochastic optimization approaches.

We experienced convergence issues with the January 2023 version of the model, resulting in the cutting of global timesteps to the point that the simulations would not be completed within the project timeframe. The decision was made to consider the results of the November 2022 version of the model as the final results. We were only able to run the new model without damage until about halfway into Phase 7. In comparing the effective inelastic strain accumulated thus far with that seen in the November 2022 version of the model, the updated model is shown to behave similarly, although it exhibits a slightly higher rate of creep deformation. Future development of the constitutive model will address the convergence issues.

LAROMance constitutive model A series of incremental updates to the LAROMance model were provided to INL over the course of the project, each covering successively larger ranges of the temperature and stress conditions of interest. The latest provided version of the LAROMance model was supplied in December 2022. This version was generated using data from the elastic viscoplastic fast Fourier transform (EVPFFT) polycrystal plasticity code, which, unlike the previous VPSC-based model versions, allows for incorporating damage.

The LAROMance ROMs are a novel development, and as would be expected with any new complex

modeling approach, robustness challenges were encountered when applying them to engineering-scale simulations during this project. Despite the increased range of applicability of the final EVPFFT-based version of the model relative to earlier versions, there were still apparent limitations on the applicability of the model to the range of temperature and stress conditions experienced during the full vessel transient. By the time the final model had been developed to cover the full range of loading conditions, very little time in the project remained for working with LANL to debug failures in internal model convergence. It is important to note that during the nonlinear solution, the iterative solutions exercise the ROM under a broad range of temperature and stress, making the finite element model more demanding of the ROM than might be intuitively expected.

Full vessel transient simulations using the December 2022 version of the LAROMance model successfully ran through Phase 1, which had essentially elastic behavior, but struggled to converge the internal return mapping iterations late in Phase 2 (startup), when inelastic strains began to accumulate. Although the developments described herein (e.g., automated substepping) significantly improved the performance of this model, they were insufficient to run it all the way through the desired loading conditions. The model ultimately experienced global timesteps being cut to time increments non-conducive to completing the simulation within the project performance period.

As stated previously, in an effort to obtain results for a larger set of loading stages, we used a reduced thermal loading condition in which the temperature difference was scaled to 25% of the original loading conditions and the LOCA phase was replaced with normal operation. This reduced loading condition allowed the LAROMance simulations to progress further into the transient (see Figure 9) before failing to converge in Phase 10. Note, however, that the response of the LAROMance model in this regime reflects something very close to linear elastic behavior, since the lower thermal gradients and peak temperatures significantly reduce inelastic behavior.

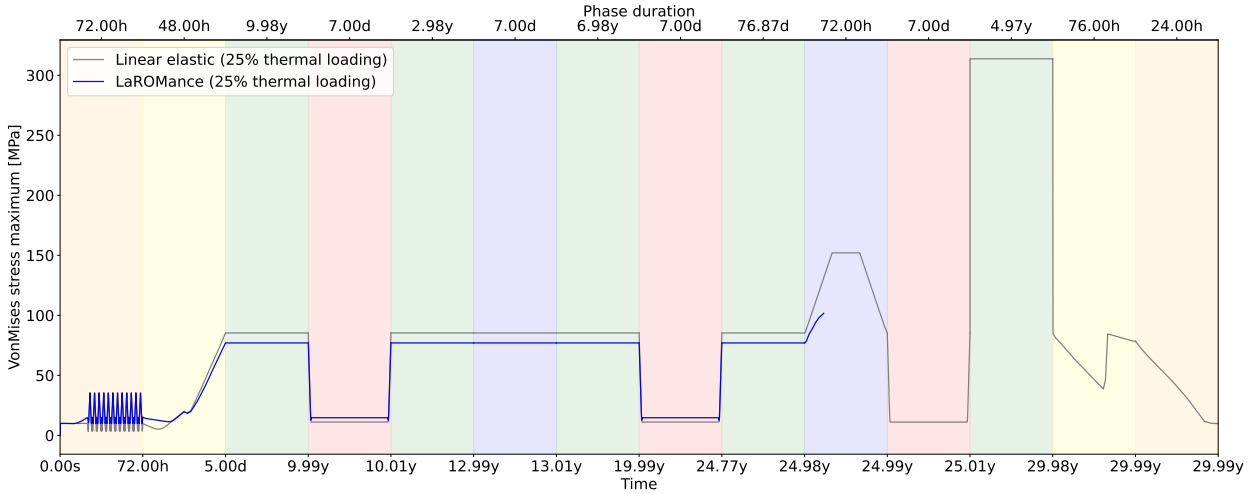

Figure 9: Maximum von Mises stress for the December 2002 version of the LAROMance model compared to a linear elastic model—both with reduced thermal loading conditions applied.

Further development/integration work is needed to improve the robustness of the LAROMance 316H model in MOOSE and thus ensure its applicability over the whole range of conditions that will be experienced in practical applications. However, previous experience with LAROMance models gives confidence that the current convergence issues can be resolved. For example, an earlier (i.e., VPSC-based) version of the LAROMance model for 316H was successfully used in this project to simulate the reactor vessel head, and

LAROMance models for another alloy (i.e., Grade 91) have been run on complex, large-scale 3D component models. Also, as previously noted, the transient considered here is more demanding than the actual expected conditions. In particular the time to failure for 316H drops rapidly above 775 °C, but the LOCA in Phase 6 has a peak temperature of 816 °C, so prior to the aforementioned adjustments to the temperature conditions, Phase 6 exposed the reactor vessel to this problematic temperature regime.

2.4 Discussion on Convergence Challenges

As previously discussed, iterative development of both classes of constitutive models occurred over the course of this project, and robustness issues with both the NEML and LAROMance models were faced at various times. Most often, these issues were rooted in challenges with converging the return-mapping iterations performed within the material models. Multiple options are available for performing adaptive time stepping, both at the local and the global material point level. This is done both to minimize integration errors and to recover from convergence failures.

Plots of timestep size over the course of the analyses are telling indicators of the difficulty faced by a given model. Figure 10 shows a comparison plot of the timestep size during the reactor vessel analyses under the full loading conditions. This shows results for multiple versions of the NEML model, including the November 2022 version, which ran robustly, and the January 2023 version, which had more challenges. The LAROMance model and the linear elastic model, which had no local material integration, are shown for comparison purposes. The November 2022 NEML model was successful in taking very large timesteps, which is the desired behavior. The problem areas for the other models are clearly evidenced by the small timesteps taken.

While the adaptive time-stepping strategies implemented for this project help significantly improve robustness, when local material points require small timesteps, it is very challenging to obtain an efficient and robust solution. Convergence issues are often caused by a lack of smoothness in the material constitutive behavior, and are expected to be resolvable with further effort.

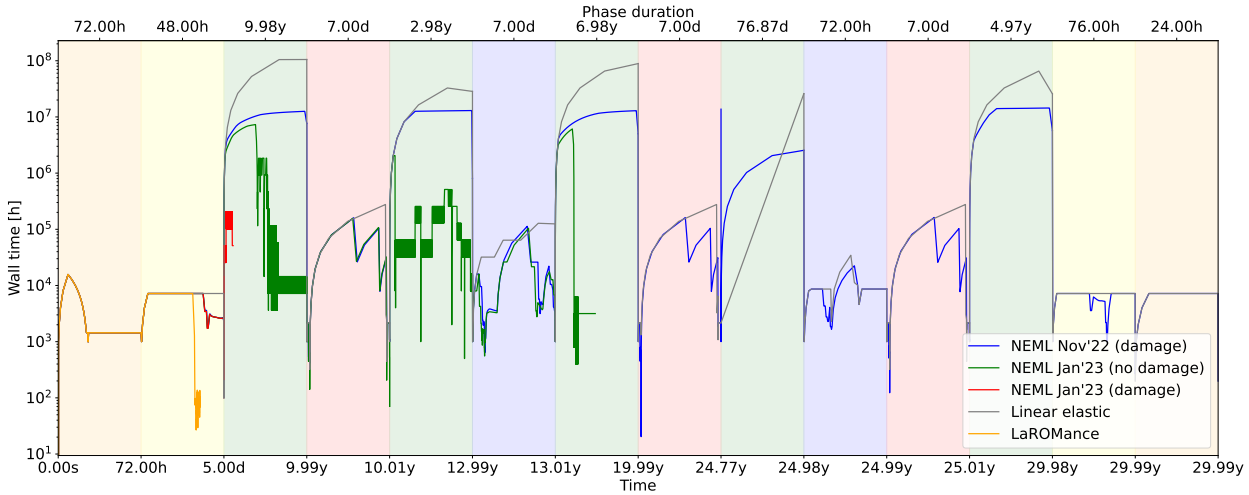

Figure 10: Simulation timestep size comparison for the various constitutive models and their different versions.

2.5 Conclusions

To support the application of advanced constitutive models to simulate realistic structures such as the reactor vessel, INL integrated the NEML- and LAROMance-based models for 316H into MOOSE-based codes. INL also developed capabilities in MOOSE to both streamline the process of setting up a complex full vessel transient thermo-mechanical model, and to improve the performance of the global solve.

To test these capabilities, INL developed a model of a simplified, modified reactor vessel, then ran it using both the NEML and LAROMance 316H models in the MOOSE-based codes. The NEML-based model successfully ran all load phases to completion, and indicated significant inelastic strains due to the challenging loading conditions. Because of convergence issues that occur under significant inelastic strains, the thermal gradients had to be scaled back for the LAROMance-based model to run through multiple stages.

Most model failures were found to have been due to convergence issues within the material point iterations, not to global solution issues. Those convergence issues caused the material-point and global timesteps to be cut to the point of becoming too small to obtain practical results. With further development targeted at addressing the robustness of the material iterations, it is expected that both classes of these models can serve as useful tools for engineering-scale simulations of high-temperature 316H components.

3 CREEP-CRACK GROWTH ESTIMATION ACCORDING TO CODIFIED ASSESSMENT PROCEDURES

This section describes the progress made to capture crack growth rates and accumulated crack sizes in the MOOSE/Grizzly environment, as per the technical report ASME STP-PT 89 [30]. Three MOOSE postprocessors were created to reproduce the steps followed in three different methodologies (i.e., R5 V4/5, Electric Power Research Institue (EPRI) Boiler Life Evaluation and Simulation System (BLESS), and American Petroleum Institute (API) 579) to obtain creep and fatigue crack growth rates. Here, we describe the verification of the vessel stress evolution and the CCG rates for the operating conditions and crack types outlined in Section 7 of [30].

3.1 Verification of stress analysis

As a first step, a transient stress analysis simulation was performed to verify the MOOSE/Grizzly results. Linear elastic stress and the generalized plane strain formulation were employed. The generalized plane strain formulation introduces an extra degree of freedom to capture strain and stress in the out-of-plane direction. This is useful for capturing axial stress when considering a 1D axisymmetric problem. The number of elements through the vessel thickness, boundary conditions, geometry, operating conditions of pressure and temperature, and temperature-dependent material properties (Young's modulus, thermal diffusivity, thermal conductivity, specific heat capacity, and coefficient of thermal expansion) dependent on temperature are taken from Sections 1 and 2 of the technical report ASME STP-PT89 [30]. The properties of Grade 22 steel were manually parsed from plots provided in the ASME report. The transient results for the Grade 22 steel superheater pipe (SHP) undergoing cold startup operating conditions are shown in Figures 11 to 13, which also compare the Grizzly results with reference solutions taken from STP-PT89.

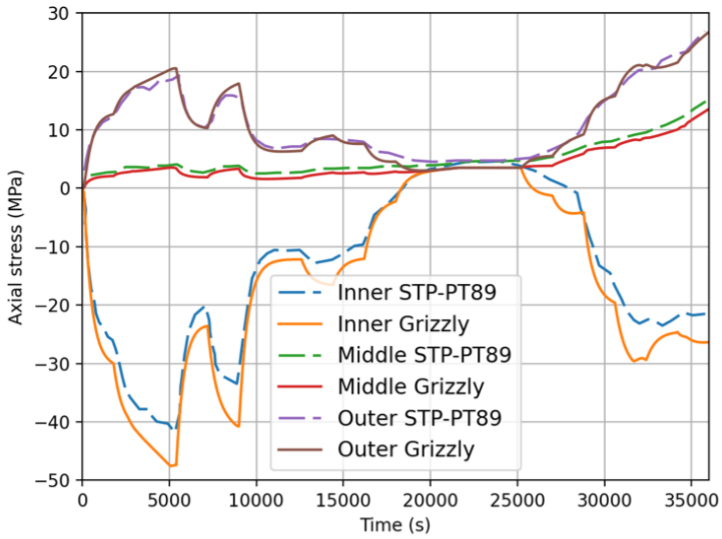

Figure 11: SHP Grade 22: Axial stress at the inner, middle, and outer points. The digitized results of STP-PT89 (Figure 3-7 therein) are used as reference solutions.

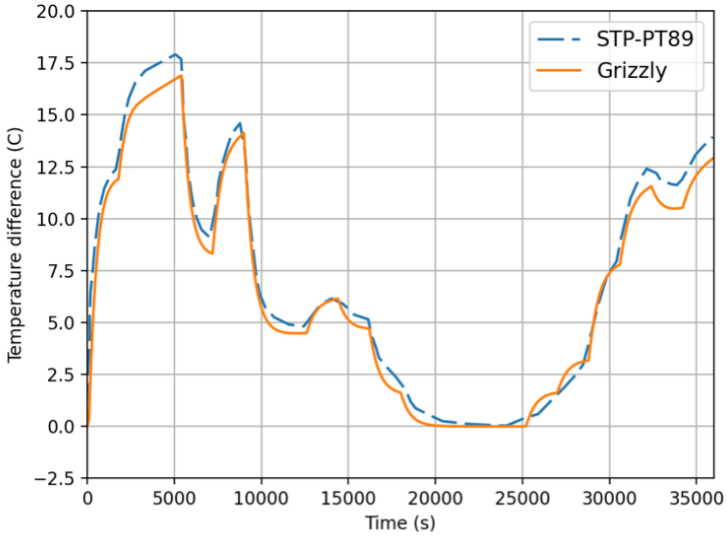

Figure 12: SHP Grade 22: Temperature difference through the vessel thickness. The digitized results of STP-PT89 (Figure 3-8 therein) are used as reference solutions.

The differences between the reference results and the Grizzly results in Figures 11 to 13 may be attributed to errors incurred while parsing material properties from plots or digitizing the reference results, in addition to other modeling discrepancies. These transient results may be obtained for any set of operating conditions, including cold/warm/hot startups and shutdowns. In Grizzly, this is called the "global" problem, in which a stress distribution through the vessel thickness may be outputted for later processing to compute stress intensity factors (SIFs), crack growth rates, or accumulated crack dimensions.

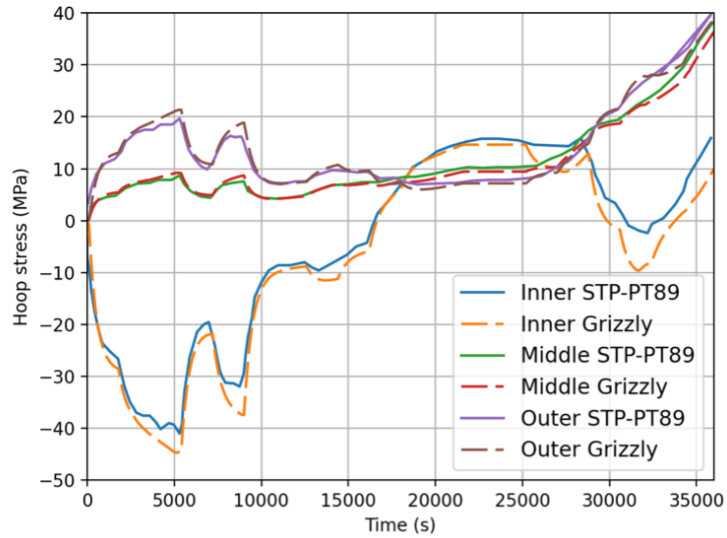

Figure 13: SHP Grade 22: Hoop stress at the inner, middle, and outer points. Digitized results of STP-PT89 (Figure 3-7 therein) are used as reference solutions.

3.2 Computation of C* per "manual" assessment procedures

In this section, we outline manual methods for CCG characterizations based on reference stresses.

3.2.1 Reference stress method for estimating C*

Predictions of crack growth due to creep often rely on a C* parameter calculation. Although its meaning and practical use are further discussed in Section 4.5.2, here we briefly introduce how this quantity is approximated in assessment methodologies (e.g., R5 [25]). (Other codes such as EPRI BLESS and API-579 follow analogous derivations.)

If a load is constant, the value of C* can be estimated by the following equation:

$$C^* = \sigma_{ref}\dot{\epsilon}_{ref}R', \tag{1}$$

where σ_{ref} is the reference stress (whose calculation depends on the loading/boundary conditions), $\dot{\epsilon}_{ref}$ is the reference strain rate, and $R' = \frac{K^2}{\sigma_{ref}^2}$ is a length parameter. The reference stress is computed based on primary loads, which cannot be relaxed. In general, the reference stress can be computed as $\sigma_{ref} = \frac{P\sigma_y}{P_L(a,\sigma_y)}$, where σ_y is the yield stress and P_L is the load of plastic collapse. See [26] (among others) for a detailed account of the steps in the R5 code using the reference stress method.

3.2.2 Simplified estimation of C* under displacement control

A simple method to estimate the value of C* that is suitable for inclusion in methodologies such as R5 was proposed in a technical report [2]. This method is strictly applicable only for displacement control. The derivation can be described as follows:

$$\dot{\Delta} = \dot{\Delta}_{el} + \dot{\Delta}_{cr} = 0, \tag{2}$$

where $\dot{\Delta}$ is the overall load-line displacement rate, and $\dot{\Delta}_{el}$ and $\dot{\Delta}_{cr}$ refer to its elastic and creep constituents, respectively. The elastic load-line displacement may be obtained by instantaneously computing the overall load and its rate:

$$\dot{\Delta}_{el} = \frac{\dot{P}}{P}\Delta_{el}, \tag{3}$$

where P is the instantaneous load. This value may be readily computed from numerical and laboratory experiments. The other contribution to the overall load-line displacement is $\dot{\Delta}_{cr}$, which can be decomposed into two contributions:

$$\dot{\Delta}_{cr} = \dot{\Delta}_{cr}^{c} + \dot{\Delta}_{cr}^{uc}, \tag{4}$$

where $\dot{\Delta}_{cr}^{c}$ and $\dot{\Delta}_{cr}^{uc}$ represent the cracked and uncracked volume contributions to the creep load-line displacement rate. $\dot{\Delta}_{cr}^{c}$ can be determined from CCG estimation methodologies such as the one based on a reference stress. Equations 2–4 enable determination of the rate at which the load drops—and thus also the load as a function of time. Once the instantaneous σ_{ref} is obtained, C* is readily available. The reference stress rate is a function of the load rate $\dot{P}$ and can be expressed as:

$$\dot{\sigma}_{ref} = \frac{E\dot{\epsilon}_{ref}}{Z}. \tag{5}$$

For complex creep-fatigue operating conditions (i.e., secondary loading), Equation 5 is typically employed using the conditions at the outset of a dwell period. For such cases, Z is a follow-up factor, often chosen as 2 [3].

3.3 Verification of CCG rates

3.3.1 Background

A detailed description of the calculations needed to obtain CCG rates is provided via "hand" calculations in Section 7 of [30]. The case discussed here is that of a reheater pipe made of Grade 22 steel and applied to a 360° (infinite) circumferential crack. This particular case is used to verify Grizzly's implementations.

Calculation of creep growth rates requires the pre-computation of the axial stress for the Grade 22 reheater pipe under full operating conditions. These reported results match reasonably well with Grizzly, which computes a constant axial stress of 17.57 MPa. The difference between these solutions is within round-off error. In addition to this computed stress, other conditions and material properties are used as inputs to the problem.

In Grizzly, we approached this problem using the following steps (see Figure 14):

1. The generalized strain 1D axisymmetric global problem is solved in Grizzly, and its output in terms of the evolution of axial/hoop stresses and temperature is written to comma-separated value files.
2. For this section, the last value representing the axial stress steady-state solution (17.57 MPa) is used as an input to the local problem, where the crack geometry is introduced. The existing implementation of SIF influence coefficients in Grizzly is leveraged to compute SIFs for surface-breaking cracks.
3. Finally, computations of reference stresses, material damage, omega model, SIFs, and crack growth rates are performed in a MOOSE postprocessor that then outputs the crack growth rate in units corresponding to the given methodology.

Similar steps are followed in each of the three methodologies described, with one exception: while API 579 and R5 4/5 rely on the Grizzly SIF influence coefficients [69], even if constant stress through the thickness is assumed, the EPRI BLESS methodology requires the implementation of SIFs obtained by equations from Zahoor [114] and Buchalet [16], which were added to the code for this purpose but still remain largely unverified. Manual C^* calculations are based on the reference stress method (see Section 3.2). CCG results from Grizzly are compared to those in [30] below.

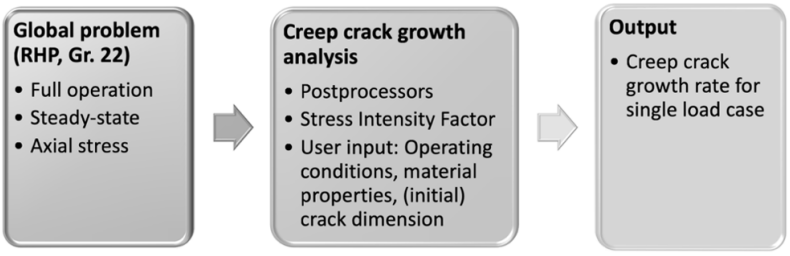

Figure 14: Simplified workflow in Grizzly to computing CCG rates. The first step involves transient stress analysis, and the second calculates the stress references and strain rates that finally yield the growth rate.

3.3.2 API 579 methodology

The global problem results (i.e., constant through-thickness axial stress) are the same for all three methodologies. Code-wise, the core computations are performed by MOOSE postprocessors. An example

of the parameters that must be provided is shown in Figure 5.

```
[Postprocessors]
    ...
    [fatigue_crack_growth]
        type = API579CrackGrowthRateReporter
        ki_calculator = ki_calculator
        vessel_geometry = vessel_geom
        single_flaw_data = flaw_data # crack definition and geometry
        internal_pressure = 0.7 # 0.7ksi-in
        A_material_parameters = '-21.860 51635.0 -7330.0 -2577.0 0.0'
        B_material_parameters = '-1.85 7205.0 -2436.0 0.0 0.0'
        t_eval = 1005.0 # F, operating temperature
        t_ref = 460
        E = 24671.0 # Young modulus at operating temperature
        length_unit = M # Required to convert vessel geometry data
        ki_unit_convert_from = PA_SQRT_M # Required to convert ki calculator result
        t_h = 28.169 # Hold time in hours for creep calculations
    []
[]
```

If not prescribed in the input file, the postprocessor will only compute a growth rate, and will not accumulate the crack growth size increments. In Figure 5, the user is assumed to know all the material parameters in the proper units that correspond to the selected methodology. The CCG rate computed by Grizzly is 2.388e-06 in./hour, whereas [30] reports 2.455e-06 in./hour—a 2.7% difference.

3.3.3 R5 V 4/5 methodology

An analogous workflow is followed to obtain the crack growth rate using the R5 V4/5 methodology. In this case, Grizzly reports a growth rate of 2.048e-06 mm/hour, whereas the reference is 2.108e-06 mm/hour—a difference of 2.8%.

3.3.4 EPRI BLESS methodology

In the EPRI BLESS methodology, a UO is developed to compute the SIF, as per the steps presented in Section 5 of [30]. This is because this methodology employs different approaches for computing different types of cracks. In this case, Grizzly reports a crack growth rate of 5.823e-07 in./hour, whereas the reference is 5.822e-07 in./hour. This small difference of 0.02% is probably due to round-off errors. The fact that this difference is smaller than those for the other two cases may be explained by the fact that ad hoc SIF equations were implemented, whereas the other two methodologies rely on coefficient interpolations.

3.3.5 Conclusions

This section showed that, for the case tested, Grizzly accurately reproduces the steps and computations given in Section 7 of [30] for determining CCG rates. The slight difference in the results is mostly due to small differences in the computed SIF, which is a necessary intermediate quantity.

4 FEM-BASED CONTINUUM DAMAGE MECHANICS MODELING OF HIGH-TEMPERATURE FLAW PROPAGATION

4.1 Introduction

The prediction of creep and creep-fatigue crack growth at high temperatures (e.g., ∼>500 °C for austenitic stainless steels) is a key aspect in both the design and defect assessment of metallic components in power-generating equipment operating at such temperatures. For nuclear energy, there currently is a strong interest in the development of novel Generation IV reactors (e.g., gas-cooled fast reactors and molten-salt reactors), and the majority of the concepts being pursued worldwide will operate under temperature regimes in which creep is a dominant deformation and failure mechanism. Crack-like defects could initiate in metallic structural components at high temperatures, thus challenging the design and safety functions of the nuclear-power-generating asset [28, 37, 40, 106].

Factors that dictate crack initiation and growth are closely associated with the life-limiting nature of creep deformation and fracture (see [67, 96, 109]). While the notion behind the combined effect of creep-fatigue failure and crack propagation is closely linked to the alternating loads and dwell periods experienced during typical plant operation, the CCG phenomenon is of key importance. CCG under either load- or displacement-controlled conditions results from the continuous agglomeration of microcracks [52, 109], which tend to initiate and grow in an intergranular manner as a result of the continuous coalescence of creep cavities [19, 82, 104]. Due to the nature of this process and its relatively low nucleation thresholds [27, 89], CCG is difficult to avoid in high-temperature systems, as noted by Holdsworth [45]. In addition, Spindler et al. [101] demonstrated the predominance of CCG as a contributing mechanism to creep-fatigue crack growth in assessments of typical operating histories for power-generating units, with creep cracking during long-term dwells in excess of 1000 h being a more dominant contributor than fatigue cracking due to alternating loads.

The CCG phenomenon is a common and important life-limiting process in components subjected to elevated temperatures and typical operational loads. Therefore, to determine the evolution of an existing crack under an imposed loading, the thermal-hydraulic operating conditions, material properties, and defect configuration are relevant for conducting life assessments of components experiencing creep conditions. In practice, multiple CCG assessment methods are used to capture the continuum mechanics of the process and their relationship to the prescribed loading conditions in the vicinity of the defect. These are briefly discussed below.

This section of the report is organized as follows: Section 4.2 summarizes the methods used in practice for predicting CCG. Section 4.3 provides a brief background on the finite element software employed in this work. The models used to capture the engineering-scale creep, plasticity, and damage of annealed and service-exposed (thermally aged) 316H at 550–650 °C are detailed in Section 4.4, which also provides material model parameters. CCG characterization often relies on computation or estimation of the C(t) domain integral. In the present work, two strategies are employed for this task: a fully computational approach based on creep strain rate and stress fields around the crack front and a fracture domain integral, and one employing ASTM E-1457 formulae for estimating C(t) for various geometries and material model parameters [31]. These procedures for estimating C(t) are detailed in Section 4.5. The finite-element-based methodology leveraged in this work to implement the computational scheme for deformation and damage is described and demonstrated in Section 4.6. The CCG modeling methodology is then employed for a variety of loading conditions, boundary conditions, geometries, and structural components (including an industry-relevant component), with numerical predictions being compared to experimental data, when available, in Section 4.7.

4.2 Survey of CCG Prediction Procedures

4.2.1 Assessment of CCG via high-temperature flaw evaluation methods, and the significance of domain integrals

In industrial practice, defects in high-temperature components are generally treated within consensus-based methodologies for demonstrating Fitness-for-Service (FFS) or defect tolerance [42]. Examples of FFS-type defect assessment procedures extensively applied within the nuclear and oil industries include the United Kingdom's R5 assessment procedure [25], API-579 (ASME FFS-1) [5], and EPRI BLESS [39]. Note that defect tolerance procedures for structural integrity differ from construction codes in that the methodologies for elevated temperature design-for-construction (e.g., within ASME Boiler and Pressure Vessel Code [BPVC] Section III, Division 5 or the French RCC-MRx) do not explicitly consider the presence and propagation of life-limiting defects. Recently, ASME BPVC Section XI, Division 2—which defines requirements for surveillance programs conducted for non-light-water reactors—has progressed in terms of defining methods for high-temperature flaw evaluations by using an approach that combines best practices from [25] and [5]. Despite the differences in these various codified procedures, they all place a high priority on assessing the effects of crack-like defects on the integrity of industrial structural components. The steps for applying these procedures to general crack-like defects are discussed in the following text, with an emphasis on failure due to steady-state creep rather than fatigue.

Since the inception of linear elastic fracture (LEFM) mechanics (see Irwin [51] and Griffith [36]), this theoretical approach has been validated and applied to assessments of brittle unstable fracture in both metallic and non-metallic materials. The central concept of LEFM is the relation between the critical SIF, K_{Ic}, and the crack size, a, due to the elastic displacement field surrounding the crack, which contributes to crack growth by releasing stored energy in the creation of a new crack surface:

$$K_{Ic} = \sigma_c Y \sqrt{a\pi}, \tag{6}$$

where σ_c is the value of the far-field stress that results in propagation of a crack of length a, and Y is a geometrical parameter that depends on the loading and the structural component geometry. For brittle materials in which the field surrounding the crack is largely elastic and the size of the plastic zone, r_p (i.e., $r_p > f(\sigma_c)$, where f denotes a general function), is limited, fracture toughness is typically used to characterize the crack response (e.g., in RSE-M and R6). Ductile materials are generally preferred for power-generation equipment, which motivates the extension of LEFM to elastic-plastic fracture mechanics (EPFM) for these types of applications. EPFM accounts for the elasto-plastic response ahead of the crack tip in an isolated plastic process zone, and is widely adopted in practice within the nuclear industry [43, 93]. EPFM methods are well established and codified, and generally adopt a combination of non-linear fracture mechanics theory and material properties that characterize the crack extension [93]. The J-integral, developed by Hutchinson, Rice, and Rosengren [46, 87], is a contour integral typically used to quantify the energy release rate for a given increment in crack growth. The basis for deriving the J-integral stems from the dissipation of plastic work ahead of the crack as well as the energy required to create an increment in the crack surface. It is defined as:

$$J = \int_{\Gamma} W \cdot \mathrm{d}x_2 - T_i \frac{\delta u_i}{\delta x_1} \cdot \mathrm{d}s, \tag{7}$$

where W is the strain energy density of the material; x_1 and x_2 are problem coordinates defining the direction of crack advancement and the direction perpendicular to the crack plane, respectively; T_i is the surface traction on the crack face; u_i is the displacement vector; Γ denotes the closed curve encompassing the crack tip area; and s is a distance along the curve.

Application of this fracture mechanics integral to ductile materials, for which the material local plastic energy is much larger than the material's local elastic energy, dictates that:

- A limiting value of fracture toughness, J_{Ic} (denoting the onset of stable tearing), exists
- The subsequent crack extension da for an increase of dJ is dictated by the J-resistance curve.

The EPFM approach enables predictions of crack propagation in ductile materials [38, 61]. For example, such methods have been applied to existing light-water reactors for temperatures of < 350°C to assess limiting defect sizes. A combination of EPFM methods for the onset of stable tearing with fatigue crack growth are employed to inform structural integrity claims.

In the 1970s, successful application of the J-integral to predict the onset of crack propagation in ductile materials caused a growing interest in the application of its time-dependent form, the C(t)-integral. Developed by Landes and Bagley [14] and Nikbin et al. [74], this integral can be defined as:

$$C(t) = \int_{\Gamma} \dot{W} \cdot \mathrm{d}x_2 - T_i \frac{\delta \dot{u}_i}{\delta x_1} \cdot \mathrm{d}s, \tag{8}$$

where $\dot{W}$ is the strain energy density rate and $\dot{u}$ is the displacement field rate. The C(t)-integral provides the generalized solutions for the stress (σ_{ij}) and strain-rate ($\dot{\varepsilon}_{ij}$) singularities ahead of a steadily growing crack front. The rate of energy release—characterized via C(t) values—for a given measured crack growth rate, is typically correlated to experimental data [49, 65]. This is then used to characterize CCG in other cracks in that same material: $\dot{a} \sim f(C(t), k)$, where k is a generic material- and constraint-related parameter.

Steady-state solutions for $\mathrm{C}^* = C(t) \mid_{t \to \infty}$ have been found to successfully characterize the long-term steady-state CCG rates in metallic materials such as American Iron and Still Institute (AISI) 3xx series steels. With the introduction of the C(t)-integral method to engineering assessments of defects, practical methods and solutions for C* [72], its transient forms over a redistribution period [8], transient solutions for combined primary and secondary loads [1], and their relation to crack growth [22, 71] under displacement- or load-control became widely accepted as proven approximate methods for use in life assessments. Standardized testing methods, solutions for crack growth rates as a function of crack mouth opening displacement (CMOD), and C* values under creep are given in [31]. A more detailed review of the extension of the C(t)-integral solutions to mixed-mode conditions can be found in Elmukashfi and Cocks [32]. At present, the C*-integral-based approaches remain the internationally accepted basis for flaw evaluations in creep-dominated, high-temperature conditions.

The procedures for high-temperature flaw evaluation prescribed in R5 and API-579 adopt similar approaches for determining crack growth rates. These are applied during creep-fatigue crack growth assessment, which combines the contributions from both creep- and fatigue induced crack growth over a given load history. A limiting amount of crack growth, a_c, is generally dictated by the onset of stable tearing and/or fast fracture as a function of the J-integral or SIF. For example, the R5 procedure [33] provides a two-step approach to determining the remaining life of a structural component subject to creep and fatigue. Volume II/III of the procedure establishes the propensity for local failure initiation, as well as provides evaluation procedures to prevent global failure modes such as plastic collapse and ratcheting. For cases in which local failure is deemed likely or defects have been observed or postulated in service, an assessment can proceed with the application of Volume IV/V of the procedure, which provides a method of assessing incubation times and the growth of defects under creep or creep-fatigue conditions. In the R5 code [33], a step-by-step approach is used to simplify crack growth prediction models. This methodology can be loosely summarized as follows (see, for example [15] for more details):

1. Characterize the initial defect and past/planned service conditions (pressure and temperature).
2. Define the parameters for material elastic and inelastic response (including creep and time-independent plasticity), as well as those for elasto-plastic fracture mechanics.
3. Perform elastic analysis of a defect-free component to derive inputs for reference stress methods [108], and assess the significance of creep-fatigue interaction, including an assessment of instability.
4. Calculate the rupture life and limiting crack size for the structural component's expected lifetime.
5. For the resolved loading, defect configuration, and reference stress, compute incremental crack growth due to creep as a function of C^*, and incremental fatigue crack growth as a function of cyclic changes in the effective SIF and loading cycles over time.
6. Consider the interaction between creep and fatigue cracking.
7. Recalculate the adjusted limiting crack size and repeat the previous three steps until the limit values are reached.

In general, application of the above procedure yields satisfactory results for predicting the lifetimes of metallic components [12]. Proven experience with these procedures, as well as those of the similar API-579 methodology, provide rationalization for the ASME BPVC Section XI methodologies to adopt a similar approach. However, application of these procedures requires numerous assumptions, some of which may be challenging to validate, and some practical cases may fall outside the bounds of the prescriptive code. These codified procedures involve a number of assumptions of specific conditions, which limit their ability to account for mixed-mode cracking, multiaxiality in the stress fields, the influence of boundary conditions (e.g., load- vs. displacement-control, with the latter involving stress relaxation near the crack tip), complex 3D geometries (and the challenge of linearizing stresses for such configurations), multi-material interfaces near cracks, the generalization to arbitrary primary (load-based, not self-limiting) and secondary (constraint-based, self-limiting) local stress states and dynamic loading sequences. Some of these assumptions, while pragmatic in nature and enabling the user to support structural integrity claims, could often result in conservative predictions.

4.2.2 Numerical modeling approaches to CCG

Despite the increasing maturity of codified FFS procedures such as R5 [25], there is still interest in detailed finite element modeling of CCG to support the enhancement of those procedures and to assess practical scenarios that involve a large set of assumptions that must be made when applying those procedures. Most FFS procedures allow for an integrated approach to defect assessment, with both analytical defect assessment procedures and numerical deformation and failure models complementing each other (e.g., estimation of the J- or C^*-integral via elasto-plastic modeling). Of note is an ASME Code Case, currently under development, on ASME BPVC Section XI [4] that allows for inelastic deformation models to be employed for characterizing crack growth due to creep. By providing virtually complete freedom in choosing the structural component geometry, crack size and shape, and boundary conditions, computational tools could potentially provide further insights into the assessment of component lifetimes, which is required for continued plant operation and the justification of safety case claims. In practice, application of such frameworks requires the use of (a) elasto-viscoplastic models for deformation and (b) damage modeling frameworks calibrated to extensive material databases. This flexibility facilitates analyses of complex scenarios that could be encountered in

practical structures, which are explored in this section by adopting a simple class of models that combine rate-independent and rate-dependent deformation models with a ductility-exhaustion-based continuum damage mechanics (CDM) model.

Various modeling techniques have been proposed to simulate the mechanical response ahead of a planar crack under creep conditions, the objective being to characterize the stress and strain fields ahead of the crack, along with its growth rate and trajectory. These permit accurate characterization of the crack's response under arbitrary conditions. Early work in this area included that of Riedel and Rice [90], who, through time-dependent stress analyses, developed solutions for the creep strain and stress fields ahead of the crack in a steady-state creeping solid. Later work by Hutchinson [47] considered similar solutions by accounting for the effect of cavity growth at the crack tip. These solutions were extended by Tang et al. [104] to also include cavity nucleation.

Finite element modeling of creep failure typically requires that damage be tracked as a quantity that accumulates over time. Various approaches for defining the evolution of damage as a function of stress or inelastic strain involve stress-based (see, for example, [54]) and strain-based ductility-exhaustion criteria [73]. Under the assumption that crack initiation and propagation are due to the accumulation of damage, finite element models can capture crack growth by reducing the ability of material points to withstand loading. In other words, a sharp reduction in stress at material points whose accumulated damage has reached a specified threshold will prompt the growth of a finite element crack. Non-linear FEM solutions for the equilibrium stress fields ahead of a crack under creep have also been produced and analyzed, demonstrating agreement with theoretical estimates [17]. The earlier approaches were extended to account for the propagation response of an advancing creep crack. Notably, Bassani and Hawk [13] evaluated the asymptotic fields ahead of a damaged crack in accordance with a Kachanov-Rabotnov formalism, while Murakami et al. [70] employed a local approach within FEM to examine CCG via CDM. These methods afforded the flexibility to evaluate crack propagation at or near anisotropic material interfaces, as well as to study the transition from transient to steady-state crack growth [44, 113]. Several studies simulated the bulk response of a creep crack by capturing the microcracking process in a simplistic polycrystalline model ahead of a macroscropic crack [76]. Such approaches attempt to explicitly consider the isolated fracture process zone ahead of the crack via a coupled bulk-interface element approach within continuum plasticity. Such FEM techniques are generally expensive; several researchers have pursued explicit modeling of cracks via cohesive-zone modeling techniques in which the micromechanics of the creep cavitation and microcracking process are embedded in the interface response [32]. These approaches successfully describe the progressive crack extension and CMOD rates but generally require a priori knowledge of the crack path.

In practical applications, studies documented in the literature typically evaluated the CCG response in standardized specimen geometries of common alloys employed in high-temperature structural applications (e.g., 316H stainless steel and 9Cr ferritic steels) via CDM models. Successful application of these approaches to compact tension (CT) specimens was shown by Hyde et al. [48], Oh et al. [75], and Wen et al. [110]. Particular attention was paid to the latter two studies, in which the employed frameworks adopted engineering-scale failure parameters whose sensitivity was informed by macroscopic observations and micromechanical aspects (e.g., ductility-exhaustion models as a function of local triaxiality, which is closely related to void growth under a multi-axial stress state [100]). Recent studies, as well as failure initiation assessment approaches applied in industrial practice, demonstrate that ductility-exhaustion measures of damage accumulation provide a more realistic picture of degradation under creep [100, 111]. The ductility-exhaustion criterion has been employed to drive crack growth and creep fracture simulation in several works [56, 58, 75].

Recently, CDM models have been applied to examine CCG within polycrystalline arrays. Compared to interface-based modeling techniques for CCG (e.g., cohesive-zone models), CDM numerical techniques

for crack propagation do not typically employ a discrete representation of a planar defect. We also note that modeling techniques such as the phase-field method provide an enhanced representation of a diffusive crack interface, without the need for a predetermined crack path profile. Examples of this approach in the recent application of irreversible phase-field models to cracking problems in metallic materials that adopt macroscale-relevant damage parameters can be found in Kimura et al. [59] and Khalil et al. [55], both of which focus on fatigue crack propagation under practical loading conditions.

From an engineering perspective, application of techniques that entail explicit modeling of the crack interface generally requires prior knowledge of the crack path, whereas CDM models informed by the mesoscale phenomena of creep cavitation require extensive data and validation before such techniques can be applied to plant components and engineering assessments. From a finite element methodology perspective, meshing of an existing crack into an arbitrary geometry can be challenging. Mesh-cutting algorithms, often used in conjunction with extended FEM, can be employed for this purpose [60, 78]; one such algorithm is used here to consider a crack in a pressure vessel (see [53] for details). Phase-field modeling can be computationally expensive, which has practical implications on scaling of analysis for engineering systems ([105]). The prospect of simplified CDM model frameworks such as those based on triaxiality sensitive ductility exhaustion are therefore appealing, as they can allow:

- Adoption of easily measurable macroscopic properties bearing some features of the underlying material state
- Coupling such macroscopic properties to simple defect assessment procedures
- Usage of FEM solvers that are widely available and have been benchmarked and used in practical industrial applications.

Application of the discussed CCG CDM approaches to other loading conditions typical of plant components or plant component geometries has not been extensively explored. We also stress that the sensitivity of the failure response to the assumed deformation models for the elastic-viscoplastic response is critical. Typically, CCG is studied under load-controlled conditions (e.g., testing is conducted under K-controlled conditions as per ASTM E1457), while plant components can experience displacement-controlled conditions that are dependant on location, transient type, local constraint, and load type. Consideration of the effects of displacement- and mixed load-displacement-controlled conditions on CCG, giving rise to primary and secondary loads, has generated large interest in assessment procedures as well (e.g., R5V4/5 Appendix A3). Application of CDM techniques for evaluating CCG response under these general conditions of interest forms the basis of this study.

4.3 FEM approach and solid mechanics software

4.3.1 Approach and structure of the present CCG study

We employed MOOSE [62] as the foundation for finite element computations, and extended its capabilities for structural-specific applications in BlackBear, a structural finite element application that accounts for finite strain kinematics [86] and features numerous material models (e.g., elasticity, nonlinear rate-independent/-dependent plasticity, and various types of creep models). Recently, more advanced engineering-scale, rate-dependent constitutive models that capture the inelastic straining and internal state evolution in metals (see [68, 103]) have also been leveraged within BlackBear. In addition, CDM models linked to element deletion capabilities can be employed, enabling the removal of finite elements whose

quadrature points have lost their load-carrying capacity (i.e., $\sigma_{ij} \to 0$ at $\omega \approx \omega_f$, where ω is a local damage parameter and ω_f is the saturating value) from the simulation. Contour integrals such as those defining SIFs and the C(t)-integral can also be computed via the domain integral based on finite element model results [94]. The coupling of models within the existing capability is detailed in [98].

This work explores CCG methodologies for metallic materials, aided by finite element tools within the MOOSE finite element framework [79]. From an application perspective, the above points were considered with an out-sight to applying the approach to realistic component geometries. Creep ductility (failure strain) exhaustion criteria are used in combination with a simpler class of power-law creep models to characterize creep failure. Strain-based creep damage is considered at Gaussian quadrature points. Upon finite elements becoming fully damaged (i.e., complete loss of load-carrying capacity), they are effectively removed from the finite element solution. The framework, validated against experimental data on CT specimens [75] in 2D and 3D models, is used here to show creep crack initiation and propagation in problems with multiple geometries such as fracture specimens and more complex components. The response of the creep crack was examined under both load- and displacement-controlled uniaxial loadings, the latter being of high relevance to plant conditions during thermal transients. This approach is demonstrated on a reactor pressure vessel geometry with a postulated crack under creep conditions in Section 4.7.5. These CCG simulations all focuses on applying the methods to austenitic 316H stainless steel, which is an alloy qualified for elevated temperature applications by ASME BPVC Section III, Division 5 [80].

4.4 Computational characterization of CCG

The material models employed in this study encompass nonlinear plasticity, creep, and local damage due to ductility exhaustion. The models were applied to austenitic 316H stainless steel, and specific datasets were employed to calibrate the model parameters. The constitutive models for the numerical characterization of 316H steel are summarized in this section.

4.4.1 Nonlinear rate-independent plasticity

Creep and plasticity were solved together using an iterative strategy that combines individual creep and plasticity return mapping algorithms. Plastic behavior was accounted for via an isotropic rate-independent power-law hardening model. Despite being a simplification, this class of models provides sufficient ability to capture a material's representative tensile response over a temperature range of up to 35–40% of the material's melting temperature. In this model, the stress can be described as follows:

$$\sigma_{\text{eqv}} = \sigma_y + K\varepsilon_{\text{eqv}}^{p,n_p}, \tag{9}$$

where σ_{eqv} is the true equivalent stress, σ_y is the yield stress taken arbitrarily as the proof strength, $\varepsilon_{\text{eqv}}^{p}$ is the effective (or equivalent) plastic strain, and K and n_p are model parameters.

4.4.2 Rate-dependent viscoplasticity (creep)

Viscoplastic strain accumulation is represented using a simple approach for illustration purposes and ease of calibration against the experimental data. In contrast to [75], simplifying assumptions are made here to omit a detailed representation of the internal state evolution, precluding the adoption of models that capture primary creep effects. This section employs the following classical power-law creep model, which

is based on the Norton exponent:

$$\dot{\varepsilon}^{c}_{\text{eqv}} = \dot{\varepsilon}^{c,avg}_{\text{eqv}} = A\sigma^{n_c}_{\text{eqv}}, \tag{10}$$

where $\dot{\varepsilon}^{c}_{\text{eqv}}$ is the equivalent average creep rate, A is the creep coefficient, and n_c is the power-law exponent. Note that the concept of average creep rate comes from the work of Mehmanparast et al. [65], in which it is defined as $\dot{\varepsilon}^{avg} = \frac{\varepsilon^f}{t_r}$, where ε^f is the uniaxial creep ductility and t_r is the time to rupture. Equation (10) is used twice to model, respectively, the contributions of diffusion and dislocation glide/climb creep by:

- Summing the contributions of the various mechanisms of the creep processes in 316H (i.e., created by vacancy diffusion and dislocation climb/glide processes [80]).
- Calibrating the two creep contributions by fitting the behavior as a function of applied stress level.

The overall approach to calibration is similar to that of Hyde et al. [50] and Oh et al. [75]. Uniaxial data are used to calibrate the rate-independent plastic and rate-dependent creep response by using publicly available experimental data. Individual cases are discussed below. The plastic strain tensors are obtained through a flow rule:

$$\varepsilon^{p}_{ij} = L\frac{\partial f}{\partial \sigma_{ij}}, \tag{11}$$

where L represents the multiplier of the plastic process and f is a function representing the yield surface. The constitutive models are integrated implicitly within the FEM framework.

4.4.3 Damage mechanics

Incorporation of the damage model within a finite element framework allows for predicting the local accumulation of deterioration mechanisms that will eventually lead to a loss of load-carrying capacity. Simulation of creep failure by using FEM is based on a ductility-exhaustion damage model; more specifically, we followed the approach proposed by Oh et al. [75]. A limiting local criterion was set to produce crack advancement over a discrete timestep. As the material points (or finite elements) ceased to provide resistance to the external load, the crack was considered to grow due to creep.

The incremental damage within the timestep is defined as the ratio of the increment in equivalent creep strain (ε^c) to the multi-axial creep ductility (ε^*_f). The fracture strain, or creep ductility, strongly depends on the stress triaxiality h:

$$h = \frac{\sigma_1 + \sigma_2 + \sigma_3}{\sigma_{vm}}, \tag{12}$$

where σ_i denotes a principal stress (i.e., $i = 1, 2, 3$) and σ_{vm} refers to the von Mises stress. Note that the sensitivity of multiaxial failure strains as a function of stress state can be captured via numerous empirical and phenomenological models that are functions of principal, effective, and triaxial stresses (see [100]). In the present formulation, the simplest form of such relationships is assumed here [18]:

$$\frac{\varepsilon^*_f}{\varepsilon_f} = \frac{\sinh(\frac{2}{3}\frac{n-0.5}{n+0.5})}{\sinh(2h\frac{n-0.5}{n+0.5})}, \tag{13}$$

where ε_f and ε^*_f are the uniaxial and multi-axial ductility, respectively, and n is the Norton creep law exponent. Values for the uniaxial creep ductility of metallic materials are commonly measured as the failure

strains in creep tests, and are highly sensitive to the material grade, applied stress, heat examined, and prior treatment. The values adopted in this study are directly informed by experimental data.

Damage is then accumulated at each timestep based on the creep strain increment:

$$\Delta\omega = \frac{\Delta\varepsilon^{c}_{\text{eqv}}}{\varepsilon^{*}_{f}}, \tag{14}$$

where $\Delta\omega$ is the increment of the accumulated damage. The current damage can then be computed by simply summing all damage increments:

$$\omega = \sum_{\text{time increments}} \Delta\omega = \sum_{\text{time increments}} \frac{\Delta\varepsilon^{c}_{\text{eqv}}}{\varepsilon^{*}_{f}}. \tag{15}$$

As the local damage, ω, approaches a value of one, the load-carrying capacity of the quadrature point is drastically reduced to capture creep-induced material failure. For ease of computation, the damage variable is updated explicitly based on the damage criterion, and as a result, the stress tensor at that quadrature point is reduced to an infinitesimally small value $\sigma_{ij} \to 0$.

4.5 Calculation of C(t) and C*

As discussed, the study also aims to evaluate the crack growth response by quantifying the domain integral C(t), which is commonly used in assessment procedures and testing. Under steady-state creep conditions, C(t) values capture the energy rate difference with a differential crack growth. As time tends to infinity, C(t) can be correlated as a creep crack growth parameter which defines the stress field at the crack tip.

There are various methodologies for computing C(t) so that it can be applied to estimations of CCG rates under steady loading. While some approaches rely on finite element discretizations and aim at obtaining estimates close to the analytical solution, other methodologies rely on estimates that employ tabulated coefficients and neglect some physics, yet can still be used to provide conservative predictions.

For the purpose of this study, numerical characterization of the material C(t)-$\dot{a}$ was achieved by approximating the C(t) value in two distinct ways. The first was to estimate the C(t)-integral within a domain surrounding the crack. This methodology, proposed in [35], was implemented in BlackBear. The second approach is typically used in experimental evaluations of CCG as applied to standardized geometries. Via the latter approach, the C* was computed per ASTM E1457 [31] for sufficiently long hold times.

4.5.1 Calculation of C* per ASTM E1457

The following relation to approximate C* is employed in the standard ASTM E1457, with application to various geometries and creep behavior:

$$C^{*} = \frac{P\dot{\Delta}^{LLD}}{B_N(W-a)} H^{LLD}\eta^{LLD}, \tag{16}$$

where P is an external load, $\dot{\Delta}^{LLD}$ is the rate of the steady-state portion of the load-line displacement, B_N is the net specimen thickness, $W-a$ denotes an uncracked dimension, and H^{LLD} and η^{LLD} are parameters obtainable from ASTM E1457 based on the specimen's geometry, dimensions, and power-law creep exponents. All the

parameters in Equation (16) are known for a particular specimen, material, and set of boundary conditions. The load-line displacement can be monitored throughout the numerical simulation, and its rate can be obtained by, among other methods, computing the first time derivative of a spline fitted to the numerical output. It is worth noting that other procedures for predicting CCG employ crack type information (orientation, location, and geometry), reference stress solutions, and creep deformation stemming from standardized data (e.g., those used in the Material Properties Council's omega method [29]) (see Section 3.2).

4.5.2 FE-based CCG assessment framework

An alternative approach to the application of formulae provided by standards is the use of finite-element based computational tools. One such computational tool is based on the extension of the J-integral to its rate counterpart. In essence, displacements are substituted by displacement rates, and the strain energy density by the strain energy rate density. When creep is significant, a rate form of the J-integral can describe the stress and strain rate fields at the crack tip. In this creep-dominating case, the C* value can be obtained analogously to the J-integral. The value of Equation (8) may be computed as a domain integral [35], omitting thermal and kinetic effects, as:

$$C(t) = \dot{\tilde{J}}_1 = \int_{V_0} \left(P_{ji} \frac{\partial \dot{u}_i}{\partial x_k} \frac{\partial q_k}{\partial x_j} - \dot{W} \frac{\partial q_k}{\partial x_k} \right) \mathrm{d}s, \tag{17}$$

in which V_0 is the undeformed volume, P_{ji} is the first Piola-Kirchoff stress tensor, and q_k is a vector field that is oriented in the crack normal direction defining the integral over the domain. Since Equation (17) describes the stress field around the crack tip, it can be particularized for various geometries and material model parameters using the reference stress method. The contour integral C(t) can then be expressed for a Norton's creep law (see [7, 50]) as a function of the strain energy rate density. For a particular material at a given temperature, the creep crack growth rate can then be estimated via knowledge of the C* value, i.e. the value of C(t) as $t \to \infty$.

Based on the two adopted approaches for computing the C(t)-integral and the ability to evaluate the localized propagation of the crack, the methodology allows for a consistent validation between the simulation framework and standardized experimental testing. Furthermore, the numerical approach to the determination of C(t) within a contour provides versatility of determination of the parameter in arbitrary crack and component configurations; this will be briefly discussed in Section 4.7.5.

4.6 Finite element methodology for CCG

In a manner similar to other studies reported in the literature (see [75]), we rely on CDM to model crack advancement. The steps followed to computationally characterize CCG can be summarized as follows:

- The geometry is meshed with element sizes that can capture the known spatial evolution of the crack (see Section 4.6.4 for further details).
- Material model parameters for elasticity, plasticity, creep, and damage are selected. These are fitted to the behavior of 316H for various heats and operating temperatures.
- Boundary conditions are applied to the specimen or structural component. Either loads or displacements are applied, then held over time to create a state of stress around an initiated crack.
- The evolution of crack growth is obtained computationally by sampling the damage parameter ω defined in Equation (15) along the path of fracture growth. As this damage parameter is defined

element- or quadrature-point-wise, a step-wise solution is obtained. The CCG rate $\dot{a}$ is calculated by computing the time derivative of a spline built with the point data of $a(t)$ every time a new spatial update occurs.

- The load-line displacement is also outputted and fitted to obtain its rate to compute a C^* estimate, employing relations analogous to those in the ASTM standard [31]. The C^* estimate can only be computed this way for standardized specimen geometries. A computational, domain integral approach is also employed for the same purpose.
- The steady-state solutions for $\dot{a}$ vs. C(t) and $\dot{a}$ vs. SIF, are plotted to perform validation studies and analyze the sensitivity of numerical results to geometry, boundary conditions, and temperature.

The above methodology is employed throughout this section by computing damage locally at each quadrature point. Numerical results and a discussion on the consideration of damage as a non-local parameter (i.e., considering an averaging radius) are found in Section 4.6.1.

4.6.1 Effects of non-local averaging and element deletion on creep rupture

Obtaining mesh-independent solutions involves some sort of regularization approach. Most commonly used regularization methods involve the inclusion of higher order gradients [24] or the use of non-local averaging [83]. The literature shows these methods to be effective at reducing the mesh dependency in the case of brittle and quasi-brittle materials. This section assesses the effects of non-local averaging on ductile creep failure.

Non-local Damage Model A non-local approach involves spatial averaging of the "local" state variable to calculate its "non-local" counterpart. The averaging means that the non-local state variable at a given quadrature point also includes the contribution of neighboring quadrature points, giving the variable its "non-locality" and regularizing it. The non-local damage approach selects the local damage variable as the averaging quantity to calculate the non-local damage, which is then used to calculate the stress.

$$\sigma = (1 - \bar{\omega})\mathbf{C} : \varepsilon \tag{18}$$

The general non-local averaging method involves spatial weight averaging of the local damage variable ω to get the non-local damage variable $\bar{\omega}$ by means of the following integral relation:

$$\bar{\omega}(x) = \frac{\int_V W(x,y)\omega(y)dV(y)}{\int_V W(x,y)dV(y)} \tag{19}$$

The parameter $W(x,y)$ denotes the spatial weight used in the averaging. Ideally, the weight function is a monotonically decreasing non-negative function of the distance $r = |y - x|$, which corresponds to the non-local radius.

Implementation in MOOSE As described in [99], MOOSE implements non-local averaging through the `RadialAverage` UO. The non-local damage can be modeled using the `non-localDamage` class in conjunction with the `RadialAverage` UO. The `RadialAverage` UO provides the framework for non-local integral calculations. The UO takes as inputs the material property (local damage) to be averaged, along with the averaging radius, which provides the spatial distance for performing the averaging. The averaging

radius provides the length limit for selecting the set of quadrature points to consider during the averaging. In the MOOSE implementation, this parameter functions similarly to the material length scale parameter in traditional non-local formulations.

The `non-localDamage` class calls the relevant local damage model and, in combination with the `RadialAverage` UO, returns the non-local averaged damage value. This damage variable is then used by the stress calculator to reduce the stress. The damage supplied by the non-local averaging is based on previous values of the local damage due to the way MOOSE evaluates material properties. The default lag is by a timestep if the `RadialAverage` is executed at the end of each timestep. If the UO is executed on each nonlinear iteration, the lag is reduced to a single nonlinear iteration. Taking into account computation costs and the accuracy of results, all subsequent analyses in this report have non-local damage lagged by one timestep.

Two spatial weights are considered in this study: CONSTANT, with a constant weight of 1 assigned to all quadrature points within the averaging radius; and LINEAR, with the weight decreasing linearly from 1 to 0 with respect to the distance between quadrature points. In preliminary analyses, the simulation yielded better numerical convergence using the linear weighted average than when using the constant weighted average. Hence, the non-local simulations discussed in the subsequent sections of the report all consider linear spatial weights. Figure 15 shows a sample block of code for performing non-local averaging of the damage variable in MOOSE.

```
[Materials]
  [non_ad_local_damage]
    type = MaterialADConverter
    ad_props_in = local_damage
    reg_props_out = local_damage_reg
  []
  [steel_local]
    type = ADSteelCreepDamageOh
    epsilon_f = 0.071
    creep_strain_name = creep_strain
    reduction_factor = 1.0e3
    use_old_damage = true
    creep_law_exponent = 4.9
    reduction_damage_threshold = 0.9
    damage_index_name = local_damage
  []
  [nonlocal_damage]
    type = ADNonlocalDamage
    average_UO = ele_avg
    damage_index_name = nonlocal_damage
    local_damage_model = steel_local
    # use_displaced_mesh = true
  []
  [radial_return_stress]
    type = ADComputeMultipleInelasticStress
    inelastic_models = 'powerlawcrp isoplas'
    damage_model = nonlocal_damage
    max_iterations = 300
    # relative_tolerance = 1e-03
    absolute_tolerance = 1e-07
  []
```

Figure 15: Example input file syntax for using non-local damage in BlackBear.

Finite element model The load is applied through the loading pins inserted into the holes of the sample. This study simulates a simplified 2D model of the CT specimen. The dimensions of the CT specimen are listed in Table 1.

Table 1: CT geometry

W (mm)	B(mm)	a(mm)	P(kN)
50	24.9	26.43	20

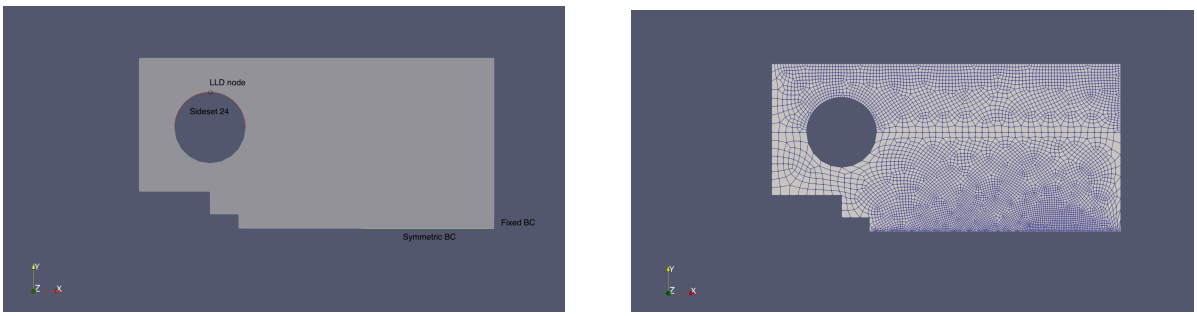

(a) Geometry with key features indicated. **(b)** Finite element mesh.

Figure 16: Boundary conditions and mesh of 2D CT specimen used in study of non-local damage models.

Load control and meshing A 2D simplified version of the CT specimen was modeled in this study. Owing to the symmetry of the specimen, only half the geometry was modeled (see Figure 16), with translation in the y direction fixed on the bottom surface. Nodes on the fixed boundary on the lower right side of the model were constrained against translation in the x direction. The load was applied as pressure on the surface of the upper semicircle. The pressure value was chosen to achieve a total equivalent force of $P = 20\,\text{kN}$. The pressure was increased linearly over the first 0.01 hours, then held constant thereafter.

The mesh of the model was sufficiently refined away from the crack zone in the upper half of the specimen so that further refinement did not affect the simulation results. The final global mesh, shown in Figure 16b, contained 5908 QUAD4 elements. The width of the elements at the crack tip was 200 μm. For finer meshes, refinement was performed locally on the symmetry lines, along the expected crack propagation path. Two such refinements were performed, corresponding to meshes with crack tip element sizes of 100 and 50 μm.

Material parameters The steel elastic modulus was taken as $E = 140000\,\text{MPa}$, with a Poisson's ratio of $\nu = 0.3$. Linear isotropic-hardening-type plasticity governed by the von Mises flow rule was used, with a yield stress of $\sigma_y = 170\,\text{MPa}$. The post-yield stress-strain response of the material (see Figure 17) was used to define the steel behavior in the plastic region.

The creep coefficients and exponents are shown in Table 2. These parameters are stress-dependent and were taken from [84]. The uniaxial ductility parameter ε_f recommended by [75] was taken to be 0.071. The power-law exponent used to calculate the multi-axial ductility was taken to be 4.9, which is the average of the two creep exponents used for local low- and high-stress behavior.

Table 2: Creep parameters

Stress (MPa)	A ($MPa^{-n}h^{-1}$)	n
$\sigma < 175$	6.56×10^{-12}	2.3
$\sigma \geq 175$	1.24×10^{-23}	7.5

The CCG curve obtained with these material parameters for the baseline mesh size and local damage model matches the experimental data in [75] reasonably well (see Figure 18). For the subsequent analyses,

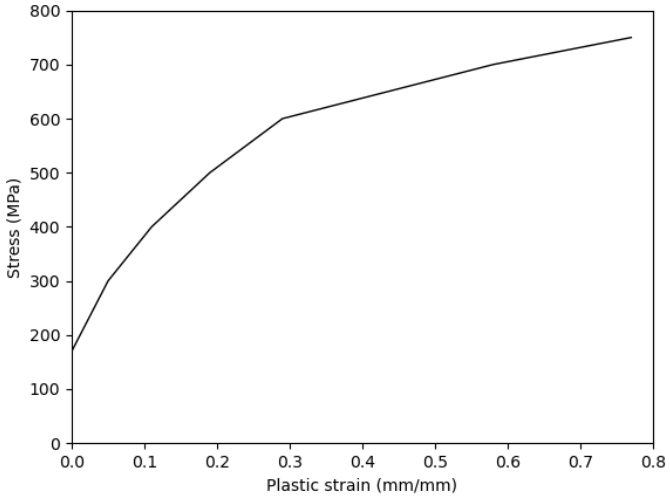

Figure 17: Stress vs. plastic strain model used in non-local damage study.

the above-listed parameters are used.

Creep fracture simulations The fracture test was simulated for the CT geometry using three levels of mesh refinement, as discussed above. For each mesh, two approaches to simulating fracture were adopted, with elements that exceeded the critical damage level (i.e., failed elements) either being deleted or still kept in the simulation but bearing a fraction of the former load. For both approaches, the test was performed with local and non-local damage formulations. And finally, for the non-local formulation, the width of the averaging radius was varied so its effects on the results could be examined. Four different non-local radii (with lengths of 100, 200, 500, and 1000 μm) were considered.

For the purposes of this study, the crack pattern, crack length evolution with time, and C(t)-integral vs. crack growth rate curves were generated, then compared for the different cases. The simulations continued until either the solve failed to converge or the simulation exhausted the walltime prescribed in the batch run (usually due to small timesteps being required). The response quantities and their definitions used in the simulation are described in the following subsection.

Crack length An element is considered to have failed once its damage level exceeds the critical damage value (0.9 in this study). The crack length is calculated by postprocessing the resulting simulation damage variable. A Python script compares the damage value of the element along the crack front (symmetry line) to the critical damage value, and calculates the incremental crack length, based on the farthest fully damaged element at a given time step. The incremental crack length is then added to the initial crack length a_0 to determine the final length of the crack. The script assumes that the crack develops along the symmetry plane, which is true for most of the numerical simulations in this study. In the case of the local damage model, the damage variable used to determine the crack length is the local damage variable; in the case of the non-local damage model, it is the non-local damage variable.

Because incremental crack growth is computed based on the local damage in individual elements, there are abrupt jumps in the computed crack length. To calculate the relationships between the CGR ($\dot{a}$) and C*, a smooth function must be fit to the computed values of a. Splines are used for this purpose, just as they are

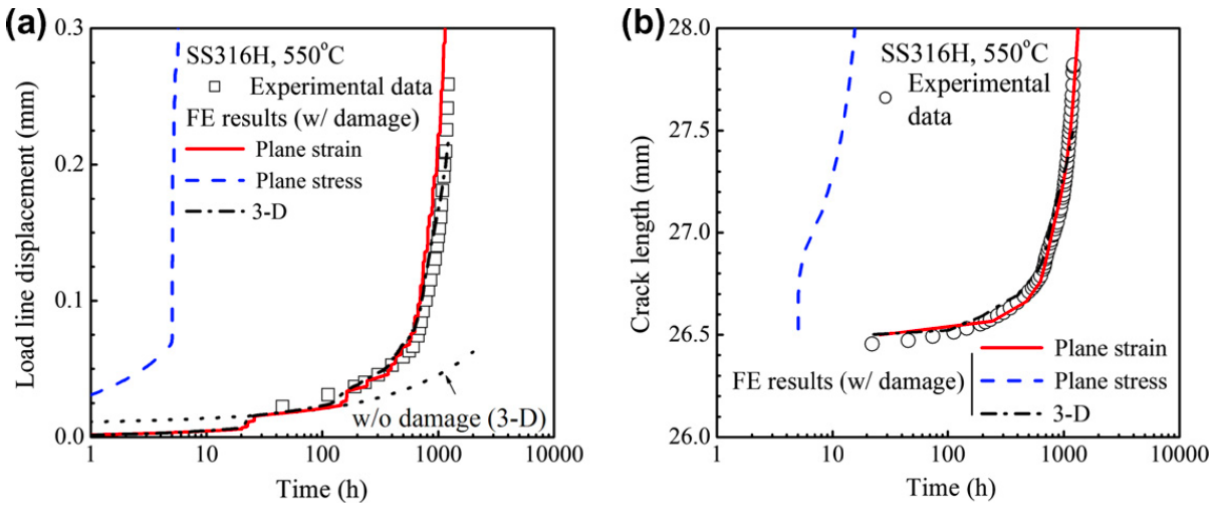

(a) Reference results for (left) load-line displacement and (right) crack length from Oh [75]

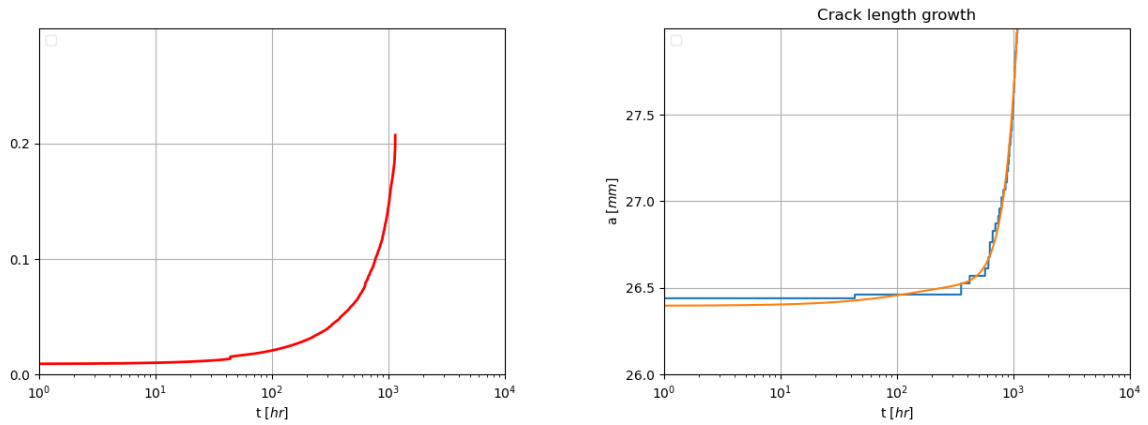

(b) Load-line displacement from current study

(c) Crack length from current study

Figure 18: CCG simulations using baseline mesh and local damage in the current study, compared with Oh's results [75].

used to obtain a smooth representation of the load-line displacement for computing C^* in the ASTM E1457 procedure.

C-integral Both the domain integral (Section 4.5.2) and the load-line-displacement (ASTM E1457) approaches (see Section 4.5.1) were used in this study to assess the effect of non-local damage. Figure 19 compares the C^* yielded by these two approaches. Although there are some discrepancies, the two methods are generally consistent. Because of the consistency between the approaches, and because the domain-integral-based approach is more complex and computationally expensive, the load-line-displacement procedure is used in this study on non-local averaging.

Effect of mesh size and non-local averaging Figure 20 shows the crack growth curve for the three meshes, using both local and non-local averaging. For the local damage model, the crack growth is slower for the coarser mesh, and with refinement the crack length growth rate is faster. There is no considerable difference

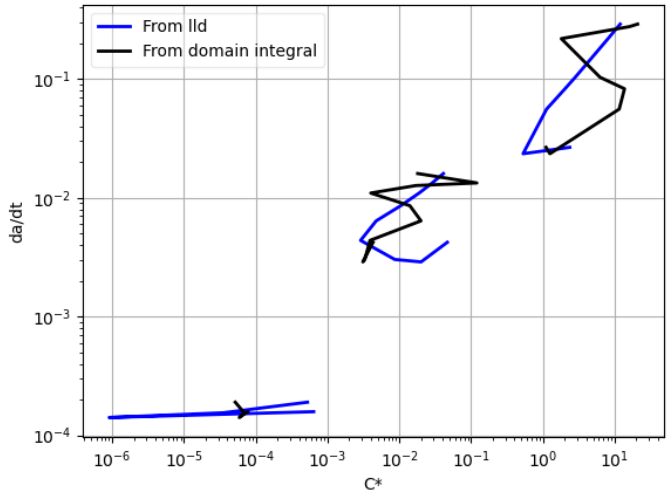

Figure 19: C(t) integral obtained from domain integration compared to that computed using the ASTM E1457 load-line-displacement-based formula.

in the crack growth for the two finer meshes, but mesh refinement has considerable negative impacts on the numerical convergence of the problem. The figure also shows the effect of non-local averaging on CCG. For a small averaging radius of 100 μm, which is less than or equal to the element size, the non-local crack growth pattern closely aligns with the local results. As the averaging radius increases, the crack growth is delayed, as the non-local damage reaches the critical value later than the local damage does. The crack growth curves do not appear to converge with increasing averaging radius, and they shift farther to the right with increasing averaging radius. However, for the two finer meshes, the non-local results are closer to the experimental results (compare Figures 18 and 20c) for the non-local radius of 500 μm, which is within 5–10x the average crack-tip element size. Additionally, except for the finer meshes in Figure 20b, the non-local approach results in longer crack development and better numerical convergence compared to the local formulation.

Figure 21 shows representative local and non-local damage fields for the local and non-local simulations. The highlighted elements have crossed the critical damage threshold and are thus supposed to have been "cracked." Hence, the highlighted elements define the assumed crack pattern in the specimen. The crack front predominantly moves along the symmetry plane, although the damage field increases in the direction normal to the symmetry plane (Figure 21a), as observed in [112]. The crack growth normal to the symmetry plane is influenced by the size of the averaging radius. For a larger radius, the crack initiates farther away from the crack tip and propagates further into the normal direction. A large radius (compared to the average element size) may lead to nonphysical crack propagation in the normal direction (Figure 21b). Moreover, the crack seems to skip elements along the symmetry plane in later stages of the creep if the non-local approach is adopted (Figure 21c).

Figure 22 plots the C-integral (MPa$\sqrt{\text{m}}$/h) vs. crack growth rate (mm/h) for the simulations. For the local simulation runs (closed circles, Figure 22), the crack growth rate is similar for the two finest meshes. The 100 μm mesh converges until a larger load-line displacement and crack length are attained, resulting in higher C^* and $\dot{a}$ values in the plot. The non-local results with a 100 μm radius are reasonably close to the local runs (see Figure 22a). With increasing values of the averaging radius, the crack growth rate is inhibited, resulting in a slightly gentler slope in the plots (see the 100 μm mesh in Figures 22b, 22c, and 22d). For the finest mesh with a 1000 μm radius, not enough results could be obtained following crack growth initiation

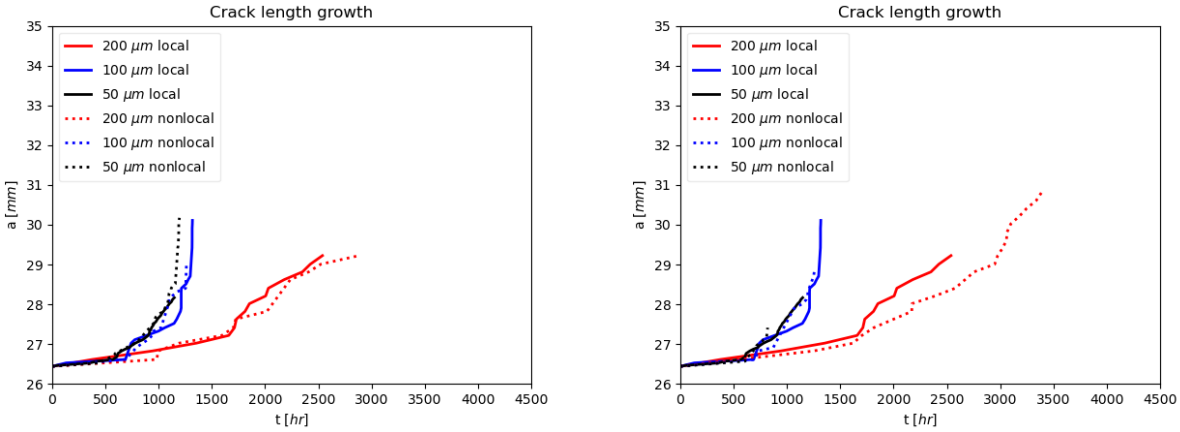

(a) $r = 100\ \mu m$ **(b)** $r = 200\ \mu m$

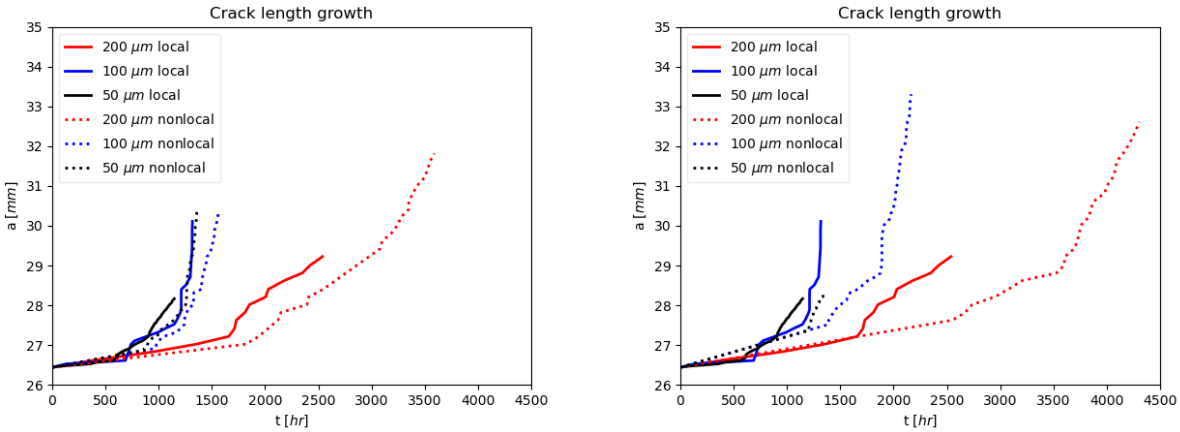

(c) $r = 500\ \mu m$ **(d)** $r = 1000\ \mu m$

Figure 20: Crack growth for varying non-local averaging radii r (with no element deletion). Results are shown for multiple mesh sizes and for both local and non-local damage models.

to allow for fitting a spline to the data; thus, the $\dot{a}$ vs. C^* results for that case are not shown in Figure 22d.

Effect of element deletion Because element deletion is commonly used with local damage models, the effects of element deletion was explored here for non-local damage models. Elements in the mesh were deleted based on the critical damage values. For the non-local models, they were deleted if the local or non-local damage in the element exceeded the critical value of 0.9. This element deletion was achieved using the `CoupledVArThresholdElementSubdomainModifier` UO in MOOSE. This UO moves the deleted element to a dummy block with no active kernels, so that the elements are still present in the mesh, but no longer contribute to the mechanical response. In the case of the non-local runs, the non-local average is performed only on the active block, meaning that the deleted elements are effectively removed from the non-local average.

Figure 24 compares the crack length evolution for the simulations with and without element deletion. For the local damage models (Figure 23a), the crack grows faster after the elements start being deleted. This accelerated creep fracture is consistent with observations made on notched bar tests [112], in which a nodal

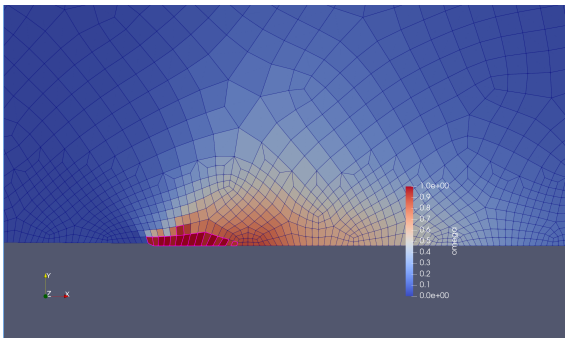

(a) 100 μm mesh (local formulation)

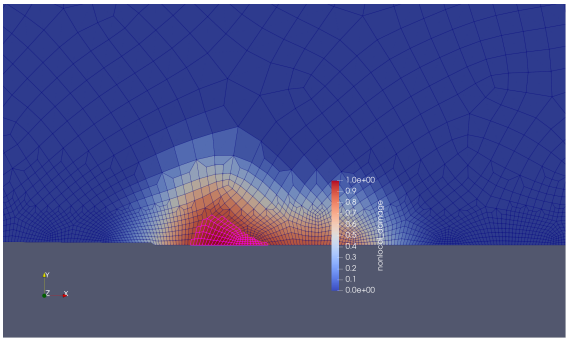

(b) 50 μm mesh ($r = 1000\ \mu m$)

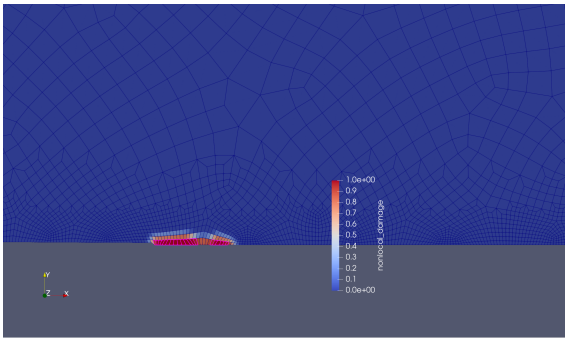

(c) 50 μm mesh ($r = 100\ \mu m$)

Figure 21: Crack patterns (without element deletion) indicated by the local or non-local damage index, as appropriate.

release technique was used to simulate element "deletion." The reason for the accelerated creep fracture is likely the increased stress at the crack tip following removal of the damaged element. Moreover, using an element deletion scheme results in higher values of crack length growth and load-line displacements. When non-local averaging is used with element deletion, the crack growth is delayed initially but then accelerates rapidly after that, as seen in Figures 23b, 23c, 23d, and 23e. The initial slow crack growth rate can be attributed to the fact that once the element is fully damaged and removed from the non-local averaging, the element at the new crack tip takes longer to accumulate a critical level of non-local damage. This occurs because the contribution of the damaged element (with a high non-local damage value) no longer contributes to the non-local damage of the new crack tip. With a larger radius, the high local damage of the crack tip smears over the larger radius, delaying the damage even more. As the crack progresses, the crack growth rate again accelerates, due to higher stresses in the crack tip as a result of stress redistribution. Finer meshes with a larger averaging radius (Figure 23e) fail to converge before a significant crack develops.

Figure 25 plots the different crack patterns observed using the element deletion routine. For a coarser mesh, the crack develops along the symmetry plane but eventually deviates inward at an angle (Figure 25a). This type of behavior is observed for the 200 μm mesh with both the local and non-local formulation with the 100 μm averaging radius. This deviation from the symmetry line occurs in the late stage of creep loading, when the specimen is nearing failure. The crack aligning at an angle to the symmetry plane was also observed by [112] for double-edged notched bars. This behavior is unexpected for isotropic materials under mode I loading, and is likely caused by mesh orientation dependencies. The second pattern is a more realistic crack development along the symmetry line (Figure 25b). This pattern is observed in the finer meshes with local formulation. For non-local damage, a third crack pattern is observed (Figure 25c) in which the damaged elements skip some elements along the symmetry line. The periodicity and length of the skipped elements

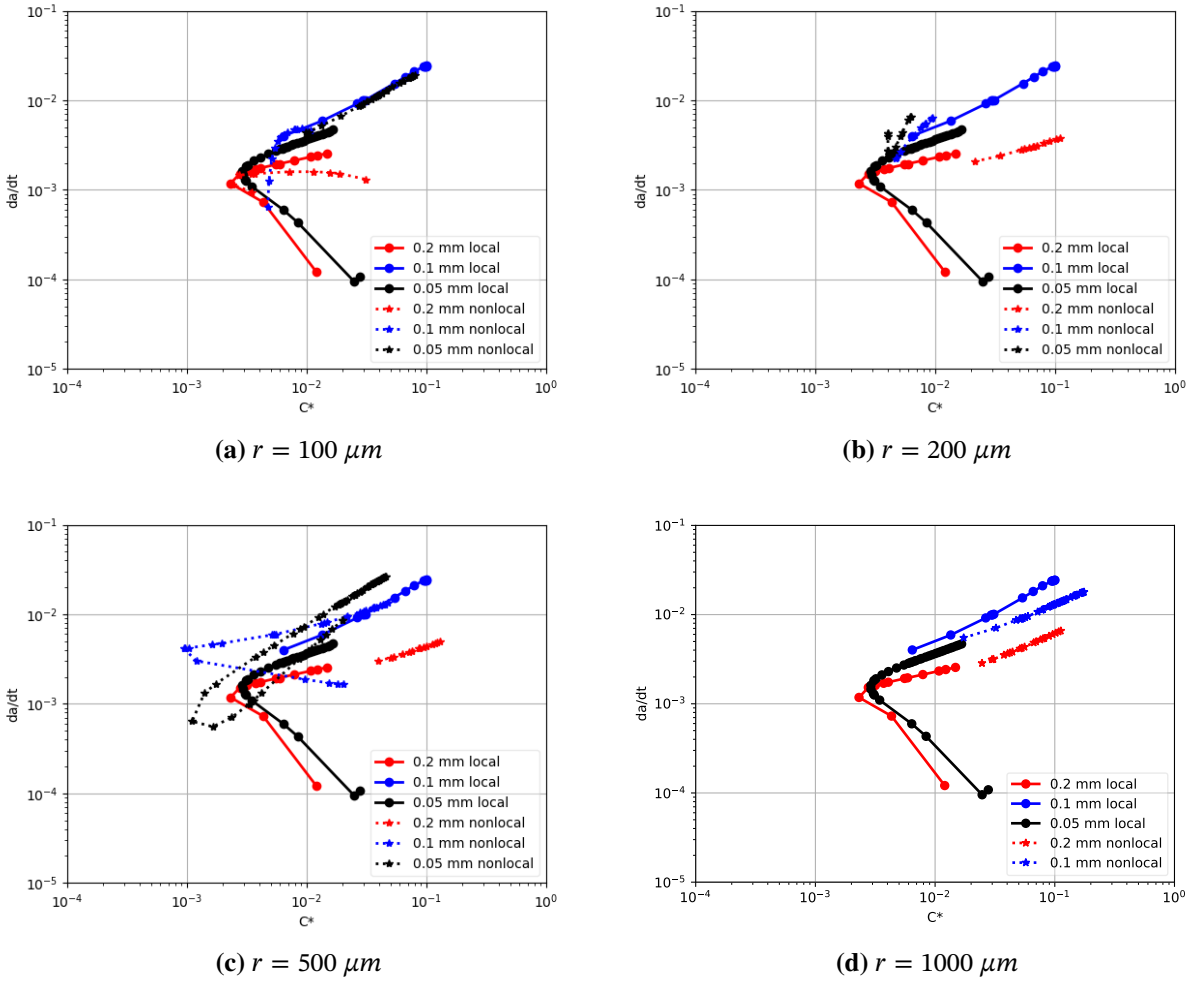

(a) $r = 100\ \mu m$ **(b)** $r = 200\ \mu m$

(c) $r = 500\ \mu m$ **(d)** $r = 1000\ \mu m$

Figure 22: C^* vs. $\dot{a}$ for varying non-local averaging radii r (with no element deletion). Results are shown for multiple mesh sizes and for both local and non-local damage models.

seemingly depend on the radius used for the non-local averaging. Such crack behaviors are not expected for the experimental CT tests. However, the experimental setup consists of a 3D specimen, often with a notch on the sides (reduced net area) to initiate and propagate the crack along the symmetry plane—something difficult to simulate using a simplified 2D model.

Figure 26 plots the C^* (MPa m/h) vs. crack growth rate (mm/h) for those simulations that included element deletion. For the local simulations, the results for the finer two meshes are almost convergent, evident by their similar crack length growth and load-line displacements. The finer two meshes (100 and 200 μm) have very similar C^* vs. $\dot{a}$ plots with non-local averaging with $r = 200\mu$m (Figure 26b). There is also good agreement between the local and non-local results for the 200 μm mesh with $r = 500\mu$m (Figure 26c). In both cases, although the crack initiates at different times, the growth rate is similar (rapid crack growth) once a substantial crack develops.

Summary This study of FEM-based CDM investigated the effects of using non-local damage in creep fracture simulations of a CT specimen. The effect of deleting the damaged elements from the simulation

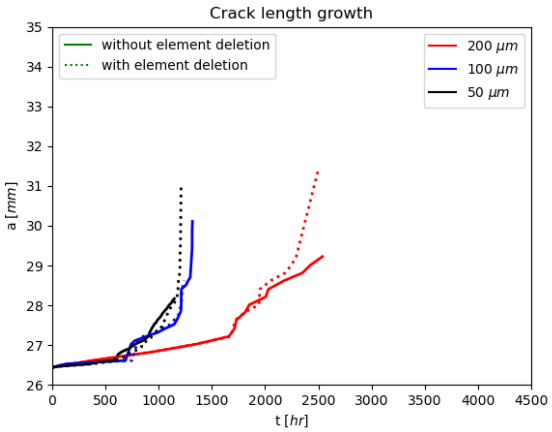

(a) $r = 0\ \mu m\ (local)$

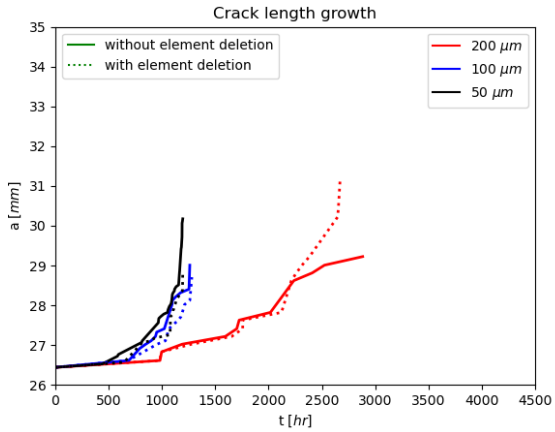

(b) $r = 100\ \mu m$

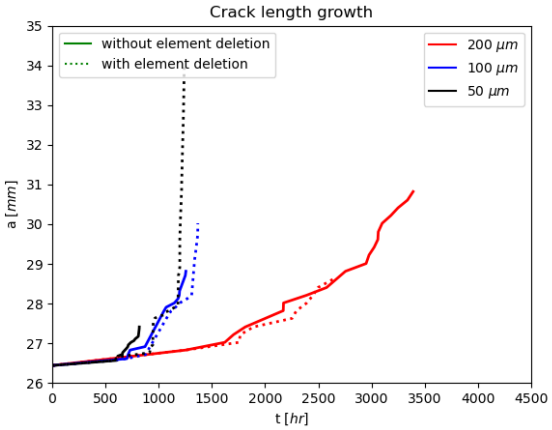

(c) $r = 200\ \mu m$

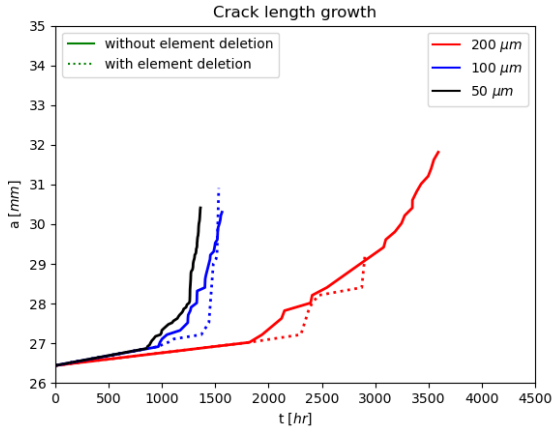

(d) $r = 500\ \mu m$

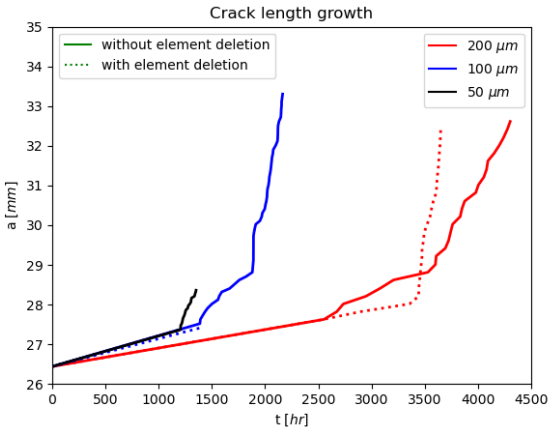

(e) $r = 1000\ \mu m$

Figure 23: Crack length growth (with and without element deletion).

Figure 24: Comparison of crack growth for varying non-local averaging radii r with and with element deletion. Results are shown for multiple mesh sizes, for both local and non-local damage models.

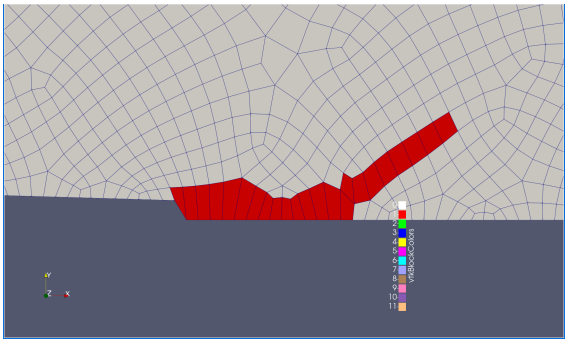

(a) 200 μm mesh (local formulation)

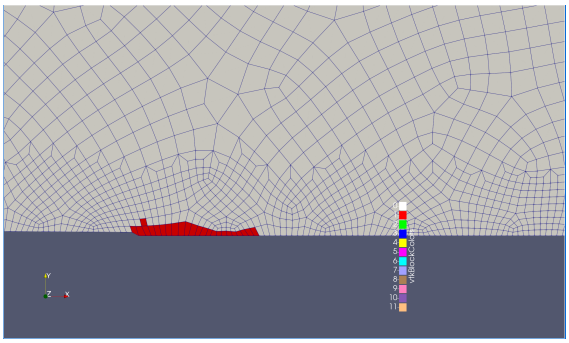

(b) 100 μm mesh (local formulation)

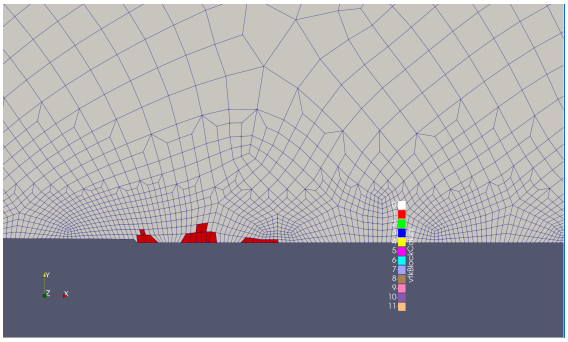

(c) 50 μm mesh ($r = 100\ \mu m$)

Figure 25: Crack patterns (with element deletion), with the elements that have been deleted shown in red.

was also studied. The results of the simulations are summarized below.

- Local damage models were able to reproduce CCG curves that reasonably align with the experimental results when a sufficiently refined mesh is used. Although the results of further mesh refinement seem to indicate convergence to a particular result, the simulations tend to be more prone to numerical issues with more refined meshes.
- Use of non-local damage delays crack initiation and propagation in comparison to local damage models. For this CT specimen, the coarsest mesh was insufficiently refined for producing accurate results. For finer meshes, an averaging radius of 500 μm produced results comparable to the experimental data.
- Use of element deletion with local damage models results in longer cracks and earlier crack growth initiation. Additionally, for coarser meshes, the deletion routine resulted in unexpected deviation of the crack paths from the symmetry line. For finer meshes, the crack front remains on the symmetry line.
- Use of the element deletion routine with non-local damage did significantly affect the crack evolution. The crack propagation was initially very slow but sharply increased after that. For finer meshes, numerical convergence issues become more pronounced due to the increasing averaging radius, as the simulation terminates immediately after crack initiation.

From this study, we have concluded that although non-local damage does show some promise in minimizing mesh size dependencies, it does not show a significant advantage over the local damage model with element deletion for this class of problem. Because of this, the numerical results presented in the

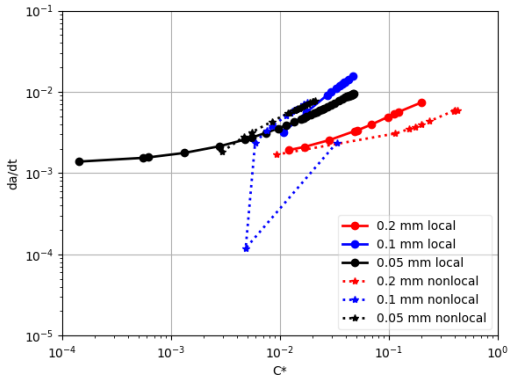

(a) $r = 100\ \mu m$

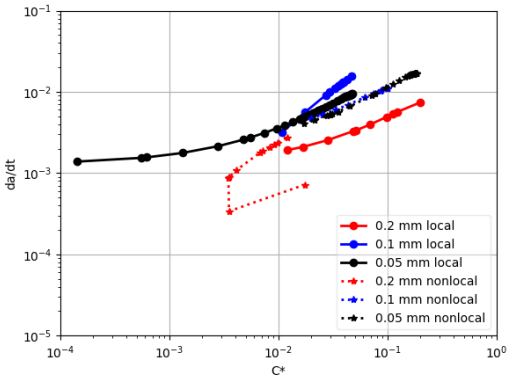

(b) $r = 200\ \mu m$

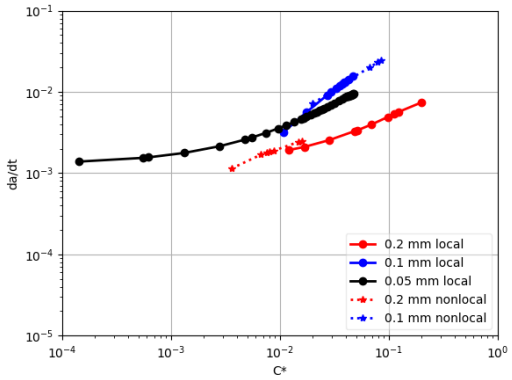

(c) $r = 500\ \mu m$

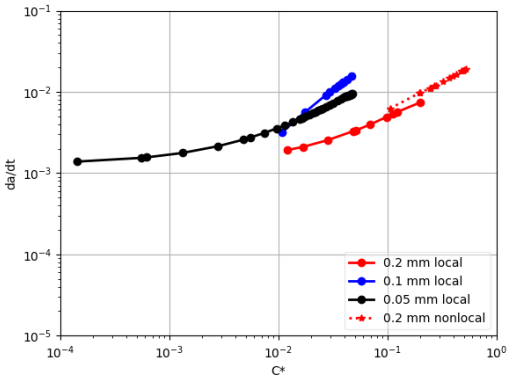

(d) $r = 1000\ \mu m$

Figure 26: C^* vs. $\dot{a}$ for varying non-local averaging radii r (with element deletion). Results are shown for multiple mesh sizes and for both local and non-local damage models.

rest of this section employ local damage and an element deletion technique to remove ill-conditioned finite elements.

4.6.2 Initial verification of a 2D model of a CT specimen (local damage)

Following the methodology proposed above, we modeled a CT specimen in two dimensions under plane strain conditions. The main dimensions of the specimen are shown in Fig. 27. The total force applied at the attachment areas was 20 kN, while the 316H material's behavior was described by elasto-viscoplastic models. Finite strain kinematics was used to describe the mechanical deformation of the specimen. The Young's modulus was assumed to be 140 GPa, and the Poisson's ratio was 0.3. Plasticity was defined by the yield strength (assumed to be 170 MPa) and a constant hardening modulus (selected to be 1800 MPa). Furthermore, the uniaxial ductility value for damage was assumed to be 0.06, and the power-law creep parameters were $1.1{\cdot}10^{-26}$ $\mathrm{MPa}^{-n_c} \times \mathrm{h}^{-1}$ for the coefficient and 8.5 for the exponent.

The external force was applied within the first second of the simulation. That force was then maintained throughout the numerical experiment as the creep and fracture evolved.

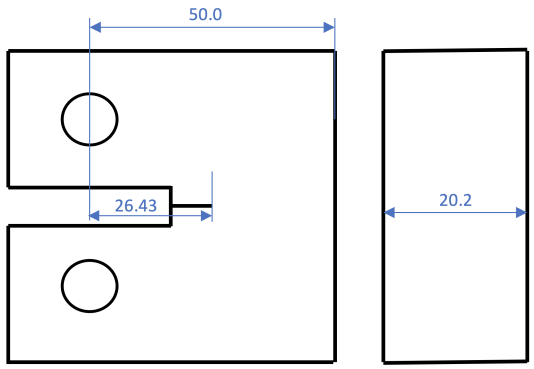

Figure 27: Simplified schema, with main specimen dimensions given in millimeters.

The mesh shown in Figure 28 has an element size of about 0.03 mm along the path where the crack is expected to propagate. Local damage accumulates at the quadrature points of the finite elements. As the local damage variable reaches a value of one, the elements lose load-carrying capacity, effectively causing crack propagation due to creep (see Fig. 29; the elements in red denote material points not contributing to the global mechanical response). The line of elements along the crack path was sampled to obtain the time evolution of the crack length. Similarly, the displacement of the load line was monitored over time. These two quantities were spline-fitted to obtain the time evolution of the crack growth rate and the load-line displacement rate. The latter value was employed to compute C^* (per [31]) with the appropriate parameters. The direct results of the simulation, in comparison to the experimental data, are shown in Figures 30 and 31. The evolution of the load-line displacement and crack growth follow the same temporal trends as the reference data extracted from [75]. By postprocessing the finite element results and relating the time derivative of the crack growth rate in Figure 31 with a C^* value as a function of the load-line displacement rate, the data points in Figure 32 were obtained. These results closely match the closed-form solution provided by Dean et al. [27]. Per the logarithmic relation $\dot{a} = c \cdot {C^*}^d$, Dean et al. obtained the coefficients $c = 0.1054$ and $d = 0.543$, whereas the coefficients from the fitting of the MOOSE results were $c = 0.601$ and $d = 0.543$.

Note that the creep model has not been fitted against the experimental data, which may explain the discrepancies in the numerical results. Still, this example demonstrates the potential to generally leverage multiphysics finite element software for CCG predictions by using a simple, fast-running model.

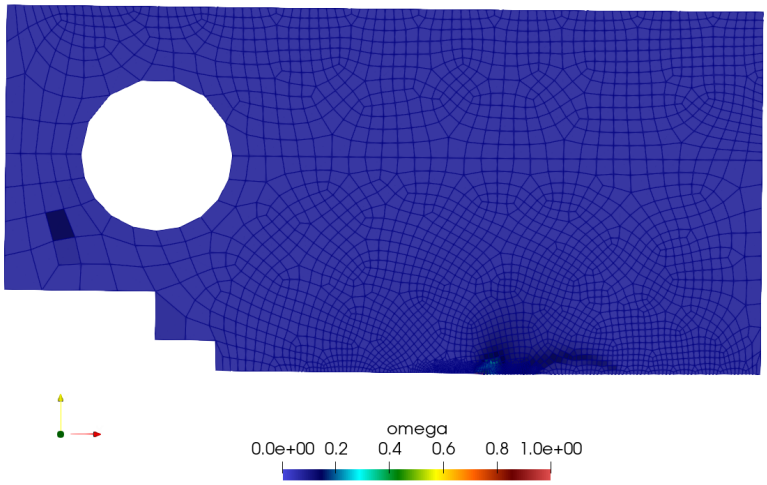

Figure 28: 2D plane strain finite element mesh.

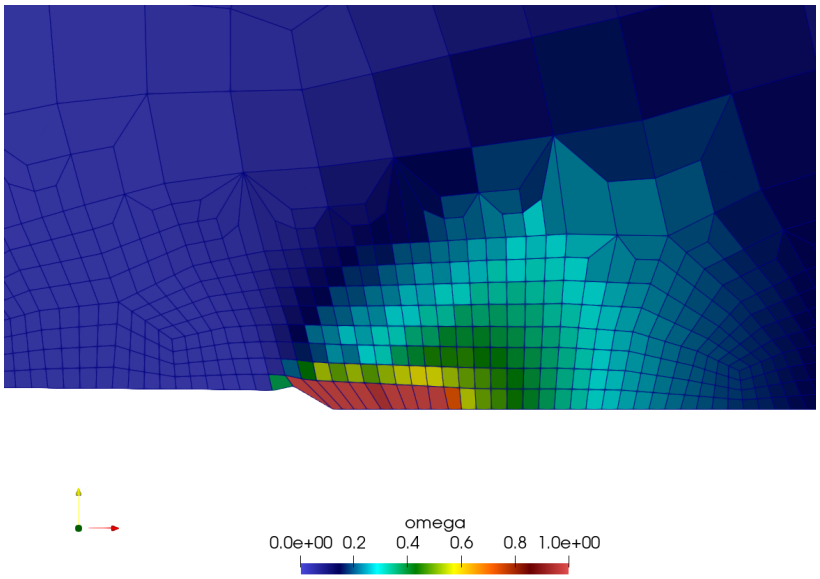

Figure 29: 2D plane strain finite element mesh. Zoomed-in detail of a crack propagation. The damage variable *omega* is colored, and the elements that have lost load-carrying capacity (i.e., a crack has locally propagated) are shown in red.

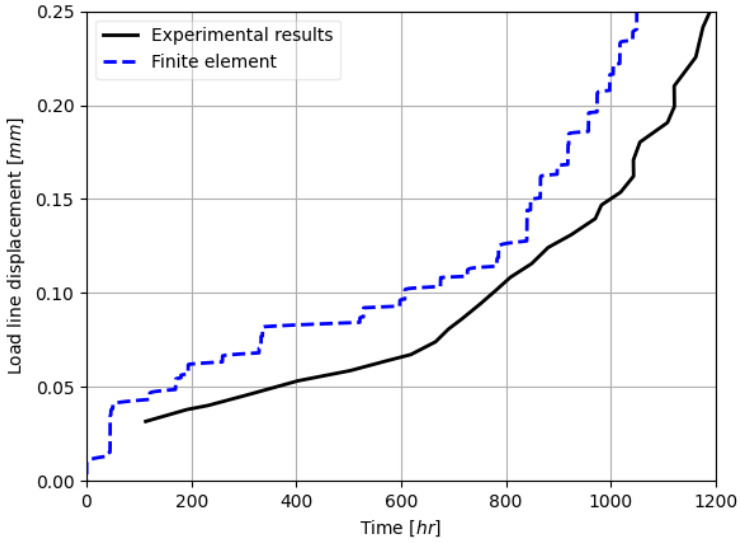

Figure 30: Load-line displacement for the CT specimen.

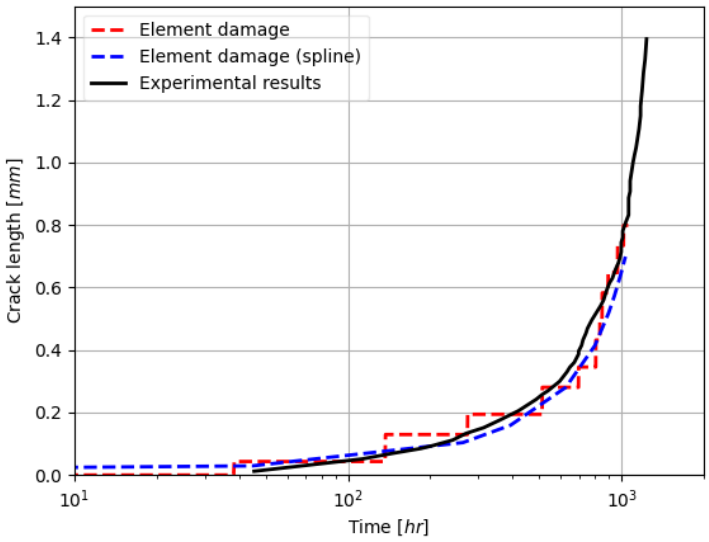

Figure 31: Evolution of crack length over time. The dashed red line shows raw finite element data based on the quadrature point damage level, whereas the dashed blue line results from its spline interpolation.

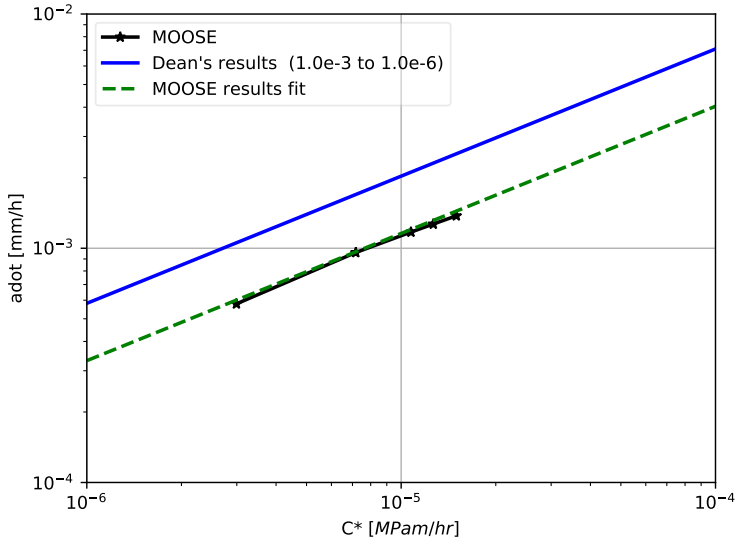

Figure 32: Crack velocity vs. C^* plot, as obtained through postprocessing of load-line displacement and crack growth finite element results. MOOSE's results are compared against the creep characterization provided by Dean et al. [27]. The dashed-green line shows the results from fitting the discrete MOOSE model results.

4.6.3 Validation: CT of ex-service heavily aged 316H at 550°C

Simulation using CDM approaches similar to those presented earlier in Section 4.6 was applied here to study CCG in Alloy 316H. Of particular importance to assessments for high-temperature plants is defect propagation in heavily aged material, as the propensity for defect growth is likely affected by the prior operational period. In this section, we compare the methodology described in Section 4.6 to experimental data [27, 75]. We examine the particular conditions of ex-service heavily aged 316H material (with a history of >50,000 hours at 500–550°C), as tested at 550°C under load-controlled conditions applied to a CT specimen (see [31] for dimensions). The study in this section serves as a validation test scheme for the simulation framework. This application of the framework also conforms to the common approach of testing CCG in CT specimens under an imposed constant load.

The material parameters for the model were selected by producing best-estimate fits of the equivalent inelastic response and uniaxial creep ductility to specific experimental data collected for ex-service 316H at 550°C by Mehmanparast et al. [65, 67] (see Table 3 for details). In this section, we disregard the influence of diffusive creep at 550°C, and use the same set of power-law parameters across the entire stress range.

Model parameters	
Material parameters	Value and units
ε_f	0.125
K	878.7 MPa
n_p	0.3
E	140 MPa
ν	0.3
A_1	$1.11 \cdot 10^{-26}$ MPa$^{-n_c}$ h^{-1}
n_{c1}	8.5

Table 3: Material model parameters for describing the behavior of annealed 316H at 550°C.

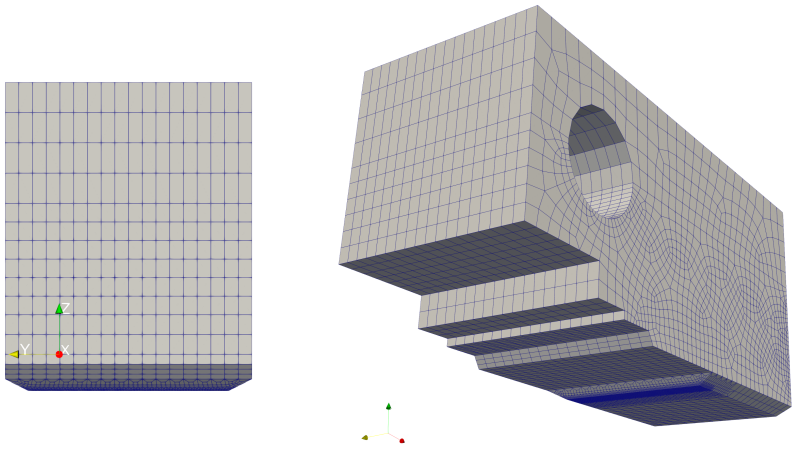

Figure 33: Meshed geometry for CT specimen runs. The CT specimens were simulated using a one-plane symmetry; the load was applied as a distributed mechanical pressure on the attachment upper surface. Nodal displacements at the model's mid-plane were fixed to remove rigid body modes.

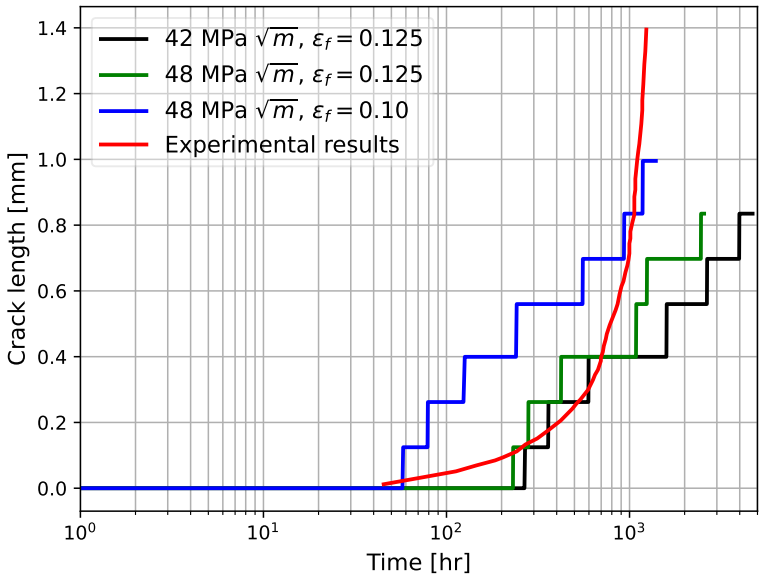

Figure 34: Crack extension results from the numerical experiment: 550°C, ex-service 316H. Experimental results were digitized from [64].

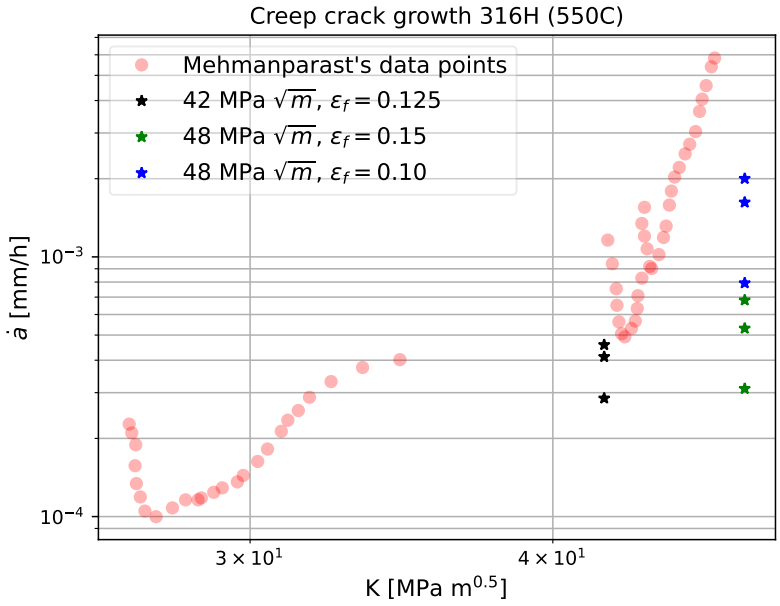

Figure 35: $\dot{a}$ vs. SIF. The numerical results are compared with experimental data points from [63].

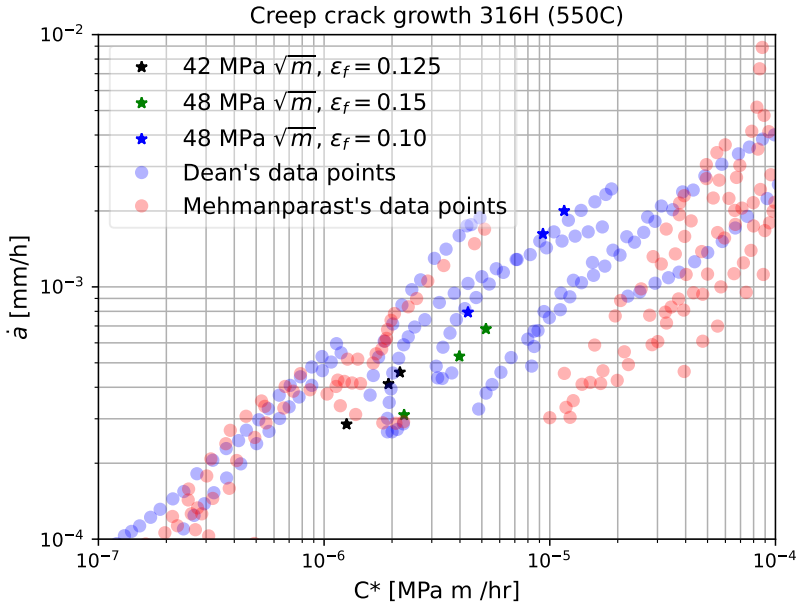

Figure 36: $\dot{a}$ vs. C*. The numerical results are compared with experimental data points from various heats (see [27] and [63]).

The specimen geometry in the numerical simulation was side-grooved. The geometry of this CT specimen is shown in Figure 33. The material model parameters used for the simulations in this subsection are fitted to the material in [27]. These material parameters are described in Table 3. The load that generates the SIF values was computed by means of formulas in [31] and applied at the beginning of the simulation. To explore the sensitivity of the crack growth response, values of 42 and 48 MPa $\sqrt{m}$ were chosen for the SIFs, and 0.1, 0.15, and 0.125 were chosen for the creep ductility, ϵ_f. The crack growth time evolution for these three simulations is plotted in Figure 34. A comparison of growth rates and SIFs against the experimental data is given in Figure 35. Identical SIFs give rise to far-apart growth rates for the same model, even under identical boundary conditions. Numerical results show that the finite element methodology employed here can capture the overall trends of CCG and the correlation of CCG rate to C* values. Indeed, dispersion of the experimental data among the various sets is well within the modeling effort output. This aspect validates the framework for load-controlled conditions of high-temperature CCG in 316H. The next section analyzes the conjugate case where CCG occurs as a result of displacement-controlled conditions.

4.6.4 Mesh sensitivity and numerical stability

In this section, we present mesh size sensitivity analysis results obtained by applying the methodology outlined in Section 4.6. We employed three different CT meshes whose dimensions were taken from [49] and applied an initial SIF of 45 MPa$\sqrt{\text{m}}$. Mesh 1 had 31,710 degrees of freedom and an element size of 0.194 mm along the crack path; mesh 2 had 133,617 degrees of freedom and an element size of 0.065 mm along the crack path; and mesh 3 had 695,007 degrees of freedom and an element size of 0.022 mm. Element size was shown to influence crack propagation in the numerical simulation. One effect of reducing the mesh size is the earlier identification of material points that lost load-carrying capacity. This aspect can be observed in Figure 37, which plots the time required for a crack to reach 0.4 mm. Crack growth length, however, converges with smaller element sizes. Despite the influence of element size, in practice, utilizing a mesh

size that can sample crack growth spatially over the time span being analyzed is sufficient to numerically characterize CCG (see Figure 38 for $C^*vs\dot{a}$ data postprocessed from the three meshes). It can be observed that differences, while existent and on the order of a factor of 2 or 3, are minor when put in perspective, and as expected, they tend to converge with decreasing element size. The uncertainty generated by element size variability is significantly less than what results from propagating the uncertainty in the material parameters. Though, for the sake of brevity, this latter aspect is not explored here, it has been analyzed in the literature on analogous finite-element-based CCG prediction methodologies [75].

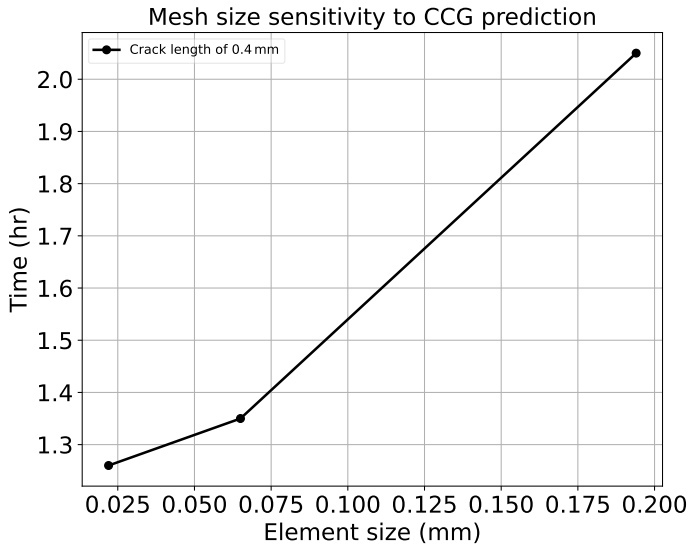

Figure 37: Time required in the CCG simulation for the crack to reach a length of 0.4 mm as a function of mesh element size.

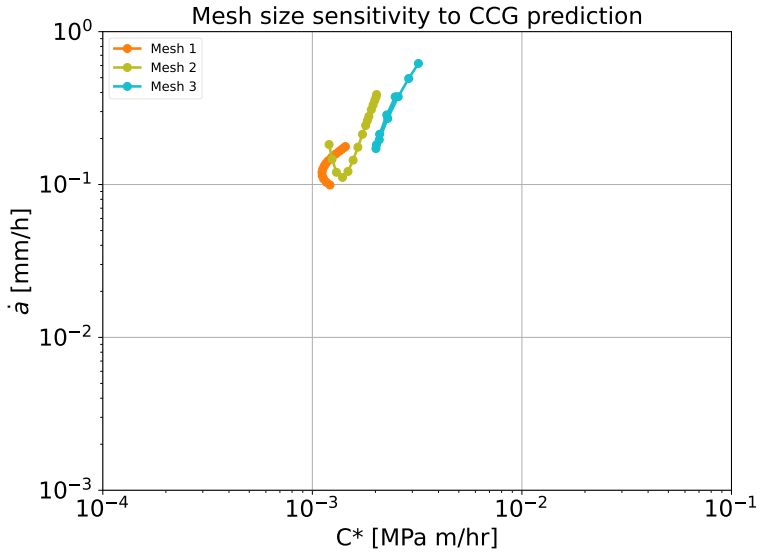

Figure 38: CCG characterization of the material as a function of element size.

The removal of load-carrying capacity (i.e., stress) at the element quadrature points that introduce internal forces to the solids can negatively impact the finite element shapes. As the elements lose strength and their connection with adjacent elements create complex loading/boundary conditions, the Jacobian of the mapping between the reference and the deformed configuration becomes ill conditioned. This phenomenon can readily cause element inversions that result in early termination of the simulation. To avoid this issue, several techniques can be applied to maintain the element shape. For example, one can choose to limit the amount of load-carry capacity lost within the elements. In the present work, before the local damage ω reaches the critical value $\omega_c = 1.0$, the fully damaged elements are moved to a separate simulation domain in which no physics are run. In other words, once elements lose their ability to resist loads, they become inactive, thus preventing element inversions. Use of this (or another similar) technique is requisite for obtaining the CCG results described herein.

4.7 Discussion and application of the CCG methodology

4.7.1 CCG under displacement-controlled conditions in standardized specimens

Creep deformation under displacement-controlled conditions is associated with stress relaxation (see, for example, [107]). Displacement-controlled conditions are particularly important for structural components in which either geometrical constraints or thermal gradients may induce such conditions. Cracks are known to exist, and they grow in regions under stress relaxation conditions. This warrants a better understanding of the creep-crack response under such time-dependent stress fields.

A notable study by Auzoux [9, 11] evaluated the CCG response under displacement-controlled conditions in CT specimens; this phenomenon is termed stress relaxation cracking. We adopted the specimen geometry from Auzoux and simulated the crack growth process for matching conditions from the experimental study. These conditions include an initial loading stage of the sample to a desired K_i-value, following which the displacement at the grip is held constant for an extended duration.

The constitutive models presented in Section 4.4 were recalibrated against the tensile and creep deformation and failure data from Auzoux (see [9]), in which a re-annealed heat of 316H stainless steel was tested at 600°C. The material behavior was again characterized by taking into account the elastic and rate-independent and rate-dependent inelastic response, while localized damage was dictated by ductility exhaustion. Note that under displacement-controlled conditions, relaxation of elastic stress redistributes elastic strains into irreversible creep strains, thus also enabling simulation of the CCG process under stress relaxation. The parameters given in Section 4.4 were fitted to the behavior of annealed 316H at 600°C, and are shown in Table 4, where the creep model contains the contributions from dislocation glide/climb at high stresses (parameter set (A_2, n_{c2})) and diffusive creep processes at low stresses (parameter set (A_1, n_{c1})).

CCG has been reported to best correlate with C^* [23, 49]; however, fewer data are available on the influence of boundary conditions on CCG. We also analyzed the CCG behavior of annealed 316H for displacement-controlled conditions. First, we carried out partial validation of the displacement-controlled setup by comparing the crack growth time evolution to that reported by Auzoux [9] under displacement control. Second, we characterized the same material with load-controlled simulations, from which we related the CCG rate to C(t) values. Finally, we assessed the effectiveness of the SIFs and C^* values for predicting steady-state crack growth in CT specimens under displacement-controlled boundary conditions.

We simulated the response of a CT specimen composed of annealed 316H material under displacement control at 600°C. The initial SIF was 31 MPa$\sqrt{\text{m}}$, just as in [10]. The model and mesh employed are depicted in Figure 33. For the displacement-controlled case, the initial SIF reduces to 23 MPa$\sqrt{\text{m}}$ after 652 hours of

Model parameters	
Material parameters	Value and units
ε_f	0.1
K	512.74 MPa
n_p	0.5
E	135 MPa
ν	0.3
A_1	$1.44 \cdot 10^{-12}$ MPa$^{-n_c}$ h^{-1}
n_{c1}	2.3
A_2	$7.2 \cdot 10^{-25}$ MPa$^{-n_c}$ h^{-1}
n_{c2}	8.6

Table 4: Material model parameters for describing annealed 316H behavior at 600°C

testing. The final opening is 803 μm, and the final crack length is ≈0.5 mm. Figure 39 shows the numerical evolution of the crack at the CT specimen midplane. The steps in the figure refer to the evolution of the progressive loss of load-carrying capacity in the elements along the crack plane. The results show agreement with the amount of crack growth reported in [10] (≈0.5 mm over ≈650 hours). Figure 40 shows the damage parameter and von Mises stress distribution right after applying the boundary condition, and after 300 hours. At the outset, the damage is negligible, whereas it becomes dominant after hundreds of hours. Additionally, the distribution of stresses ahead of the crack relaxes with time, as shown in Figure 40—particularly in the area surrounding the crack front.

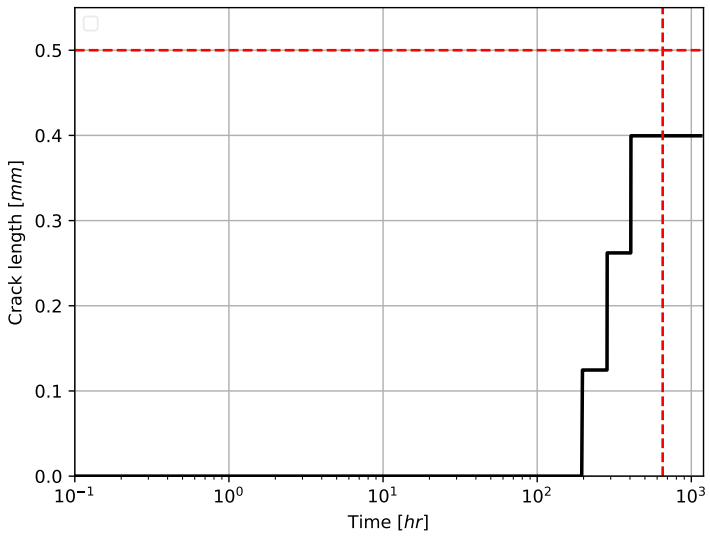

Figure 39: Crack growth over time. The dashed red lines denote the time and crack growth level (i.e., the experimental data point) reported by [10].

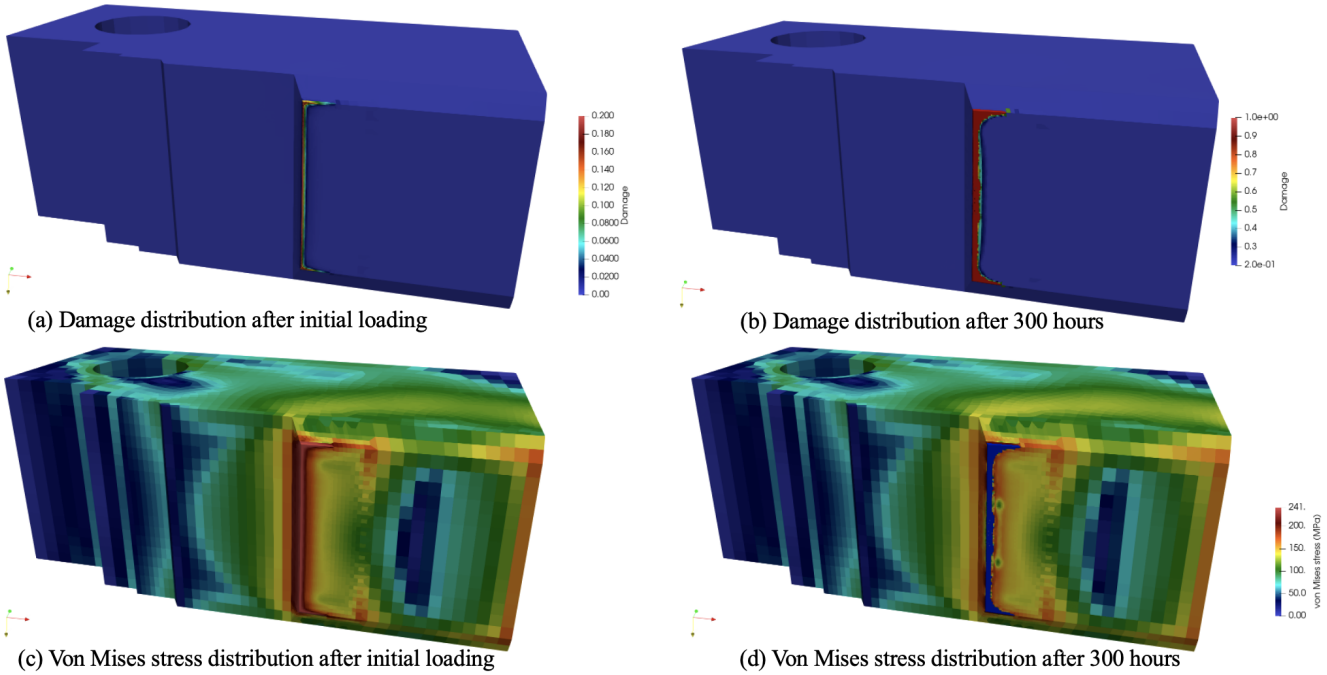

(a) Damage distribution after initial loading

(b) Damage distribution after 300 hours

(c) Von Mises stress distribution after initial loading

(d) Von Mises stress distribution after 300 hours

Figure 40: Evolution of von Mises stress and damage fields in a CT specimen. (a) and (b) show the damage field after initial loading and after 300 hours of simulation, respectively. (c) and (d) show the von Mises stress field after initial loading and after 300 hours of simulation, respectively. After the initial loading, no material points are identified as damaged; however, creep and plastic effects drive stress relaxation over the simulation (see [d]) and the evolution of creep-induced failure (see [b]).

The response of the CT specimen under load control (i.e., constant K_i-value) was evaluated for the same material (i.e., annealed 316H at 600°C). Three loading cases were evaluated with constant K_i = 26, 31, and 38 MPa$\sqrt{\text{m}}$. The same material parameters from Table 4 are used.

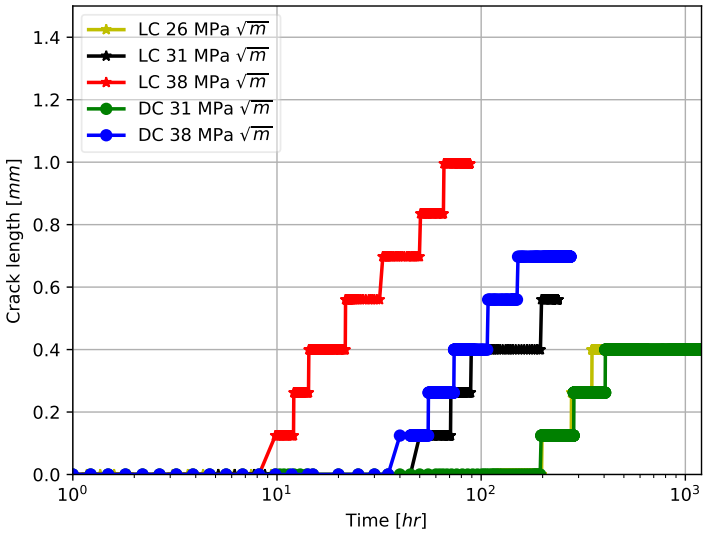

Figure 41: Crack growth over time for six load-controlled and displacement-controlled simulations of annealed 316H at 600°C.

Next, the displacement- and load-controlled simulations of annealed 316H at 600°C were analyzed in two distinct ways. This allowed for different interpretations of the crack growth rates as a function of the crack driving force parameters, K_i and C(t)-integral, to also be evaluated. First, the instantaneous crack growth rates for the two displacement- and three load-controlled conditions are plotted as a function of instantaneous K_i-values. Note the distinct difference between the load- and displacement-controlled cases. As the material relaxes, the values of the reaction force and corresponding SIF decrease over time, thus impacting the stress and strain rate fields on the crack area. For the sake of brevity, these results are not discussed here, but the relaxation of the stress field as the crack progresses under displacement control is seen in Figure 40.

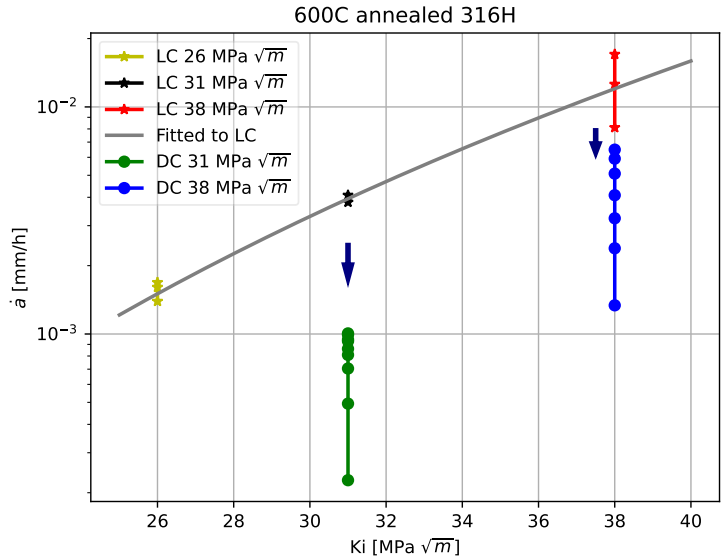

Figure 42: Numerical experiment results of the CCG rate and SIF. The gray line fits the numerical results from load-controlled (LC) numerical experiments for three SIF values. Postprocessing of displacement-controlled (DC) results with 31 MPa$\sqrt{m}$ and 38 MPa$\sqrt{m}$ follow the same trend as the load-controlled results, but the SIF is, as expected, a poor predictor of CCG.

Next, we discuss crack growth rates as a function of the C(t)-integral. Note that predicting the C* value for a displacement-controlled condition typically requires considerations beyond standardized equations and methods for load-controlled cases. For example, a load-line-displacement-based approach to C* is suggested in [31] (see Equation [16]). Application of this method to assess C(t) values for displacement-controlled conditions is not directly viable, as the load-line displacement is virtually constant under such conditions in a CT specimen. Instead, the C(t) values for the displacement-controlled case evaluated were computed via the numerical approach given in Section 4.5.2. The values of C(t) for the load-controlled condition were obtained via the ASTM standard's formula based on load-line displacement (Equation [16]), which is also in general agreement with the numerical estimate of C(t) obtained within the crack domain.

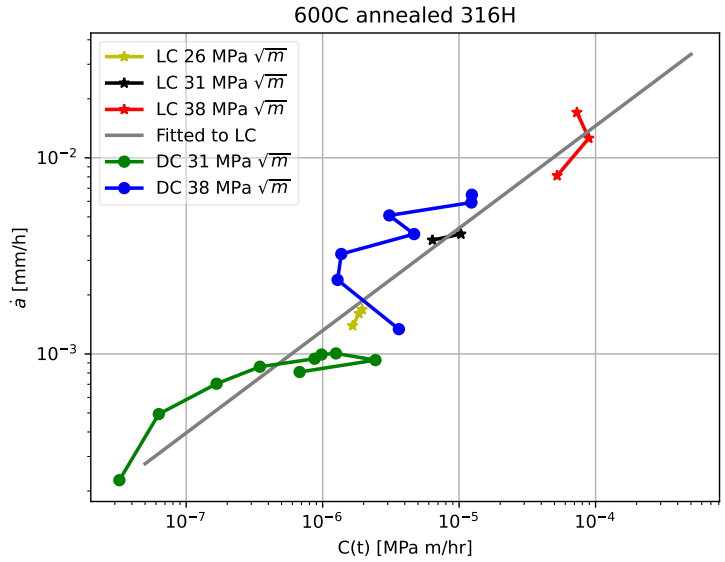

Figure 43: Correlation of numerical experiments between CCG rate and C(t). The gray line fits the numerical results from the load-controlled numerical experiments for three SIF values. Postprocessing of displacement-controlled results with 31 MPa $\sqrt{\text{m}}$ and 38 MPa $\sqrt{\text{m}}$ aligns with the load-controlled predictions.

These results highlight that the modeling framework can predict the evolution of crack growth under time-dependent loading. It was also found that under displacement-controlled conditions, the stress and inelastic strain rate fields ahead of the crack can have significantly smaller values, which drastically retards the equilibrium rate of crack growth. The crack growth results are plotted in Figure 41. This is evident in the reduction of $\dot{a}$ with decreasing K_i-values in Figure 42. Therefore, to limit overly conservative predictions in practice, both assessment methods and models for high-temperature flaw evaluation should account for relaxation of the crack driving force under displacement-controlled conditions. The following subsection probes the crack growth response under conditions that impose different geometric constraints at the crack tip.

From Figure 43, it can be inferred that the correlation between instantaneous crack growth rates and C(t) holds for both load- and displacement-controlled conditions, as estimated for a given set of inelastic characteristics. Therefore, this aspect numerically confirms the general validity of the C(t)-integral as a viable characteristic metric describing the crack tip field under creep conditions in homogeneous materials [32, 71, 87]. Some aspects of these findings are further discussed in Section 4.7.

4.7.2 The effect of geometry and constraint ahead of the crack tip

Shallow cracks in realistic components typically cause low stress triaxiality, potentially leading to increased fracture toughness. In elastic-plastic fracture mechanics, it has been established that the J-integral well describes the crack tip stress field under high constraint conditions. In other words, the actual stress deviates from the stress described by the J-integral, which is considered to be a measure of the constraint level. The concept of crack tip "constraint," which is defined as the degree of triaxiality, was thus developed to quantify this deviation from the stress state predicted by using the J-integral and Hutchinson-Rice-Rosengren (HRR) field alone.

Extensive literature exists on the desire to obtain crack growth data for life assessments of components from CT tests, as well as from other types of experimental specimens (e.g., single-edge-notched bending [SENB] specimens), which provide a high constraint and therefore a conservative metric with respect to the flaw profile in a plant. Adoption of the lower-bound fracture toughness obtained from deeply-cracked SENB specimens is discussed by O'Dowd et al. [77], highlighting the fact that crack growth characteristics from specimen types with a lower constraint (e.g., single-edge-notched tension [SENT]) can also be used to inform an assessment, provided the actual constraint in the applied configuration resembles that of the specimen. In fact, a constraint-based failure assessment diagram established by Ainsworth and O'Dowd [57] is embedded within the R6 failure assessment procedure. Such discussions naturally lead to the need to evaluate the sensitivity of the selected simple class of constitutive deformation and damage models from Section 4.4 in capturing trends of creep crack propagation under different constraints. Recent studies in the literature [21] highlight differences in the stress and inelastic strain rate fields ahead of a creep crack within CT and double-edge-notched tension (DENT) specimens. Here, we evaluate this difference via the numerical framework, and support our findings through comparisons with experimental results. For simplicity, we adopted the material parameters in Section 4.7.1 for annealed 316H steel at 600°C. The influence of the constraint ahead of the crack tip was assessed by conducting additional simulations of CCG in a DENT specimen.

We found that, for lower C^* values, the DENT specimen tended to induce lower triaxiality ahead of the crack. This effect is exacerbated for DENT specimens with low crack length-to-width ratios ($2a/W$). The effects of geometrical and microstructural constraints in various specimen geometries are discussed in [20, 41]. This aspect affects the relationship between C^* and $\dot{a}$. In other words, experimental material characterization will depend on the selection of specimen geometries and initial crack depths. Numerically, these features can also be observed from our simulation results (see Figure 44). Rough trends for C^* vs. $\dot{a}$ are highlighted in blue and red for experimental and numerical results with more and less geometrical constraints, respectively.

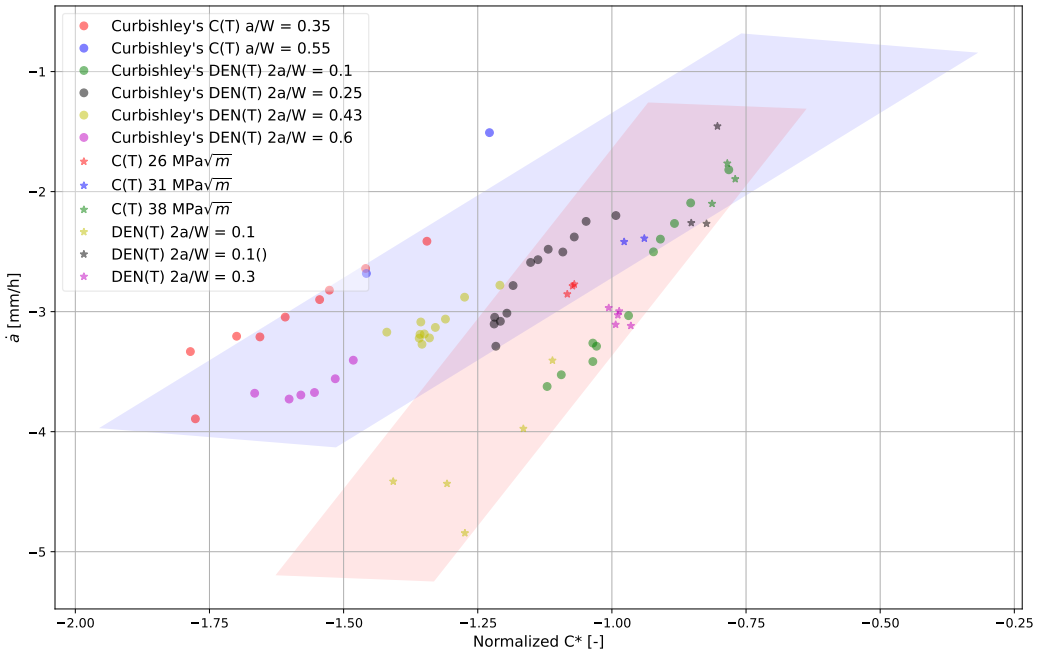

Figure 44: Normalized C^* vs. $\dot{a}$ for experimental data (see [20]), and numerical results obtained from this work. Crack sizes and specimen geometries determine distinct trends in the relationship between crack growth rate and the fracture parameter C^*. The higher the geometric constraint of the crack within the structural component and the applied load, the lower the resulting crack propagation speed. (The abscissa is computed as $\frac{\log C^*}{\log C^*_{ref}}$, in which C^*_{ref} is selected to be the approximate point at which the DENT and CT $C^* - \dot{a}$ trends diverge.)

4.7.3 Evaluation of the crack growth profile due to diverse local specimen features

To explore the observed sensitivity to the triaxiality ahead of the crack tip, as dictated by the overall specimen geometry, we explored an additional case of a CT specimen geometry—one that does not contain the V-shaped grooves on the side. While compliant with the ASTM E1457 standard, such types of specimens typically yield a disc-shaped creep crack profile during prolonged growth, as opposed to the typically uniform profile of the crack along the thickness of the specimen.

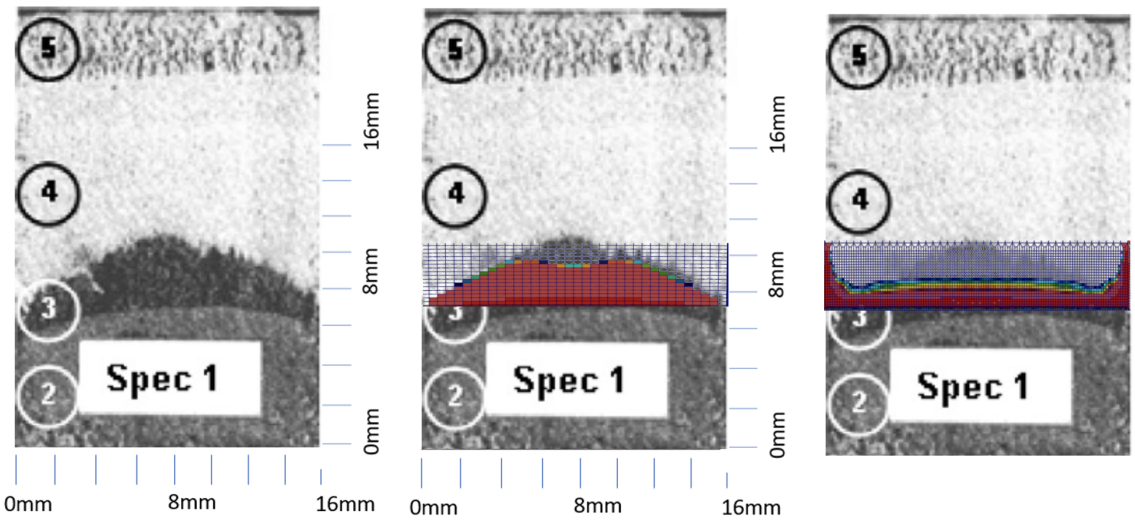

(a) Experimental results from Hyde et al (2010)

(b) Comparison of CCG failure in (a) with numerical results

(c) Comparison of CCG failure in (a) with grooved specimen with ASTM dimensions (numerical results not on scale)

Figure 45: Visualization of CCG damage from the present study, as compared to the experimental results from [50]. Lateral grooves in the specimen impact the advancement of material failure due to creep (see the numerical results of [b] vs. [c]).

A particular case involving CCG in annealed 316 stainless steel at 600°C was proposed by Hyde et al. [49], who reported extensive details on the characterization of both the crack growth rate's dependence on imposed K- and C(t) values. Note that these experimental data were also examined by Hyde et al. [50], who employed a similar CDM approach and found good agreement with data from [49]. In characterizing the crack profile in terms of both shape and absolute crack extension, we acknowledge that CCG response is sensitive to heat-to-heat variation and sample geometries [85].

Here, we simply recalibrated the simple inelastic and failure models to the relevant experimental data reported by Hyde [49], and simulated the crack propagation under load-controlled conditions of K = 38 MPa$\sqrt{\text{m}}$. We utilized two different geometries: one used by [49] without lateral grooving, and one defined in [31]. The predicted results for the crack extension with time are shown in Figure 45 and compared to the experimental data. The resulting crack profile is compared to a scaning electron microscope (SEM) image of the crack profile from Hyde [49]. Note that the absolute growth in time between the model prediction and that recorded experimentally differs very significantly, depending on the numerical model. Differences in crack propagation caused by specimen geometry can exacerbate discrepancies when analyzing results in the $\dot{a}$-C* or $\dot{a}$-K space. This is important, since flaw propagation patterns in realistic components can assume irregular shapes, which also impacts the conservatism in assessment procedures (see [97]). Results shown in the literature (see [49, 91]) typically highlight a CCG data dispersion that can reach a variability of one order of magnitude in terms of the crack propagation rate.

4.7.4 Other geometries analyzed

Here, we briefly describe other geometries employed in the numerical characterization of 316H at 600°C. The $C^* - \dot{a}$ results are shown and discussed in Section 4.7.6.

Elliptical crack in a plate The semi-axes of the elliptical crack were 450 and 2250 mm. The plate was assumed to have dimensions (without accounting for symmetry) of 1000 x 10000 x 10000 mm (see Figure 46). The material properties corresponded to those of annealed 316H steel at 600°C (see Table 4). The boundary conditions ensured double symmetry, both on the crack plane and at a crack angle of $\phi = 90$ degrees. The boundary conditions were applied such that mode I crack opening was excited. These boundary conditions were either "load"-controlled via mechanical pressure or "displacement"-controlled by applying displacements on the boundaries to generate an initial pressure of the same amount as seen in the load-controlled case. When displacement boundary conditions are used, material creep causes reaction forces to decrease over time.

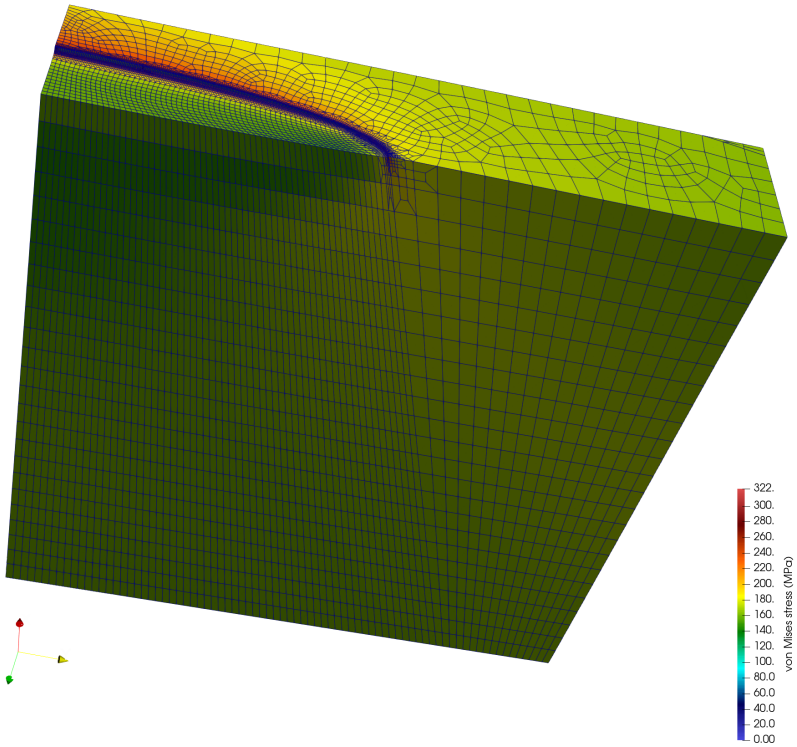

Figure 46: Mesh of a quarter model of an elliptical crack in a plate. Double symmetry is leveraged in this setup.

Double-edge-notched tension An image of the DENT specimen is shown in Figure 47. Its dimensions are as follows: a height (h) of 150 mm and a width (W) of 22.5 mm, with two initial crack length ratios considered (i.e., $\frac{a}{W} = 0.1$ and $\frac{a}{W} = 0.3$). The material properties used in the simulation correspond to those of annealed 316H steel at 600°C (see Table 4).

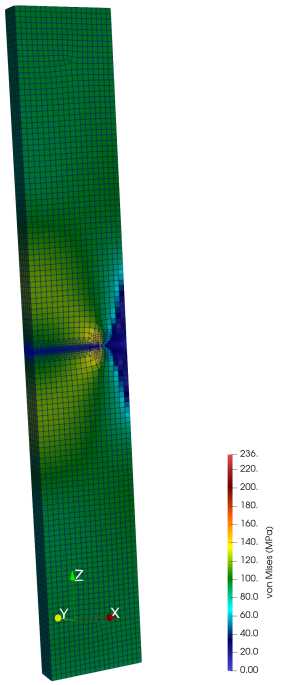

Figure 47: Double-edge-notched tension specimen.

4.7.5 Application to a realistic geometry

As discussed, complex geometries and boundary conditions represent some challenges in the application of assessment methodologies for CCG. A recent code case within ASME BPVC Section XI [4] employs calibrated inelastic deformation models to better capture their interaction with creep deformation leading to failure, thereby informing the stress and strain rate fields ahead of the crack tip. On the other hand, as demonstrated in the preceding sections, the modeling framework employed in this article is able to capture a number of key features of the propagation process, making it viable to probe within more realistic geometries.

In this section, we simulate a 3D representative pressure vessel geometry with an initial crack in a non-trivial position. The same finite-element-based CCG predicting methodology is used in this section for 316H steel at 650°C, following a prior heat-up from room temperature to high temperature and ramped pressurization. In Table 5, the material parameters for the inelastic deformation and failure models are calibrated against representative data for 316H at the temperature of interest.

To simplify the application workflow and reduce computational costs, we employed a submodeling approach to the structural solution. First, the finite element model of the pressure vessel was solved for the entire time span including loading and boundary conditions. As a second step, we created a finite element model (a submodel) of a section of the vessel containing the initial crack. This second model, of much smaller dimensions, is loaded with the displacement field solution obtained from the vessel's model and the appropriate temperature boundary conditions. The boundaries of the submodel are chosen to be sufficiently far from the flaw that they do not affect the stress field perturbed by the flaw. The crack geometry was introduced by utilizing mesh cutting algorithms (see [88] for details). In essence, an uncracked mesh was created, and the location and size of the elliptical crack was provided to the finite element framework, which, before the beginning of the simulation, created the crack geometry in which crack growth is measured and the

Model parameters	
Material parameters	Value and units
ε_f	0.04
K	350.0 MPa
n_p	0.219
E	143.6 MPa
ν	0.3
A_1	$2.956 \cdot 10^{-15}$ MPa$^{-n_c}$ h^{-1}
n_{c1}	8.5
A_2	$9.0 \cdot 10^{-11}$ MPa$^{-n_c}$ h^{-1}
n_{c2}	2.305

Table 5: Assumed material model parameters for describing the behavior of annealed 316H at 650°C.

C(t)-integral values are computed via the domain integral. Solving the structural global problem without the crack (see Figure 48), with symmetry displacement boundary conditions (see Figure 49), and by applying the displacement solution to a local volume containing the crack allows for a reduction in the overall computation time. The boundary conditions for the vessel geometry were prescribed to ensure localization of creep strain on the inner diameter of the vessel shell beneath the nozzle, including the triaxial stress field, which assists the growth of a circumferentially positioned crack in this region. A constant internal pressure of 2 MPa was assumed throughout the simulations. The vessel shell thickness was 100 mm. The crack geometry was defined by an ellipse of semi-axes of 3 and 1.5 cm. The location of the (meshed) submodel in the global vessel model is shown in Figure 48. The crack is primarily oriented circumferentially on the inner side of the vessel (see the finely meshed area in Figure 50).

The evolution of the crack's growth is plotted in Figure 51. Steady-state values for crack growth under these conditions were numerically determined to be approximately $\dot{a} = 3.0 \cdot 10^{-4}$ and $C^* = 1.5 \cdot 10^{-5}$ MPa m/hour. These results are influenced by the level of constraint of the crack and the properties of the material at 650°C. We can infer a number of aspects regarding the FEM approach and its numerical results for the arbitrary crack in the vessel:

- This approach can simulate crack growth in a realistic component under conditions in which an initial stress state eventually relaxes to a steady state.
- The application of analytical methods to assessing CCG can be compared to the FEM-based modeling predictions to understand the level of conservatism of simplified procedures. Of course, this result will be sensitive to the constitutive models employed as well (see Section 4.7 for further discussion on this).
- The basic approach utilized offers versatility in adopting material properties recorded from engineering-scale testing for validating a model framework and extending it to predictions at the component scale of an as-built plan.

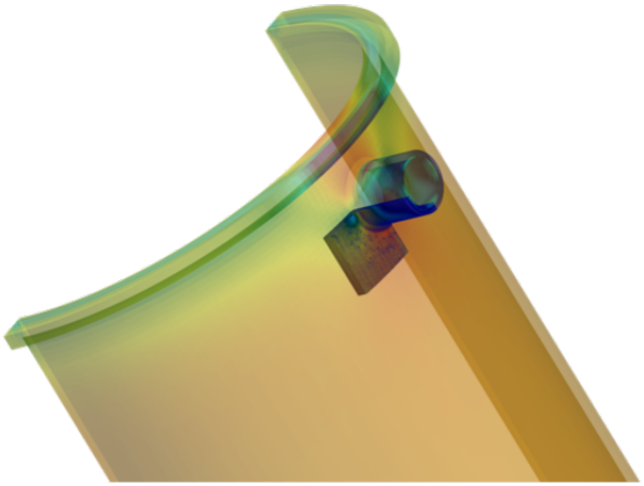

Figure 48: von Mises stress distribution in the pressure vessel model.

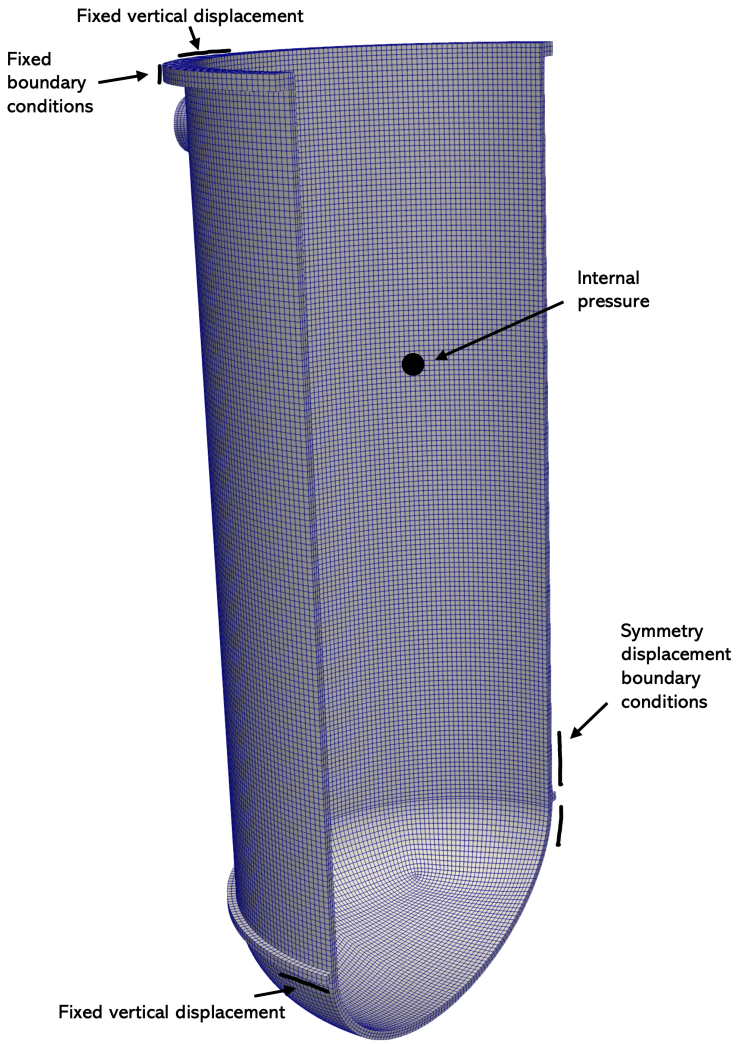

Figure 49: Boundary conditions in the global vessel FEM.

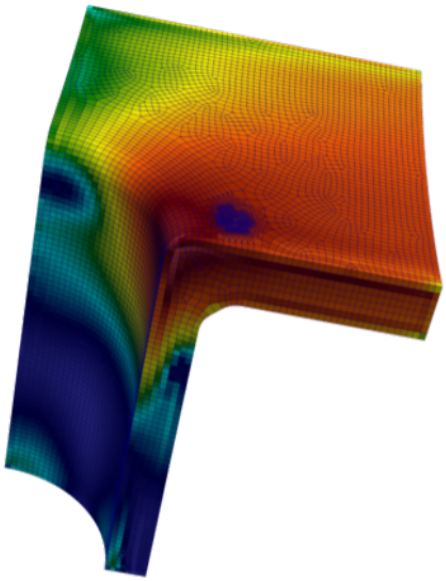

Figure 50: Details of the mesh model around the crack geometry.

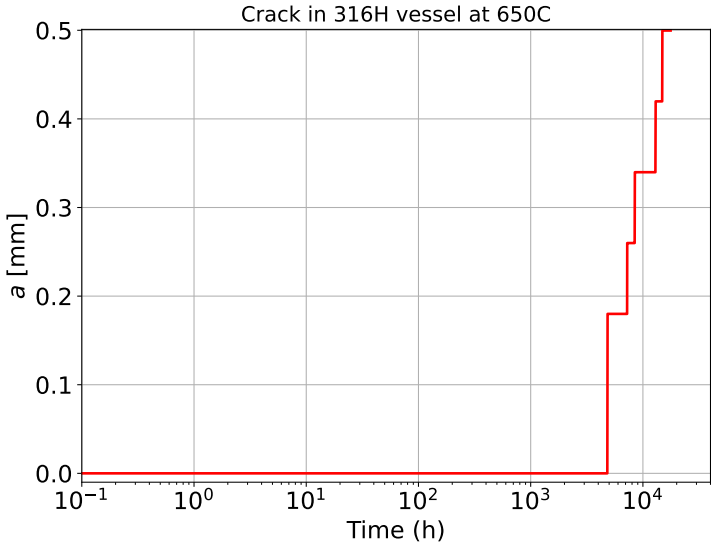

Figure 51: Radial growth of the crack in the vessel.

4.7.6 Summary of the numerical CCG characterization

In this section, we explored the numerical CCG characterization effort based on CDM. We took the numerical output of the finite element simulations and related the speed at which crack propagates due to creep with corresponding values of C^* computed via ASTM E1457 or with MOOSE's domain integral capabilities. The logarithmic relation between $\dot{a}$ and C^* holds overall, despite those important aspects that introduce uncertainty in the characterization of the material, including boundary conditions and constraints

ahead of the crack tip, which can be considered responsible for the discrepancies between 316H experimental data [49] and our numerical results in Figure 52.

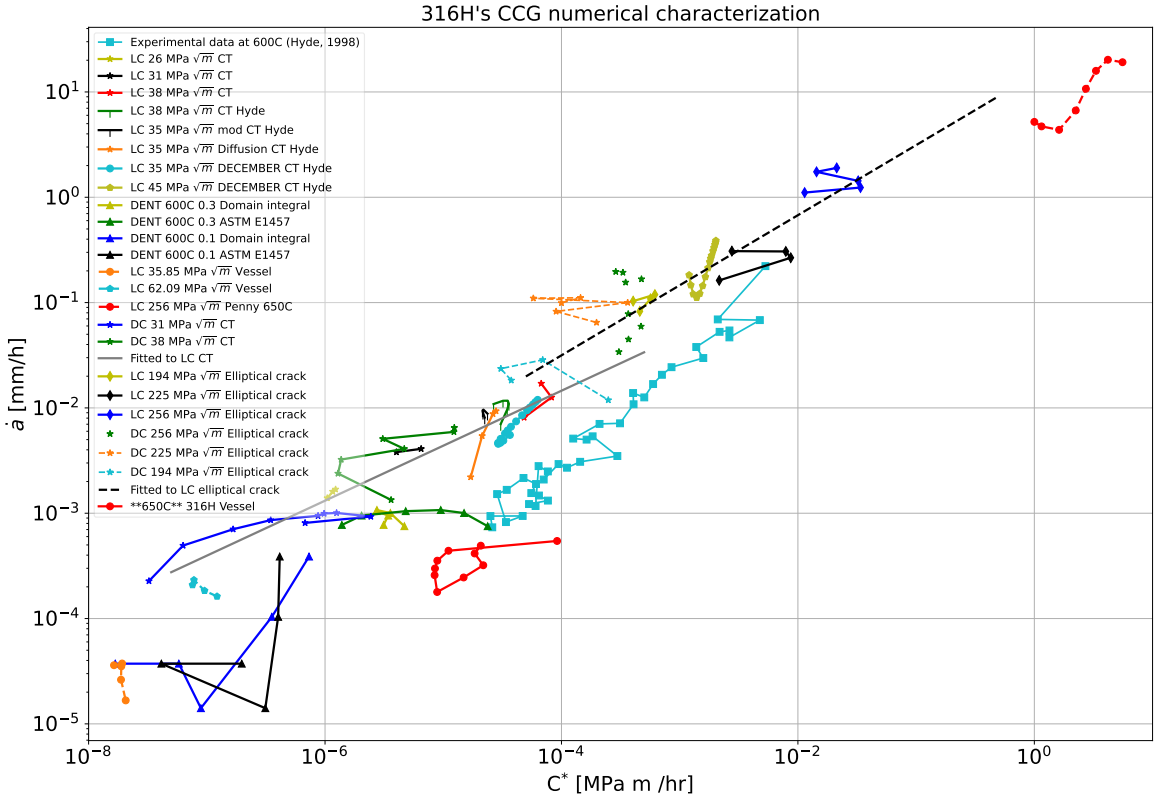

Figure 52: $\dot{a}$ vs. C*. Experimental results from [49] are compared with the results for CT, DENT, an elliptical crack in a plate, and an elliptical crack in a pressure vessel. For CT specimens, the non-standard geometry used by Hyde is marked "Hyde." Two different boundary conditions were used: load-controlled and displacement-controlled. The domain integral approach was used to compute C*, except when "ASTM E1457" is spelled out in the legend; in such cases, the load-line displacement was monitored during the simulation to compute C* according to the approximated formula. SIFs are given in the legend in MPa$\sqrt{m}$ units. The vessel results at a higher temperature (650°C) are also shown on the plot.

4.7.7 The effect of constitutive response, including relaxation, rate-dependence of inelastic straining and multi-axial creep ductility

The relatively simple engineering-scale approach used here has known shortcomings. The response of stainless steel above 550°C becomes markedly more rate-dependent than at lower temperatures, particularly under strain-controlled tensile loading. The models employed herein do not account for the detailed evolution of the material state within the creep and plastic process zones ahead of the crack. More advanced material models, including rate-dependency or based on mesoscale modeling, can be utilized in the MOOSE finite element framework to predict CCG [95]. Capturing these advanced material features is key to the following

effects:

- Evolution of the material's local state. For example, hardening of the material ahead of the crack tip would modify the characteristic creep rates in 316H, whose creep response is sensitive to pre-straining [66, 67, 81].
- Application of more predictive material models at the component scale will also better capture long-range stress fields that can also affect the stress and strain-rate fields ahead of the crack.
- Typically, power-law creep models calibrated to load-controlled creep are deficient in accurately capturing creep strain accumulation during stress relaxation [107]. Application of more advanced inelastic models would improve the capability to describe both stress- and strain-controlled creep response.
- The impact of loading and operation histories, as well as the interaction of fatigue and creep, can be better described by more advanced material models.

4.8 Conclusions on FEM-based CDM predictions of CCG

The methodology described and analyzed in this section—or a similar one founded on more advanced material models—could potentially be integrated into the procedure given in ASME BPVC Section XI [4]. This possibility makes it important to assess whether existing analytical approaches to CCG predictions are overly conservative. Consideration of the elastic-viscoplastic rate-dependent response of materials within these assessment procedures can help reduce the excessive conservatism of elastic approaches. Integration of a CDM-based finite element methodology into the assessment procedures can also aid in the design of specific workflows for other operating conditions, including dynamic response and non-proportional loading, which will enable a reduction in the extent of the testing and characterization efforts.

This work presented numerical results from applying a CDM-based methodology, including creep and plasticity data fitted to the behavior of stainless-steel materials at various temperatures. The procedure was validated against published data and uses the domain integral approach in computing C^*, thus allowing for a more accurate characterization of CCG. Several specimen geometries, boundary conditions, and crack tip constraint conditions were modeled and discussed within a CCG-prediction methodology. The numerical results show that the integration of advanced material models within a finite element methodology can help increase the accuracy in predicting fracture and fracture growth at high temperatures. The conclusions drawn here open the door for using more advanced material models in practical assessments of crack growth in structural components routinely used by industry.

REFERENCES

[1] Ainsworth, R., Dean, D., and Budden, P. (2011). Creep crack growth under complex loading. In *Creep-Fatigue Interactions: Test Methods and Models*. ASTM International.

[2] Ainsworth, R. A., Ruggles, M. B., and Takahashi, Y. (1990). Flaw assessment guide for high-temperature reactor components subject to creep-fatigue loading. Technical report, Oak Ridge National Laboratory.

[3] Ainsworth, R. A., Ruggles, M. B., and Takahashi, Y. (1992). Flaw Assessment Procedure for High-Temperature Reactor Components. *Journal of Pressure Vessel Technology*, 114(2):166–170.

[4] American Society of Mechanical Engineers (2021). *ASME Boiler and Pressure Vessel Code*. American Society of Mechanical Engineers.

[5] Anderson, T. L. and Osage, D. A. (2000). API 579: a comprehensive fitness-for-service guide. *International Journal of Pressure Vessels and Piping*, 77(14-15):953–963.

[6] Argonne National Laboratory (2023). NEML code repository. https://github.com/Argonne-National-Laboratory/neml.

[7] ASTM (2001). Standard test methods for measurement of creep crack growth rates in metals. *Annual Book of ASTM Standards; ASTM: Philadelphia, PA, USA*, 3.

[8] ASTMSTP905, S. V. (1986). Creep crack growth under non-steady-state conditions. In *Fracture mechanics: Seventeenth Volume: Seventeenth National Symposium on Fracture Mechanics on Fracture Mechanics sponsored ASTM Committee E-24 on Fracture Testing, Albany, New York, 7-9 August 1984*, page 185. ASTM International.

[9] Auzoux, Q. (2004). Fissuration en relaxation des aciers inoxydables austénitiques-influence de l'écrouissage sur l'endommagement intergranulaire. *École Nationale Supérieure des Mines de Paris, Doctoral dissertation*.

[10] Auzoux, Q., Allais, L., Caës, C., Monnet, I., Gourgues, A.-F., and Pineau, A. (2010a). Effect of pre-strain on creep of three AISI 316 austenitic stainless steels in relation to reheat cracking of weld-affected zones. *Journal of Nuclear Materials*, 400(2):127–137.

[11] Auzoux, Q., Allais, L., Caës, C., Monnet, I., Gourgues, A. F., and Pineau, A. (2010b). Effect of pre-strain on creep of three AISI 316 austenitic stainless steels in relation to reheat cracking of weld-affected zones. *Journal of Nuclear Materials*, 400(2):127–137.

[12] Baker, A. J., O'Donnell, M. P., and Dean, D. W. (2003). Use of the R5 Volume 4/5 procedures to assess creep–fatigue crack growth in a 316L (N) cracked plate at 650 °C. *International Journal of Pressure Vessels and Piping*, 80(7-8):481–488.

[13] Bassani, J. L. and Hawk, D. E. (1990). Influence of damage on crack-tip fields under small-scale-creep conditions. In Knauss, W. G. and Rosakis, A. J., editors, *Non-Linear Fracture: Recent Advances*, pages 157–172. Springer Netherlands, Dordrecht.

[14] Begley, J. A. and Landes, J. D. (1976). *A Fracture Mechanics Approach to Creep Crack Growth*. ASTM International.

[15] Brust, F. W., Wilkowski, G. M., Krishnaswamy, P., and Wichman, K. (2010). Creep and creep-fatigue crack growth at structural discontinuities and welds. Technical report, ASME Standards Technology, LLC.

[16] Buchalet, C. and Bamford, W. (1976). Stress intensity factor solutions for continuous surface flaws in reactor pressure vessels. In Rice, J. and Paris, P., editors, *Mechanics of crack growth, ASTM STP 590*, pages 385–402. American Society for Testing and Materials.

[17] Chang, T. C., Popelar, C. H., and Staab, G. H. (1987). Creep crack growth in an elastic-creeping material Part II: mode I. *International Journal of Fracture*, 33(1):31–45.

[18] Cocks, A. C. F. and Ashby, M. F. (1980). Intergranular fracture during power-law creep under multiaxial stresses. *Metal Science*, 14(8-9):395–402.

[19] Cocks, A. C. F. and Ashby, M. F. (1982). On creep fracture by void growth. *Progress in Materials Science*, 27(3-4):189–244.

[20] Curbishley, I., Pilkington, R., and Lloyd, G. J. (1986). Macroscopic creep crack growth in type 316 stainless steel.: III. Application of linear and nonlinear elastic fracture mechanics. *Engineering Fracture Mechanics*, 23(2):401–422.

[21] Dai, Y., Liu, Y., and Chen, H. (2019). Numerical investigations on the effects of T-stress in mode I creep crack. *International Journal of Computational Methods*, 18:8.

[22] Davies, C. M., Dean, D. W., Nikbin, K. M., and O'Dowd, N. P. (2007). Interpretation of creep crack initiation and growth data for weldments. *Engineering Fracture Mechanics*, 74(6):882–897.

[23] Davies, C. M., Mueller, F., Nikbin, K. M., O'Dowd, N. P., and Webster, G. A. (2006). *Analysis of creep crack initiation and growth in different geometries for 316H and carbon manganese steels*. ASTM International.

[24] De Borst, R., Sluys, L. J., Muhlhaus, H.-B., and Pamin, J. (1993). Fundamental issues in finite element analyses of localization of deformation. *Engineering Computations*.

[25] Dean, D. W., Allport, L. C., and Chevalier, M. J. (2015). The R5 procedures for assessing the high temperature response of structures: Current status and recent developments. In *Transactions of SMiRT-23*, Paper 458, Manchester, UK.

[26] Dean, D. W., Budden, P. J., and Ainsworth, R. A. (2007). R5 procedures for assessing the high temperature response of structures: current status and future developments. In *ASME Pressure Vessels and Piping Conference*, volume 42797, pages 403–412.

[27] Dean, D. W. and Gladwin, D. N. (2007). Creep crack growth behaviour of type 316H steels and proposed modifications to standard testing and analysis methods. *International Journal of Pressure Vessels and Piping*, 84(6):378–395.

[28] Dean, D. W. and Johns, J. G. (2015). Structural integrity issues in high temperature nuclear plant: experience from operation of the UK advanced gas cooled reactor fleet. In *Transactions of SMiRT-23*, Paper 459, Manchester, UK.

[29] Deleo, F., Riordan, T., Baylor, J., and Cohen, M. (2020a). Creep and creep-fatigue crack growth at structural discontinuities and welds. Technical report, ASME, STP-PT-089.

[30] Deleo, F., Riordan, T., Baylor, J., and Cohen, M. (2020b). Creep-fatigue flaw growth analysis to support elevated temperature flaw size acceptance criteria. Technical report, ASME STP-PT-089, TerraPower, LLC.

[31] E1457-15, A. (2015). *Standard Test Method for Measurement of Creep Crack Growth Times in Metals*. ASTM International.

[32] Elmukashfi, E. and Cocks, A. C. F. (2021). A theoretical and computational investigation of mixed mode creep crack growth along an interface. *International Journal of Fracture*, 229(2):125–159.

[33] Energy, B. (2003). R5: Assessment procedure for the high temperature response of structures. Technical report, British Energy.

[34] Forsberg, C. W., Peterson, P. F., and Pickard, P. S. (2003). Molten-salt-cooled advanced high-temperature reactor for production of hydrogen and electricity. *Nuclear Technology*, 144(3):289–302.

[35] Gosz, M., Dolbow, J., and Moran, B. (1998). Domain integral formulation for stress intensity factor computation along curved three-dimensional interface cracks. *International Journal of Solids and Structures*, 35(15):1763–1783.

[36] Griffith, A. A. (1921). VI. the phenomena of rupture and flow in solids. *Philosophical Transactions of the Royal Society of London. Series A, Containing Papers of a Mathematical or Physical Character*, 221(582-593):163–198.

[37] Grover, P. S. and Saxena, A. (1995). Creep crack growth in power plant materials. *Integrity of Engineering Components*, 20(1):53–85.

[38] Grueter, L. and Zeibig, H. (1980). Creep crack growth in austenitic steels—applicability of fracture mechanics parameters. *Materialwissenschaft und Werkstofftechnik*, 11(12):423–434.

[39] Grunloh, H. J., Ryder, R. H., Gattuso, A., Bloom, J. M., Lee, D. R., Schultz, C. C., Sutherland, D. D., Harris, D. O., and Dedhia, D. D. (1992). An integrated approach to life assessment of boiler pressure parts, Vol. 4: BLESS code user's manual and life assessment guidelines. *EPRI Research Project*, pages 2253–10.

[40] Guidez, J., Coz, P. L., Martin, L., Mariteau, P., and Dupraz, R. (2005). Lifetime extension of the Phenix plant. *Nuclear Technology*, 150(1):37–43.

[41] Gupta, M., Alderliesten, R. C., and Benedictus, R. (2015). A review of T-stress and its effects in fracture mechanics. *Engineering Fracture Mechanics*, 134:218–241.

[42] Hadley, I. (2011). Fracture assessment methods for welded structures. *Fracture and Fatigue of Welded Joints and Structures*, pages 60–90.

[43] Hadley, I. (2018). BS 7910:2013 in brief. *International Journal of Pressure Vessels and Piping*, 165:263–269.

[44] Hall, D. E., McDowell, D. L., and Saxena, A. (1998). Crack tip parameters for creep-brittle crack growth. *Fatigue & Fracture of Engineering Materials & Structures*, 21(4):387–401.

[45] Holdsworth, S. R. (1998). Material data requirements for assessing defect integrity at high temperatures. In *High Temperature Power Plant and Process Plant Applications Session as held at the Materials Congress'98*, pages 177–197.

[46] Hutchinson, J. W. (1968). Singular behaviour at the end of a tensile crack in a hardening material. *Journal of the Mechanics and Physics of Solids*, 16(1):13–31.

[47] Hutchinson, J. W. (1983). Constitutive behavior and crack tip fields for materials undergoing creep-constrained grain boundary cavitation. *Acta Metallurgica*, 31(7):1079–1088.

[48] Hyde, C. J., Hyde, T. H., Sun, W., and Becker, A. A. (2010a). Damage mechanics based predictions of creep crack growth in 316 stainless steel. *Engineering Fracture Mechanics*, 77(12):2385–2402.

[49] Hyde, T. H. (1988). Creep crack growth in 316 stainless steel at 600°C. *High Temperature Technology*, 6(2):51–61.

[50] Hyde, T. H., Saber, M., and Sun, W. (2010b). Creep crack growth data and prediction for a P91 weld at 650 °C. *International Journal of Pressure Vessels and Piping*, 87(12):721–729.

[51] Irwin, G. R. (1957). Analysis of stresses and strains near the end of a crack traversing a plate. *Journal of Applied Mechanics*, 24(3):361–364.

[52] Jazaeri, H., Bouchard, P. J., Hutchings, M. T., Mamun, A. A., and Heenan, R. K. (2016). Study of cavities in a creep crack growth test specimen. *Procedia Structural Integrity*, 2:942–949.

[53] Jiang, W., Spencer, B. W., and Dolbow, J. E. (2020). Ceramic nuclear fuel fracture modeling with the extended finite element method. *Engineering Fracture Mechanics*, 223:106713.

[54] Kachanov, L. (1986). *Introduction to continuum damage mechanics*, volume 10. Springer Science & Business Media.

[55] Khalil, Z., Elghazouli, A. Y., and Martínez-Pañeda, E. (2022). A generalised phase field model for fatigue crack growth in elastic–plastic solids with an efficient monolithic solver. *Computer Methods in Applied Mechanics and Engineering*, 388:114286.

[56] Kim, N.-H., Oh, C.-S., Kim, Y.-J., Davies, C. M., Nikbin, K., and Dean, D. W. (2013a). Creep failure simulations of 316H at 550 °C: Part II–Effects of specimen geometry and loading mode. *Engineering Fracture Mechanics*, 105:169–181.

[57] Kim, N.-H., Oh, C.-S., Kim, Y.-J., Davies, C. M., Nikbin, K., and Dean, D. W. (2013b). Creep failure simulations of 316H at 550 °C: Part II – Effects of specimen geometry and loading mode. *Engineering Fracture Mechanics*, 105:169–181.

[58] Kim, N.-H., Oh, C.-S., Kim, Y.-J., Yoon, K.-B., and Ma, Y.-H. (2011). Comparison of fracture strain based ductile failure simulation with experimental results. *International Journal of Pressure Vessels and Piping*, 88(10):434–447.

[59] Kimura, M., Takaishi, T., Alfat, S., Nakano, T., and Tanaka, Y. (2021). Irreversible phase field models for crack growth in industrial applications: thermal stress, viscoelasticity, hydrogen embrittlement. *SN Appl. Sci.*, 3(781):695–704.

[60] Kumar, M. and Singh, I. V. (2020). Numerical investigation of creep crack growth in plastically graded materials using C(t) and XFEM. *Engineering Fracture Mechanics*, 226:106820.

[61] Larrosa, N. O., Ainsworth, R. A., Akid, R., Budden, P. J., Davies, C. M., Hadley, I., Tice, D. R., Turnbull, A., and Zhou, S. (2017). 'Mind the gap'in fitness-for-service assessment procedures-review and summary of a recent workshop. *International Journal of Pressure Vessels and Piping*, 158:1–19.

[62] Lindsay, A. D. et al. (2022). 2.0 - MOOSE: Enabling massively parallel multiphysics simulation. *SoftwareX*, 20:101202.

[63] Mehmanparast, A. (2012). *The influence of inelastic damage on creep, fatigue and fracture toughness*. PhD thesis, Imperial College London.

[64] Mehmanparast, A., Davies, C. M., Dean, D. W., and Nikbin, K. (2013a). Material pre-conditioning effects on the creep behaviour of 316H stainless steel. *International Journal of Pressure Vessels and Piping*, 108:88–93.

[65] Mehmanparast, A., Davies, C. M., Dean, D. W., and Nikbin, K. M. (2013b). The influence of pre-compression on the creep deformation and failure behaviour of Type 316H stainless steel. *Engineering Fracture Mechanics*, 110:52–67.

[66] Mehmanparast, A., Davies, C. M., Dean, D. W., and Nikbin, K. M. (2014a). Plastic pre-compression and creep damage effects on the fracture toughness behaviour of Type 316H stainless steel. *Engineering Fracture Mechanics*, 131:26–37.

[67] Mehmanparast, A., Davies, C. M., Webster, G. A., and Nikbin, K. M. (2014b). Creep crack growth rate predictions in 316H steel using stress dependent creep ductility. *Materials at High Temperatures*, 31(1):84–94.

[68] Messner, M. C., Phan, V.-T., and Sham, T.-L. (2018). A unified inelastic constitutive model for the average engineering response of grade 91 steel. In *Pressure Vessels and Piping Conference*, volume Volume 1B: Codes and Standards. V01BT01A015.

[69] Miyazaki, K., Iwamatsu, F., Nakanishi, S., and Shiratori, M. (2006). Stress intensity factor solution for subsurface flaw estimated by influence function method. In *ASME Pressure Vessels and Piping Conference*, volume 47527, pages 19–36.

[70] Murakami, S., Kawai, M., and Rong, H. (1988). Finite element analysis of creep crack growth by a local approach. *International Journal of Mechanical Sciences*, 30(7):491–502.

[71] Nibkin, K. M. and Radon, J. C. (1997). Meso-fracture of creep crack initiation and growth of engineering materials. *Theoretical and Applied Fracture Mechanics*, 26(1):41–45.

[72] Nikbin, K. M., Smith, D. J., and Webster, G. A. (1984a). Prediction of creep crack growth from uniaxial creep data. *Proceedings of the Royal Society of London. A. Mathematical and Physical Sciences*, 396(1810):183–197.

[73] Nikbin, K. M., Smith, D. J., and Webster, G. A. (1984b). Prediction of creep crack growth from uniaxial creep data. *Proceedings of the Royal Society of London. A. Mathematical and Physical Sciences*, 396(1810):183–197.

[74] Nikbin, K. M., Webster, G. A., and Turner, C. E. (1976). Relevance of nonlinear fracture mechanics to creep cracking. In *Cracks and Fracture*. ASTM International.

[75] Oh, C.-S., Kim, N.-H., Kim, Y.-J., Davies, C., Nikbin, K., and Dean, D. (2011). Creep failure simulations of 316H at 550 °C: Part I–A method and validation. *Engineering Fracture Mechanics*, 78(17):2966–2977.

[76] Onck, P. and van der Giessen, E. (1998). Growth of an initially sharp crack by grain boundary cavitation. *Journal of the Mechanics and Physics of Solids*, 47(1):99–139.

[77] O'Dowd, N. (2011). 1 - Constraint-based fracture mechanics in predicting the failure of welded joints. In Macdonald, K. A., editor, *Fracture and Fatigue of Welded Joints and Structures*, Woodhead Publishing Series in Welding and Other Joining Technologies, pages 17–30. Woodhead Publishing.

[78] Pandey, V. B., Singh, I. V., and Mishra, B. K. (2023). A new creep-fatigue interaction damage model and CDM-XFEM framework for creep-fatigue crack growth simulations. *Theoretical and Applied Fracture Mechanics*, 124:103740.

[79] Permann, C. J., Gaston, D. R., Andrš, D., Carlsen, R. W., Kong, F., Lindsay, A. D., Miller, J. M., Peterson, J. W., Slaughter, A. E., Stogner, R. H., and Martineau, R. C. (2020). MOOSE: Enabling massively parallel multiphysics simulation. *SoftwareX*, 11:100430.

[80] Petkov, M., Young, G. A., and Juan, P.-A. (2022a). Non-conservatism of ASME BPVC Section III Division 5 isochronous stress–strain curves for 316H stainless steel at low stresses. *Journal of Pressure Vessel Technology*, 144(6). 061506.

[81] Petkov, M. P., Chevalier, M., Dean, D., and Cocks, A. C. F. (2021). Creep-fatigue interactions in type 316H under typical high-temperature power plant operating conditions. *International Journal of Pressure Vessels and Piping*, 194:104500.

[82] Petkov, M. P., Elmukashfi, E., and Cocks, A. C. F. (2022b). Multi-scale modelling of creep cavity nucleation and growth in polycrystalline Type 316 stainless steel. *Philosophical Magazine*, 102(23):2362–2411.

[83] Pijaudier-Cabot, G. and Bažant, Z. P. (1987). Nonlocal damage theory. *Journal of Engineering Mechanics*, 113(10):1512–1533.

[84] Quintero, H. and Mehmanparast, A. (2016). Prediction of creep crack initiation behaviour in 316h stainless steel using stress dependent creep ductility. *International Journal of Solids and Structures*, 97-98:101–115.

[85] Radhakrishnan, V. M. and Kamaraj, M. (1990). Creep crack growth in type 316 stainless steel and its weldment. *High Temperature Technology*, 8 (1):219–26.

[86] Rashid, M. M. (1993). Incremental kinematics for finite element applications. *International Journal for Numerical Methods in Engineering*, 36(23):3937–3956.

[87] Rice, J. R. and Rosengren, G. F. (1968). Plane strain deformation near a crack tip in a power-law hardening material. *Journal of the Mechanics and Physics of Solids*, 16(1):1–12.

[88] Richardson, C. L., Hegemann, J., Sifakis, E., Hellrung, J., and Teran, J. M. (2011). An XFEM method for modeling geometrically elaborate crack propagation in brittle materials. *International Journal for Numerical Methods in Engineering*, 88(10):1042–1065.

[89] Riedel, H. (1981). Creep deformation at crack tips in elastic-viscoplastic solids. *Journal of the Mechanics and Physics of Solids*, 29(1):35–49.

[90] Riedel, H. and Rice, J. R. (1980). Tensile cracks in creeping solids. *ASTM STP*, 700:112–130.

[91] Saxena, A. (1988). Creep crack growth under transient conditions. *Materials Science and Engineering: A*, 103(1):125–129. Workshop on the Mechanics and Physics of Crack Growth: Application to Life Prediction.

[92] Scarlat, R. O., Laufer, M. R., Blandford, E. D., Zweibaum, N., Krumwiede, D. L., Cisneros, A. T., Andreades, C., Forsberg, C. W., Greenspan, E., Hu, L.-W., and Peterson, P. F. (2014). Design and licensing strategies for the fluoride-salt-cooled, high-temperature reactor (FHR) technology. *Progress in Nuclear Energy*, 77:406–420.

[93] Scarth, D. A., Kim, Y. J., and Vanderglas, M. L. (1985). A critical review on the application of elastic-plastic fracture mechanics to nuclear pressure vessel and piping systems. *Ontario Hydro Research Division*, Report No 85-257-K.

[94] Shih, C. F., Moran, B., and Nakamura, T. (1986). Energy release rate along a three-dimensional crack front in a thermally stressed body. *International Journal of fracture*, 30(2):79–102.

[95] Singh, G., Messner, M., Munday, L. B., and Spencer, B. W. (2022). High temperature creep test suite for Grizzly. Technical Report INL/RPT-22-67519, Idaho National Laboratory, Idaho Falls, ID.

[96] Skelton, R. P. and Gandy, D. (2008). Creep–fatigue damage accumulation and interaction diagram based on metallographic interpretation of mechanisms. *Materials at High Temperatures*, 25(1):27–54.

[97] Smith, E. and Beardsmore, D. W. (2009). Pessimisms inherent in current treatments of multiple defects in fracture assessments. In *Pressure Vessels and Piping Conference*, volume Volume 6: Materials and Fabrication, Parts A and B, pages 639–648.

[98] Spencer, B. W., Hoffman, W. M., Biswas, S., Jiang, W., Giorla, A., and Backman, M. A. (2021). Grizzly and BlackBear: Structural component aging simulation codes. *Nuclear Technology*, 207(7):981–1003.

[99] Spencer, B. W., Ke, J.-H., Nezdyur, M., Schwen, D., Neupane, H., and Jain, A. (2022). Summary of development for structural component modeling in Fiscal Year 2022. Technical Report INL/RPT-22-69943, Idaho National Laboratory.

[100] Spindler, M. W. (2004). The multiaxial creep ductility of austenitic stainless steels. *Fatigue & Fracture of Engineering Materials & Structures*, 27 (4):273–81.

[101] Spindler, M. W. and Cotton, C. C. (1998). Creep-fatigue crack growth in type 316H stainless steel through a zone of tensile residual stress. *Materials at High Temperatures*, 15(2):117–121.

[102] Tallman, A. E., Kumar, M. A., Castillo, A., Wen, W., Capolungo, L., and Tomé, C. N. (2020). Data-driven constitutive model for the inelastic response of metals: Application to 316H steel. *Integrating Materials and Manufacturing Innovation*, 9(4):339–357.

[103] Tallman, T. N. and Smyl, D. J. (2020). Structural health and condition monitoring via electrical impedance tomography in self-sensing materials: a review. *Smart Materials and Structures*, 29(12):123001.

[104] Tang, S., Guo, T. F., and Cheng, L. (2008). C*-controlled creep crack growth by grain boundary cavitation. *Acta Materialia*, 56(18):5293–5303.

[105] Tourret, D., Liu, H., and LLorca, J. (2022). Phase-field modeling of microstructure evolution: Recent applications, perspectives and challenges. *Progress in Materials Science*, 123:100810. A Festschrift in Honor of Brian Cantor.

[106] Townsend, R. D. (2000). Review of service problems during high temperature operation. *Institute of Materials, Materials for High Power Generation and Process Plant Applications(UK),*, pages 199–223.

[107] Wang, Y. Q., Spindler, M. W., Truman, C. E., and Smith, D. J. (2016). Critical analysis of the prediction of stress relaxation from forward creep of Type 316H austenitic stainless steel. *Materials & Design*, 95:656–668.

[108] Webster, G. A. and Ainsworth, R. A. (2013). *High temperature component life assessment*. Springer Science & Business Media.

[109] Webster, G. A., Davies, C. M., and Nikbin, K. M. (2010). Assessment of creep crack growth due to stress relief. *International Journal of Solids and Structures*, 47(7-8):881–886.

[110] Wen, J.-F., Tu, S.-T., Gao, X.-L., and Reddy, J. N. (2013). Simulations of creep crack growth in 316 stainless steel using a novel creep-damage model. *Engineering Fracture Mechanics*, 98:169–184.

[111] Wen, J.-F., Tu, S.-T., Xuan, F.-Z., Zhang, X.-W., and Gao, X.-L. (2016). Effects of stress level and stress state on creep ductility: Evaluation of different models. *Journal of Materials Science & Technology*, 32(8):695–704.

[112] Yatomi, M., Nikbin, K., and O'Dowd, N. (2003). Creep crack growth prediction using a damage based approach. *International Journal of Pressure Vessels and Piping*, 80(7):573–583. Creep crack growth in components.

[113] Yatomi, M. and Nikbin, K. M. (2014). Numerical prediction of creep crack growth in different geometries using simplified multiaxial void growth model. *Materials at High Temperatures*, 31(2):141–147.

[114] Zahoor, A. (1985). Closed form expressions for fracture mechanics analysis of cracked pipes. *Journal of Pressure Vessel Technology*, 107(2):203–205.